HIGH-ORDER INTEGRAL EQUATIONS FOR ELECTROMAGNETIC PROBLEMS IN LAYERED MEDIA WITH APPLICATIONS IN BIOLOGY AND SOLAR CELLS

by

Brian Zinser

A dissertation submitted to the faculty of
The University of North Carolina at Charlotte
in partial fulfillment of the requirements
for the degree of Doctor of Philosophy in
Applied Mathematics

Charlotte

2016

Approved by:

_____

Dr. Wei Cai

_____

Dr. Duan Chen

_____

Dr. Shaozhong Deng

_____

Dr. Greg Gbur

ABSTRACT

BRIAN ZINSER. High-order integral equations for electromagnetic problems in layered media with applications in biology and solar cells. (Under the direction of DR. WEI CAI)

We present two distinct mathematical models where high-order integral equations are applied to electromagnetic problems. The first problem is to find the electric potential in and around ion channels and Janus particles. The second problem is to find the electromagnetic scattering caused by a set of simple geometric objects.

In biology, we consider two types of inhomogeneities: the first one is a simple model of an ion channel which consists of a finite height cylindrical cavity embedded in a layered electrolytes/membrane environment, and the second one is a Janus particle made of two different semi-spherical dielectric materials. A boundary element method (BEM) for the Poisson-Boltzmann equation based on Müller's hyper-singular second kind integral equation formulation is used to accurately compute electrostatic potentials. The proposed BEM gives $O(1)$ condition numbers and we show that the second order basis converges faster and is more accurate than the first order basis.

For solar cells, we develop a Nyström volume integral equation (VIE) method for calculating the electromagnetic scattering according to the Maxwell equations. The Cauchy principal values (CPVs) that arise from the VIE are computed using a finite size exclusion volume with explicit correction integrals. Outside the exclusion, the hyper-singular integrals are computed using an interpolated quadrature formulae with tensor-product quadrature nodes. We considered cubes, rectangles, cylinders, spheres, and ellipsoids. As the new quadrature weights are pre-calculated and tab-

ulated, the integrals are calculated efficiently at runtime. Simulations with many scatterers demonstrate the efficiency of the interpolated quadrature formulae. We also demonstrate that the resulting VIE has high accuracy and p-convergence.

ACKNOWLEDGMENTS

The journey through graduate school is a long one in which the most important virtue is perseverance. Perseverance means making mathematics a constant part of one's life and continually striving to reach a better state of knowledge. Aristotle correctly points out that the journey toward the end goal of knowledge is best done alongside others who also desire to improve themselves by knowing the world. Here, a partial list is given of those who have a part of my journey towards that which is good.

First, I would like to acknowledge not only Dr. Cai's role as my advisor, but also his virtues that have improved me through my time working with him. As any good advisor should be, he is honest. However, he moderates his honesty with kindness and he is never angry. He is willing to accept that others do not always proceed in the same way as he would. In short, he is a mathematician whose intelligence is only surpassed by his magnanimity.

The rest of my committee is also deserving of high praise. Dr. Chen embodies patience perfectly. Over the past two years, I spent more time in his office than I did in my own, working through one detail or another that he needed me to finish before he could continue in his work. Next, Dr. Deng exemplifies charity as he is always willing to set aside his many tasks to help me figure out an concept in a paper or navigate the various rules of the graduate school. Finally, Dr. Gbur displays an inordinate amount of humility. He never uses his superior knowledge of physics to demonstrate how much more he knows than me and he respects my accomplishments

in mathematics. In short, I feel quite blessed to have a committee who excel not just in academic subjects, but in being virtuous people that I wish to emulate.

In addition to my committee, there are many other people who have helped shape my work. There are the wonderful teachers I learned from, the staff that made everything possible, and my fellow students who traveled the same path as me. It is impossible to describe how thankful I am to each person who has helped me. However, a few must be singled out. First is the diligent Mr. Hamrick, who tirelessly keeps the computers and servers running in the math department. Second, I am grateful that Huimin Lin left me her code for the Poisson Boltzmann equation and other materials. Third, I would like to thank those who held a position above my own, but still took the time to help me along my way: Min Hyung Cho, Changhao Yan, and Xingjie Li. Finally, I would like to name a few peers who helped me on my journey through graduate school: Katherine Baker, Kelly Smalenberger, Caylah Retz, Jun Yang, Jian Wu, Yijing Zhou, and Puja Rattan.

Last, I would like to acknowledge my family and friends. I count the time I have spent with any one of them more valuable than all my possessions. Specifically, I would like to single out my wife and daughter, both of whom have made the past few years the best of my life.

TABLE OF CONTENTS

LIST OF FIGURES xi

LIST OF TABLES xv

CHAPTER 1: INTRODUCTION 1

1.1. Motivation 1

1.2. Modeling Electrostatics 2

1.3. Modeling Electromagnetic Wave Scattering 4

1.4. Layout of the Dissertation 5

CHAPTER 2: ION CHANNEL AND JANUS PARTICLE 7

2.1. Governing Differential Equation for Electrostatics 7

2.2. Layered Green's Function 9

2.3. Boundary Integral Equations 16

2.3.1. Boundary Integral Equations of the First Kind 17

2.3.2. Boundary Integral Equations of the Second Kind 20

2.4. Matrix Equation 21

2.5. Quadrature Rules 24

2.6. Singular Integrands 27

2.7. Numerical Results 29

2.7.1. Dielectric Sphere 30

2.7.2. Janus Particle 34

2.7.3. Ion Channel 35

2.8. Future Work Concerning the PB Equation 42

2.9. Summary for Modeling with the PB Equation 45

CHAPTER 3: SINGULAR INTEGRALS IN THREE DIMENSIONS 46

3.1. Calculation of Integrals with Singular Kernels 46

3.2. Quadrature Formula over Tensor-Product Nodes 47

3.3. M-Point Tensor-Product Quadratures for a Cube or Rectangular Prism 49

3.3.1. Quadrature Rule when the Singularity $\mathbf{r}'$ is at the Center of the Cube 50

3.3.2. Quadrature Rule when the Singularity $\mathbf{r}'$ is not at the Center of the Cube 52

3.3.3. M-Point Tensor-Product Quadratures for a Cube 54

3.4. M-Point Tensor-Product Quadratures for a Cylinder 55

3.4.1. Quadrature Rule for a Subcylinder Centered at the Singularity $\mathbf{r}'$ 55

3.4.2. Quadrature Rule for all Subcylinders not Containing the Singularity $\mathbf{r}'$ 57

3.4.3. M-Point Tensor-Product Quadratures for a Cylinder 59

3.5. M-Point Tensor-Product Quadratures for a Sphere 61

3.5.1. Quadrature Rule over a Sphere for a Singular Kernel 61

3.5.2. M-Point Tensor-Product Quadratures for a Sphere 64

3.6. Algorithm Outline 68

3.7. Numerical Results 70

3.7.1. Numerical Results for when Ω is a Cube 72

3.7.2. Numerical Results for when Ω is a Rectangular Prism 73

3.7.3. Numerical Results for when Ω is a Cylinder 74

3.7.4. Numerical Results for when Ω is a Sphere 75

3.7.5. Numerical Results for when Ω is an Ellipsoid 75

3.8. Future Work for Integrating Singularities via Interpolation 76

3.9. Summary for Integrating Singular Integrands in Three Dimensions 80

CHAPTER 4: SOLAR CELLS 81

4.1. The Vector Wave Equation and its Corresponding Integral Equation 81

4.1.1. Maxwell Equations 81

4.1.2. Integral Equation Derivation 84

4.2. Derivation of the Integral Equation Based on the Helmholtz Decomposition 88

4.2.1. The Helmholtz Decomposition and the Helmholtz Equation 88

4.2.2. Integral Equation Derivation 90

4.3. Nyström Collocation Method for VIEs 93

4.4. Numerical Results 95

4.4.1. The Correction Terms 96

4.4.2. p-Convergence 97

4.4.3. Many Scatterers 100

4.5. Future Work Concerning Scatterers 102

4.6. Summary for Modeling Scattering with the Maxwell Equations 105

CHAPTER 5: CONCLUSION 106

5.1. Models of Physical Phenomena 106

5.2. Singular Integrands 107

PUBLICATIONS 110

REFERENCES 111

APPENDIX A: ANALYTICAL FORM FOR THE GREEN'S FUNCTION 115

APPENDIX B: INTEGRAL EQUATIONS FOR THE PB EQUATION 117

APPENDIX C: CURVILINEAR ELEMENTAL MAPPING 119

APPENDIX D: ROTATION MATRICES 121

LIST OF FIGURES

FIGURE 1: Schematic illustration of a three-layer medium. 7

FIGURE 2: Schematic illustration of an ion channel model. 9

FIGURE 3: Schematic illustration of a round-top cylinder. 18

FIGURE 4: The planar projection of the body-fitted mesh. Left: top semi-sphere surface; right: the side surface of the cylinder. 21

FIGURE 5: From the left to the right, the plots show the quadrature points when the singularity is at $(0, 0)$, $(0, 1)$, and $(1, 0)$, respectively. 26

FIGURE 6: From the left to the right, the plots show the quadrature points when the singularity is at $(0, 1/2)$, $(1/2, 1/2)$, and $(1/2, 0)$, respectively. 26

FIGURE 7: Quadrature points for a regular integral over the reference triangle with symmetric sample points (left) and sample points mapped from a cube (right). 27

FIGURE 8: Potential (left) and its derivative (right) on the dielectric sphere's boundary when $z = 0$ and the charge is inside the sphere at $(0.5, 0.1, 0.2)$. 30

FIGURE 9: Convergence of the potential and its normal derivatives on the dielectric sphere's boundary with the charge inside the sphere at $(0.5, 0.1, 0.2)$ as the mesh size n increases. The points mark our results and the lines are linear fits. 31

FIGURE 10: Potential (left) and its derivative (right) on the dielectric sphere's boundary when $z = 0$ and the charge is outside the sphere at $(0.5, 2, 0.2)$. 32

FIGURE 11: Convergence of potential and its normal derivative on the dielectric sphere's boundary with the charge outside the sphere at $(0.5, 2, 0.2)$ as the mesh size n increases. The points mark our results and the lines are linear fits. 33

FIGURE 12: Potential in and around Janus particles when $x = 0$ (left) and when $x = 1.2$ (right) for various values of ε. 36

FIGURE 13: Convergence of the potential in a Janus particle when ε is perturbed by 10^{-1} in the upper hemisphere as the mesh size n increases. The points mark our results and the lines are linear fits. 37

FIGURE 14: Schematic illustration of model setup for an ion channel with a cylindrical boundary (left) and with a deformed boundary (right). 38

FIGURE 15: Self-energy (left) and potential (right) in the ion channel with cylindrical sides, calculated using BIE of the 2^{nd} kind, 2^{nd} degree basis, and mesh parameter 16. 39

FIGURE 16: Convergence of the self-energy (left) and potential (right) inside the ion channel with cylindrical sides using BIE of the 2^{nd} kind as the mesh size n increases. The points mark our results and the lines are linear fits. 39

FIGURE 17: Self-energy (left) and potential (right) in the ion channel with deformed sides, calculated using BIE of the 2^{nd} kind, 2^{nd} degree basis, and mesh parameter 16. 41

FIGURE 18: Convergence of the self-energy (left) and potential (right) inside the ion channel with deformed sides using BIE of the 2^{nd} kind as the mesh size n increases. The points mark our results and the lines are linear fits. 41

FIGURE 19: ϕ_{out} contains a singularity and is difficult to solve for. w_{out} is smooth. The source charge is at $(0, 0, 1.01)$. 43

FIGURE 20: Points on a triangle for regular integration with the sample points mapped from a square by collapsing the top edge (left) and the new mapping that avoids clustering (right). 44

FIGURE 21: Quadrature points on the pyramid with base satisfying $x = 1$ (left) and on the cube $[-1, 1]^3$ (right). 51

FIGURE 22: From left to right, the illustrations correspond to subdivisions when the singularity is in a corner, near an edge, and at the center of a face. The subcube with a singularity is red. 53

FIGURE 23: Interpolation points, colored to show rotationally symmetric points, on the cube when $m = 3$ and $M = 27$. 55

FIGURE 24: Quadrature points for the subcylinders. Left: The subcylinder with $\mathbf{r}'$ at its center when $n = 8$; right: all subcylinders when $\mathbf{r}' = (0.2, 0.3, 0.4)$ when $n = n_{cyl} = n_w = 4$. 57

FIGURE 25: Interpolation points on the cylinder with circles when φ is a free variable and $m = 3$ and $M = 54$. 60

FIGURE 26: Sample points on the unit sphere. Left: Quadrature points when $\mathbf{r}' = (0.2, -0.3, -0.6)$ and $n = 8$; right: Interpolation points with circles when φ is a free variable, $m = 3$, and $M = 42$. 65

FIGURE 27: A plot of $\hat{L}_{i,k}(\rho, \theta)$ when $m_\theta = 3$. The Kronecker delta property is satisfied at $\theta = 0, \pi/3, 2\pi/3, \pi$. Note that the function does not depend on the ϕ axes, which goes into the page. 67

FIGURE 28: The $\log_{10}$ relative error of the integrals of $\cos(R)/R^k$ (left) and $\sin(R)/R^k$ (right) when Ω is the cube $\Omega = [-1, 1]^3$. $M = m^3$ sample points are used in (90). 72

FIGURE 29: The $\log_{10}$ relative error of the integral of the entries of $\hat{\mathbf{H}}(\mathbf{r}, \mathbf{r}')$ when Ω is the cube $\Omega = [-1/4, 1/4]^3$. Each point corresponds to an entry of $\hat{\mathbf{H}}$ for a given m; the line is a linear fit for all points. $M = m^3$ sample points are used in (90). 72

FIGURE 30: The $\log_{10}$ relative error of the integrals of $\cos(R)/R^k$ (left) and $\sin(R)/R^k$ (right). In the x, y, and z directions, basis functions were of degree $m - 1$, m, and m, respectively. Ω is a rectangular prism. 73

FIGURE 31: The $\log_{10}$ relative error of the integral of the entries of $\hat{\mathbf{H}}(\mathbf{r}, \mathbf{r}')$. In the x, y, and z directions, basis functions were of degree $m - 1$, m, and m, respectively. Ω is a rectangular prism. 73

FIGURE 32: The $\log_{10}$ relative error of the integrals of $\cos(R)/R^k$ (left) and $\sin(R)/R^k$ (right) when Ω is a cylinder. $M = 2m^3$ sample points are used in (90). 74

FIGURE 33: The $\log_{10}$ relative error of the integral of the entries of $\hat{\mathbf{H}}(\mathbf{r}, \mathbf{r}')$ when Ω is a cylinder. Each point corresponds to an entry of $\hat{\mathbf{H}}$ for a given m; the line is a linear fit for all points. $M = 2m^3$ sample points are used in (90). 74

FIGURE 34: The $\log_{10}$ relative error of the integrals of $\cos(R)/R^k$ (left) and $\sin(R)/R^k$ (right) when Ω is a sphere. $M = m_\rho(2m_\varphi(m_\theta - 1) + 2)$ sample points are used in (90). 75

FIGURE 35: The $\log_{10}$ relative error of the integral of the entries of $\hat{\mathbf{H}}(\mathbf{r}, \mathbf{r}')$ when Ω is a sphere. Each point corresponds to an entry of $\hat{\mathbf{H}}$ for a given m; the line is a linear fit for all points. $M = m_\rho(2m_\varphi(m_\theta - 1) + 2)$ sample points are used in (90). 75

FIGURE 36: The $\log_{10}$ relative error of the integrals of $\cos(R)/R^k$ (left) and $\sin(R)/R^k$ (right) when Ω is an ellipsoid. $M = m_\rho(2m_\varphi(m_\theta - 1) + 2)$ sample points are used in (90). 76

FIGURE 37: The $\log_{10}$ relative error of the integral of the entries of $\hat{\mathbf{H}}(\mathbf{r}, \mathbf{r}')$ when Ω is an ellipsoid. Each point corresponds to an entry of $\hat{\mathbf{H}}$ for a given m; the line is a linear fit for all points. $M = m_\rho(2m_\varphi(m_\theta - 1) + 2)$ sample points are used in (90). 76

FIGURE 38: Regular quadrature points (left) and interpolation points (right) on the tetrahedron. While not shown here, the distribution of points in the singular region is similar to Fig. 21. 78

FIGURE 39: A scatterer Ω in a layered medium, whose boundaries make up Σ. 83

FIGURE 40: Difference of matrix entries when $\delta = 0.1$ vs $\delta = 0.001$ when correction terms are omitted (a) and when they are included (b). 96

FIGURE 41: Convergence under the L^2 function norm for a cube with sides of length 2. Linear fit is given by $-0.57m + 1.1$. 98

FIGURE 42: Convergence under the L^2 function norm for a cylinder of radius 1 and height 2. Linear fit is given by $-0.48m + 0.07$. 99

FIGURE 43: Convergence under the L^2 function norm for a sphere of radius 1. Linear fit is given by $-0.89m + 0.59$. 100

FIGURE 44: E_x, E_y, E_z for an arrangement of cubes (left) and an arrangement of spheres (right). 101

LIST OF TABLES

TABLE 1: Quadrature points for a regular integral over the reference triangle. 27

TABLE 2: Quadrature rule used for a given example and mesh size. 30

TABLE 3: Relative error and convergence rate r of the potential and its normal derivative on the dielectric sphere's boundary; the charge is inside the sphere at $(0.5, 0.1, 0.2)$. 31

TABLE 4: Relative error and convergence rate r of the potential and its normal derivative on the dielectric sphere's boundary; the charge is outside the sphere at $(0.5, 2, 0.2)$. 33

TABLE 5: Relative error and convergence rate r of the potential on the two planes $x = 0$ and $x = 1.2$ for the Janus particle. The reference solution is obtained from when the mesh parameter is 64. 35

TABLE 6: Condition number κ and number of iterations N to solve the matrix equation corresponding to the Janus particle with a perturbation of 10^{-1}. 37

TABLE 7: Relative error and convergence rate r of the potential and self-energy for the ion channel with a cylindrical boundary using BIEs of the 2^{nd} kind. The reference solution is obtained from when the mesh parameter is 16. 40

TABLE 8: Condition number κ and number of iterations N to solve matrix equation corresponding to the ion channel with a cylindrical boundary. 40

TABLE 9: Relative error and convergence rate r of the potential and self-energy for the ion channel with a deformed boundary using BIEs of the 2^{nd} kind. The reference solution is obtained from when the mesh parameter is 16. 42

TABLE 10: Convergence of the nonzero matrix entries when the singularity is at center when correction terms are omitted. 96

TABLE 11: Timing results for matrix construction for a single spherical domain. 100

TABLE 12: Approximate absolute errors due to interpolation. Since the singularity is in the span of the IXFEM basis, its convergence rate is dominated by error due to interpolating $\cos(\sqrt{x^2 + y^2})$. 104

CHAPTER 1: INTRODUCTION

1.1 Motivation

Deriving and implementing models of electromagnetic problems is a multi-faceted problem. Speaking very generally, physics presents an equation that models a situation, mathematics provides the frameworks to derive a set of equations that can be solved to describe the situation, and computer science provides the tools required to solve the set of equations with the necessary level of granularity and accuracy. While this dissertation focuses on the role mathematics plays in describing the situation of interest, its purpose is broader insofar as is necessary to design accurate, useful models of the electrostatics in and around ion channels and Janus particles, and of the electromagnetic wave scattering of solar cells.

Moreover, partial differential equations model many physical phenomena, but obtaining a highly-accurate solution to them can often be difficult. Our approach involves finding the Green's function that is the fundamental solution to the partial differential equation in question. This approach results in a system of integral equations that can be solved for the unknown quantity in the partial differential equation. The Green's function's singular nature requires that it be given special attention when formulating high-order integral equations and the corresponding numerical method. My dissertation presents several ways to handle the Green's function's singular kernel

in the context of applications in biology and solar cells.

1.2 Modeling Electrostatics

Electrostatic interactions are recognized as important and dominant forces in various applications, including protein folding, stability of biomolecules, other biological processes, colloidal material sciences, and engineering devices such as nanoelectronics and near field optics [6]. In many of these applications, we are faced with a difficult task of finding the electrostatic fields in the presence of inhomogeneous media and/or layered structures. For instance, for ion transport through a biological membrane, the dynamics of the ions are closely related to the electrostatic forces of the permanent charges in the residues of ion proteins and the surrounding layered dielectric environment. In the application of drug designs, a drug molecule's binding with a virus protein depends greatly on the complicated geometry and the electrostatic potential distribution of the former. On the other hand, for the study of colloidal media involving Janus particles [40], the inhomogeneous polarization of the particles can be the key to creating novel electric, magnetic, and self-assembling phenomena for various engineering applications.

Finding the electrostatic potential in non-homogeneous media requires the solutions of the Poisson and/or Poisson-Boltzmann equation if ionic materials are involved [16]. There are two basic approaches in obtaining the solutions, either by analytic methods, such as image charge methods [7] [43] or generalized Born approximations [35], or by grid-based numerical methods [6]. While the former is easy to implement and computationally less intensive, it does not produce a high-accuracy solution when

modeling an ion channel [23]. The latter consists of finite difference, finite element methods, and by BEMs based on boundary integral equations. The BEMs reduce the solution domain to lower dimensional manifolds, provided a Green's function is available as in the cases of homogeneous or layered background materials wherein some isolated inhomogeneities such as a Janus particle or an ion channel may be embedded.

In this dissertation, we will present a hypersingular integral equation which gives a well-conditioned second kind integral equation formulation. The Green's function corresponding to the PB equation contains a weak singularity of $O(|\mathbf{r}-\mathbf{r}'|)$. The hypersingularity in the integral equations results from taking the second normal derivative of the Green's function is used, which is $O(|\mathbf{r}-\mathbf{r}'|^3)$. We employ a singularity subtraction technique due to Müller [28] and Rokhlin [33], and the hypersingularities in the integral operators from adjacent dielectric materials are canceled out and the final integral equations only contain a weakly singular integrand, ready to be treated by a simple local polar coordinate transform. This technique is especially significant because it allows for the hypersingularity to be reduced analytically before the system of integral equations is translated into computer code. At most, the computer code that implements the resulting numerical scheme deals with weakly-singular functions. Other subtraction techniques often require the difference to be calculated by the computer code, which can cause significant rounded error.

1.3 Modeling Electromagnetic Wave Scattering

Electromagnetic wave scattering depends largely on complex microstructures, which in turn affects the efficiency of various devices like solar cells. The interface between a dielectric and a conductor gives rise to electromagnetic excitations known as surface plasmon polaritons, which can be modeled by the wave form of Maxwell's equations [27]. Surface plasmons intensify the transmission of electromagnetic energy[3]. Moreover, the transmission factor is a function of the microstructure meaning that a small amount of roughness on the order of a few angstroms affects how well a solar cell absorbs light energy [31]. Further applications exist in modeling meta-materials, super-resolution imaging devices, and Raman scattering [30][19][32]. For the required amount of detail to be achieved, a mathematical model must produce accurate results in a very efficient manner.

We will model the time harmonic Maxwell equations via a Nyström volume integral equation (VIE) method for a set of scatterers. The volume of interest for the VIEs will coincide with the scatterers while the remaining region will be treated implicitly as a dielectrically homogeneous or layered background. The integral equation is a second kind Fredholm integral equation that satisfies the Silver-Müller radiation conditions at infinity [6].

For the model of the solar cells, the electric field must be obtained from Maxwell's equations. The Green's function for the vector form of Maxwell's equations contains a hyper-singularity of $O(|\mathbf{r} - \mathbf{r}'|^3)$. A two-fold approach is proposed to handle the singularity accurately and efficiently. First, a sphere of some small radius is excluded

from the singularity and a special integration technique is proposed for efficiently calculating the integral outside of the excluded sphere. The integration technique relies on integrating a set of basis functions against the singular kernel; the results can be used as weights in a new quadrature rule corresponding to the sample points of the basis functions. When the integral equation is solved, the new quadrature rule is used and the accuracy obtained when integrating the basis functions against the singular kernel is preserved even though the computation time is greatly reduced. Second, when a high-accuracy result is desired, some correction terms are added to account for integrals over the sphere. However, if the sphere's radius is sufficiently small and the integration of the basis functions against the singular kernel is accurate enough, the correction terms are not necessary and the integral of the hyper-singular function is calculated very quickly.

1.4 Layout of the Dissertation

This dissertation is laid out as follows: Chapter 2 introduces the Poisson-Boltzmann equation and presents models of ion channels and Janus particles based on it. Special attention given to the Green's function results in a boundary integral equation (BIE) in which all singular integrands have been made regular through the use of polar coordinates. Chapter 3 introduces a novel quadrature rule for calculating the Cauchy principle value of singular integrals in three dimensions. This quadrature rule is valid for any singular integral whose numerator is smooth enough to interpolate accurately. Chapter 4 introduces the vector wave equation for Maxwell's equations along with its integral representation. The quadrature rule from Chapter 3 is used to calculate

the Cauchy principle value of the integral and the scattering due to objects of simple geometries is calculated. Finally, some concluding remarks are given in Chapter 5.

CHAPTER 2: ION CHANNEL AND JANUS PARTICLE

2.1 Governing Differential Equation for Electrostatics

Following [47] closely, we consider a three layer medium of materials with different dielectric constants and inverse Debye-Hückle lengths, as shown in Fig. 1, and the middle layer has a thickness D. In layer Ω_j, $1 \leq j \leq 3$, we denote the dielectric constants by ε_j and the inverse Debye-Hückle lengths by λ_j.

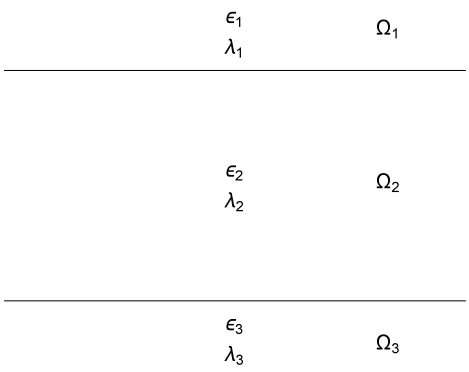

Figure 1: Schematic illustration of a three-layer medium.

For the study of ion channels, we consider a simple nano-pore hybrid model within a layered medium, which consists of a cylinder of height D within the middle layer (representing a cell membrane) with the axis of the cylinder perpendicular to the layer's boundary (see Fig. 2). Here, ε and λ can take different values inside the cylinder. The finite height cylinder represents a dividing interface in the hybrid solvation model for biomolecule simulations (refer to section 4.5 in [6] for more details). In such a hybrid model, inside the cylinder an atomistic representation of the physical system

is used, namely, channel proteins and ions can be described in terms of their atomic centers and charges and their interactions are governed by Coulombic potentials. On the other hand, the media outside the cylinder, composed of a membrane and solvents above and below, are modeled as layered continuum dielectrics described by dielectric constants and Debye-Hückle screen length and the electrostatics potential there is governed by the Poisson (for the membrane) and Poisson-Botlzmann (for the ionic solvents) equations.

Now let us assume that inside the cylinder there are N charges with magnitudes $q_k, 1 \leq k \leq N$, located at $\mathbf{r}_k$. Then, the electric potential field $\phi(\mathbf{r})$ satisfies the Poisson-Boltzmann (PB) equation

$$\nabla^2\phi(\mathbf{r}) - \lambda^2(\mathbf{r})\phi(\mathbf{r}) = -\frac{4\pi}{\varepsilon(\mathbf{r})}\sum_{k=1}^{N} q_k\delta(\mathbf{r}-\mathbf{r}_k), \tag{1}$$

with boundary conditions

$$[\phi(\mathbf{r})] = 0, \quad [\varepsilon(\mathbf{r})\frac{\partial\phi(\mathbf{r})}{\partial\mathbf{n}}] = 0, \tag{2}$$

where δ is the Dirac delta function, $[\cdot]$ denotes the jump across an interface, and $\mathbf{n}$ is the outward normal vector of the interface. The boundary conditions apply to any point on an interface between two media; the interface condition is not well defined when $\mathbf{r}$ is at a cross point of more than two interfaces. To avoid the latter case in the numerical solution process, after discretizing, we shift some nodes by a numerically negligible amount (i.e., close to machine zero) so no collocation point lies on multiple interfaces.

While (1) is the general governing equation, ε and λ can take different values in

different regions in Fig. 2. For instance, in the hybrid model, setting $\lambda_{2,\text{in}} = 0$ will produce the Poisson equation with the N charges inside the cylinder explicitly. Meanwhile, the remaining regions are treated implicitly with the homogeneous PB or Poisson equation. The cylindrical boundary only defines where the explicit regions ends and the implicit region begins. The hybrid model allows the shape of the physical shape of the ion channel to be modeled with atomistic details and accuracy.

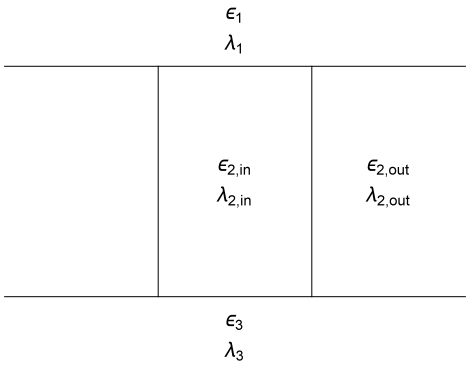

Figure 2: Schematic illustration of an ion channel model.

2.2 Layered Green's Function

As ε_j and λ_j may have different values inside the cylinder from the rest of the middle layer outside, we consider two distinct sets of layers when constructing the Green's functions for the corresponding partial differential equations: one for the inside and one for the outside. As depicted in Fig. 1 with three layers, each layer is homogeneous in x and y directions with constant $\varepsilon(\mathbf{r})$ and $\lambda(\mathbf{r})$. We proceed by deriving the Green's function $G(\mathbf{r}, \mathbf{r}')$ and its derivatives for the partial differential equation in (1). Namely, $G(\mathbf{r}, \mathbf{r}')$ will be the fundamental solution for (1) satisfying

the following partial differential equation

$$\varepsilon(\mathbf{r})[\nabla^2 G(\mathbf{r},\mathbf{r}') - \lambda^2(\mathbf{r})G(\mathbf{r},\mathbf{r}')] = -\delta(\mathbf{r}-\mathbf{r}'), \tag{3}$$

with boundary conditions

$$[G(\mathbf{r},\mathbf{r}')] = 0, \quad \left[\varepsilon(\mathbf{r})\frac{\partial G}{\partial \mathbf{n}}(\mathbf{r},\mathbf{r}')\right] = 0. \tag{4}$$

Following the approach in [23], we decompose the Green's function $G(\mathbf{r},\mathbf{r}')$ into a singular part and a smooth part

$$G(\mathbf{r},\mathbf{r}') = \begin{cases} G_{\mathrm{mod},j}(\mathbf{r},\mathbf{r}') + P_j(\mathbf{r},\mathbf{r}'), & \mathbf{r}\in\Omega_j, \\ G_{\mathrm{mod},j}(\mathbf{r},\mathbf{r}'), & \mathbf{r}\notin\Omega_j, \end{cases} \tag{5}$$

where

$$P_j(\mathbf{r},\mathbf{r}') = \frac{e^{-\lambda_j|\mathbf{r}-\mathbf{r}'|}}{4\pi\varepsilon_j|\mathbf{r}-\mathbf{r}'|}. \tag{6}$$

Then, $G_{\mathrm{mod},j}$ corresponds to the homogeneous differential equation

$$\nabla^2 G_{\mathrm{mod},j}(\mathbf{r},\mathbf{r}') - {\lambda_i}^2 G_{\mathrm{mod},j}(\mathbf{r},\mathbf{r}') = 0. \tag{7}$$

Let k_x and k_y be the spectral variables for x and y. Also let $\rho = \sqrt{x^2+y^2}$, $k_\rho = \sqrt{k_x^2+k_y^2}$, and $\tilde{\eta}_j = \sqrt{k_\rho^2+\lambda_j^2}$. Performing a Fourier transform on (7) in x and y, we have

$$\frac{\partial^2 \hat{G}_{\mathrm{mod},j}}{\partial z^2}(k_\rho,z,z') - {\tilde{\eta}_i}^2 \hat{G}_{\mathrm{mod},j}(k_\rho,z,z') = 0, \tag{8}$$

whose solution is

$$\hat{G}_{\mathrm{mod},j}(k_\rho,z,z') = C_{i,1}e^{-\tilde{\eta}_i z} + C_{i,2}e^{\tilde{\eta}_i z}, \tag{9}$$

where the values of $C_{i,1}$ and $C_{i,2}$ are given in the appendix.

To recover the function G, which is defined in the physical domain, we consider the inverse Fourier transform as a Sommerfeld integral. Specifically, we have

$$\begin{aligned} G_{\mathrm{mod},j}(\rho, z, z') &= F^{-1}\{\hat{G}_{\mathrm{mod},j}(k_\rho, z, z')\} \\ &= \frac{1}{2\pi}\int_{-\infty}^{\infty}\int_{-\infty}^{\infty} \hat{G}_{\mathrm{mod},j}(k_\rho, z, z') e^{i[k_y(y-y')+k_x(x-x')]} dk_x dk_y \\ &= \frac{1}{2\pi}\int_{0}^{\infty}\int_{0}^{2\pi} \hat{G}_{\mathrm{mod},j}(k_\rho, z, z') k_\rho e^{ik_\rho\rho\cos(\alpha-\beta)} d\beta dk_\rho \\ &= \int_{0}^{\infty} \hat{G}_{\mathrm{mod},j}(k_\rho, z, z') k_\rho J_0(k_\rho\rho) dk_\rho, \end{aligned} \tag{10}$$

where

$$J_0(z) = \frac{1}{2\pi}\int_0^{2\pi} e^{iz\sin\theta}\, d\theta \tag{11}$$

is the 0^{th} Bessel function of the first kind.

In terms of $\mathbf{r}$ and $\mathbf{r}'$, we have

$$G(\mathbf{r}, \mathbf{r}') = \begin{cases} G_{\mathrm{mod},j}(\mathbf{r}, \mathbf{r}') + P_j(\mathbf{r}, \mathbf{r}'), & \mathbf{r} \in \Omega_j, \\ G_{\mathrm{mod},j}(\mathbf{r}, \mathbf{r}'), & \mathbf{r} \notin \Omega_j. \end{cases} \tag{12}$$

We will need the first and second normal derivatives of G with respect to $\mathbf{r}$ and $\mathbf{r}'$, denoted by $\partial G/\partial \mathbf{n}$, $\partial G/\partial \mathbf{n}'$, and $\partial^2 G/\partial \mathbf{n}'\partial \mathbf{n}$. Specifically, the derivatives are defined in terms of G by

$$\frac{\partial G}{\partial \mathbf{n}} = n_1\frac{\partial}{\partial x}G + n_2\frac{\partial}{\partial y}G + n_3\frac{\partial}{\partial z}G, \tag{13}$$

$$\frac{\partial G}{\partial \mathbf{n}'} = n_1'\frac{\partial}{\partial x'}G + n_2'\frac{\partial}{\partial y'}G + n_3'\frac{\partial}{\partial z'}G, \tag{14}$$

and

$$\frac{\partial^2 G}{\partial \mathbf{n}'\partial \mathbf{n}} = n_1'\frac{\partial}{\partial x'}\frac{\partial G}{\partial \mathbf{n}} + n_2'\frac{\partial}{\partial y'}\frac{\partial G}{\partial \mathbf{n}} + n_3'\frac{\partial}{\partial z'}\frac{\partial G}{\partial \mathbf{n}}, \tag{15}$$

where $\mathbf{n} = (n_1, n_2, n_3)$ and $\mathbf{n}' = (n_1', n_2', n_3')$.

For derivatives with respect to z or z', the derivative can be moved inside the Sommerfeld integral and applied to $\hat{G}_{\mathrm{mod},j}$.

$$\frac{\partial}{\partial z} G(\rho, z, z') = \int_0^\infty \frac{\partial}{\partial z} \hat{G}_{\mathrm{mod},j}(k_\rho, z, z') k_\rho J_0(k_\rho \rho) dk_\rho \tag{16}$$

$$\frac{\partial}{\partial z'} G(\rho, z, z') = \int_0^\infty \frac{\partial}{\partial z'} \hat{G}_{\mathrm{mod},j}(k_\rho, z, z') k_\rho J_0(k_\rho \rho) dk_\rho \tag{17}$$

As specified in the appendix, we can take $\hat{G}_{\mathrm{mod},j}$ as $A_i e^{-\tilde{\eta}_i z}$, $B_i e^{-\tilde{\eta}_i z} + C_i e^{\tilde{\eta}_i z}$, or $D_i e^{\tilde{\eta}_i z}$ depending on the regions $\mathbf{r}$ and $\mathbf{r}'$ are in. Their first derivatives with respect to z are

$$\begin{aligned} \frac{\partial}{\partial z} A_i e^{-\tilde{\eta}_i z} &= -\tilde{\eta}_1 A_i e^{-\tilde{\eta}_i z}, \qquad & \frac{\partial}{\partial z} B_i e^{-\tilde{\eta}_i z} &= -\tilde{\eta}_2 B_i e^{-\tilde{\eta}_i z}, \\ \frac{\partial}{\partial z} C_i e^{\tilde{\eta}_i z} &= \tilde{\eta}_2 C_i e^{\tilde{\eta}_i z}, \qquad & \frac{\partial}{\partial z} D_i e^{\tilde{\eta}_i z} &= \tilde{\eta}_3 D_i e^{\tilde{\eta}_i z}. \end{aligned} \tag{18}$$

Their first derivatives with respect to z' when z' is in Ω_1 are

$$\begin{aligned} \frac{\partial}{\partial z'} A_1 e^{-\tilde{\eta}_i z} &= -\tilde{\eta}_1 A_1 e^{-\tilde{\eta}_i z}, \qquad & \frac{\partial}{\partial z'} B_1 e^{-\tilde{\eta}_i z} &= -\tilde{\eta}_1 B_1 e^{-\tilde{\eta}_i z}, \\ \frac{\partial}{\partial z'} C_1 e^{\tilde{\eta}_i z} &= -\tilde{\eta}_1 C_1 e^{\tilde{\eta}_i z}, \qquad & \frac{\partial}{\partial z'} D_1 e^{\tilde{\eta}_i z} &= -\tilde{\eta}_1 D_1 e^{\tilde{\eta}_i z}. \end{aligned} \tag{19}$$

Their first derivatives with respect to z' when z' is in Ω_2 are

$$\begin{aligned} \frac{\partial}{\partial z'} A_2 e^{-\tilde{\eta}_i z} &= \tilde{\eta}_2(-A_{2,1} + A_{2,2}) e^{-\tilde{\eta}_i z}, \qquad & \frac{\partial}{\partial z'} B_2 e^{-\tilde{\eta}_i z} &= \tilde{\eta}_2(-B_{2,1} + B_{2,2}) e^{-\tilde{\eta}_i z}, \\ \frac{\partial}{\partial z'} C_2 e^{\tilde{\eta}_i z} &= \tilde{\eta}_2(-C_{2,1} + C_{2,2}) e^{\tilde{\eta}_i z}, \qquad & \frac{\partial}{\partial z'} D_2 e^{\tilde{\eta}_i z} &= \tilde{\eta}_2(-D_{2,1} + D_{2,2}) e^{\tilde{\eta}_i z}, \end{aligned} \tag{20}$$

where the notation $A_2 = A_{2,1} + A_{2,2}$, $B_2 = B_{2,1} + B_{2,2}$, $C_2 = C_{2,1} + C_{2,2}$, and $D_2 = D_{2,1} + D_{2,2}$ was used. Finally, their first derivatives with respect to z' when z'

is in Ω_3 are

$$\begin{aligned}\frac{\partial}{\partial z'}A_3e^{-\tilde{\eta}_i z} = \tilde{\eta}_3 A_3 e^{-\tilde{\eta}_i z} \text{ and } \frac{\partial}{\partial z'}B_3e^{-\tilde{\eta}_i z} = \tilde{\eta}_3 B_3 e^{-\tilde{\eta}_i z} \\ \frac{\partial}{\partial z'}C_3e^{\tilde{\eta}_i z} = \tilde{\eta}_3 C_3 e^{\tilde{\eta}_i z} \text{ and } \frac{\partial}{\partial z'}D_3e^{\tilde{\eta}_i z} = \tilde{\eta}_3 D_3 e^{\tilde{\eta}_i z}\end{aligned} \tag{21}$$

For derivatives in the directions of x or y, some quantities must be defined first. Furthermore, we will use polar coordinates for derivatives with respect to x, y, x', or y'. Using polar coordinates defined by

$$\begin{aligned}x - x' &= \rho\cos(\alpha) \\ y - y' &= \rho\sin(\alpha),\end{aligned} \tag{22}$$

we can now define the following derivative operators as

$$\begin{aligned}\frac{\partial}{\partial x} &= \cos(\alpha)\frac{\partial}{\partial \rho} - \frac{\sin(\alpha)}{\rho}\frac{\partial}{\partial \alpha} \\ \frac{\partial}{\partial y} &= \sin(\alpha)\frac{\partial}{\partial \rho} + \frac{\cos(\alpha)}{\rho}\frac{\partial}{\partial \alpha} \\ \frac{\partial}{\partial x'} &= -\{\cos(\alpha)\frac{\partial}{\partial \rho} - \frac{\sin(\alpha)}{\rho}\frac{\partial}{\partial \alpha}\} \\ \frac{\partial}{\partial y'} &= -\{\sin(\alpha)\frac{\partial}{\partial \rho} + \frac{\cos(\alpha)}{\rho}\frac{\partial}{\partial \alpha}\}.\end{aligned} \tag{23}$$

Also of use are the Bessel functions J_0, J_1, and J_2 of the first kind. They are defined by

$$J_0(u) = \frac{1}{2\pi}\int_0^{2\pi} e^{iu\sin\theta}\, d\theta \tag{24}$$

$$J_1(u) = \frac{1}{2\pi}\int_0^{2\pi} e^{-i(\theta - u\sin(\theta))}\, d\theta \tag{25}$$

$$J_2(u) = \frac{1}{2\pi}\int_0^{2\pi} e^{i(2\theta - u\sin(\theta))}\, d\theta. \tag{26}$$

Moreover, the derivatives of the Bessel functions are related by

$$\begin{aligned} J_0'(u) &= -J_1(u) \\ J_1'(u) &= -J_2(u) + \frac{J_1(u)}{u}. \end{aligned} \tag{27}$$

Applying the derivative in polar coordinates, we have the following first derivatives

$$\begin{aligned} \frac{\partial}{\partial x} G_{\mathrm{mod},j}(\rho, z, z') &= \left(\cos(\alpha)\frac{\partial}{\partial \rho} - \frac{\sin(\alpha)}{\rho}\frac{\partial}{\partial \alpha}\right) \int_0^\infty \hat{G}_{\mathrm{mod},j}(k_\rho, z, z') k_\rho J_0(k_\rho \rho) dk_\rho \\ &= \cos(\alpha) \int_0^\infty \hat{G}_{\mathrm{mod},j}(k_\rho, z, z') k_\rho \frac{\partial}{\partial \rho} J_0(k_\rho \rho) dk_\rho \\ &= -\cos(\alpha) \int_0^\infty \hat{G}_{\mathrm{mod},j}(k_\rho, z, z') {k_\rho}^2 J_1(k_\rho \rho) dk_\rho \\ \frac{\partial}{\partial y} G_{\mathrm{mod},j}(\rho, z, z') &= -\sin(\alpha) \int_0^\infty \hat{G}_{\mathrm{mod},j}(k_\rho, z, z') {k_\rho}^2 J_1(k_\rho \rho) dk_\rho \\ \frac{\partial}{\partial x'} G_{\mathrm{mod},j}(\rho, z, z') &= \cos(\alpha) \int_0^\infty \hat{G}_{\mathrm{mod},j}(k_\rho, z, z') {k_\rho}^2 J_1(k_\rho \rho) dk_\rho \\ \frac{\partial}{\partial y'} G_{\mathrm{mod},j}(\rho, z, z') &= \sin(\alpha) \int_0^\infty \hat{G}_{\mathrm{mod},j}(k_\rho, z, z') {k_\rho}^2 J_1(k_\rho \rho) dk_\rho \end{aligned} \tag{28}$$

Using the same methods as used for the first derivatives, the second derivatives not involving z are

$$\begin{aligned} \frac{\partial^2}{\partial x' \partial x} G_{\mathrm{mod},j}(\rho, z, z') &= -\cos^2(\alpha) \int_0^\infty \hat{G}_{\mathrm{mod},j}(k_\rho, z, z') {k_\rho}^3 J_2(k_\rho \rho) dk_\rho \\ &\quad + \frac{1}{\rho} \int_0^\infty \hat{G}_{\mathrm{mod},j}(k_\rho, z, z') {k_\rho}^2 J_1(k_\rho \rho) dk_\rho \\ \frac{\partial^2}{\partial x' \partial y} G_{\mathrm{mod},j}(\rho, z, z') &= -\cos(\alpha)\sin(\alpha) \int_0^\infty \hat{G}_{\mathrm{mod},j}(k_\rho, z, z') {k_\rho}^3 J_2(k_\rho \rho) dk_\rho \\ \frac{\partial^2}{\partial y' \partial x} G_{\mathrm{mod},j}(\rho, z, z') &= -\cos(\alpha)\sin(\alpha) \int_0^\infty \hat{G}_{\mathrm{mod},j}(k_\rho, z, z') {k_\rho}^3 J_2(k_\rho \rho) dk_\rho \\ \frac{\partial^2}{\partial y' \partial y} G_{\mathrm{mod},j}(\rho, z, z') &= -\sin^2(\alpha) \int_0^\infty \hat{G}_{\mathrm{mod},j}(k_\rho, z, z') {k_\rho}^3 J_2(k_\rho \rho) dk_\rho \\ &\quad + \frac{1}{\rho} \int_0^\infty \hat{G}_{\mathrm{mod},j}(k_\rho, z, z') {k_\rho}^2 J_1(k_\rho \rho) dk_\rho, \end{aligned} \tag{29}$$

and the second derivatives involving z are

$$\begin{aligned}
\frac{\partial^2}{\partial x' \partial z} G_{\mathrm{mod},j}(\rho, z, z') &= \cos(\alpha) \int_0^\infty \frac{\partial}{\partial z} \hat{G}_{\mathrm{mod},j}(k_\rho, z, z') {k_\rho}^2 J_1(k_\rho \rho) dk_\rho \\
\frac{\partial^2}{\partial y' \partial z} G_{\mathrm{mod},j}(\rho, z, z') &= \sin(\alpha) \int_0^\infty \frac{\partial}{\partial z} \hat{G}_{\mathrm{mod},j}(k_\rho, z, z') {k_\rho}^2 J_1(k_\rho \rho) dk_\rho \\
\frac{\partial^2}{\partial z' \partial x} G_{\mathrm{mod},j}(\rho, z, z') &= -\cos(\alpha) \int_0^\infty \frac{\partial}{\partial z'} \hat{G}_{\mathrm{mod},j}(k_\rho, z, z') {k_\rho}^2 J_1(k_\rho \rho) dk_\rho \\
\frac{\partial^2}{\partial z' \partial y} G_{\mathrm{mod},j}(\rho, z, z') &= -\sin(\alpha) \int_0^\infty \frac{\partial}{\partial z'} \hat{G}_{\mathrm{mod},j}(k_\rho, z, z') {k_\rho}^2 J_1(k_\rho \rho) dk_\rho \\
\frac{\partial^2}{\partial z' \partial z} G_{\mathrm{mod},j}(\rho, z, z') &= \int_0^\infty \frac{\partial}{\partial z'} \frac{\partial}{\partial z} \hat{G}_{\mathrm{mod},j}(k_\rho, z, z') k_\rho J_0(k_\rho \rho) dk_\rho.
\end{aligned} \tag{30}$$

Next, recall that the fundamental solution for ε_j and λ_j was given by (6) as

$$P_j(\mathbf{r}, \mathbf{r}') = \frac{e^{-\lambda_j |\mathbf{r} - \mathbf{r}'|}}{4\pi \varepsilon_j |\mathbf{r} - \mathbf{r}'|}. \tag{31}$$

Then, its normal derivative with respect to $\mathbf{r}$ is given by

$$\begin{aligned}
\frac{\partial P_j}{\partial \mathbf{n}}(\mathbf{r}, \mathbf{r}') &= \frac{1}{4\pi\varepsilon_j} \frac{1}{|\mathbf{r} - \mathbf{r}'|} \frac{\partial}{\partial \mathbf{n}} [e^{-\lambda_j |\mathbf{r} - \mathbf{r}'|}] + \frac{1}{4\pi\varepsilon_j} e^{-\lambda_j |\mathbf{r} - \mathbf{r}'|} \frac{\partial}{\partial \mathbf{n}} [\frac{1}{|\mathbf{r} - \mathbf{r}'|}] \\
&= -\frac{\lambda_j}{4\pi\varepsilon_j} e^{-\lambda_j |\mathbf{r} - \mathbf{r}'|} \frac{1}{|\mathbf{r} - \mathbf{r}'|} \frac{\partial |\mathbf{r} - \mathbf{r}'|}{\partial \mathbf{n}} - \frac{1}{4\pi\varepsilon_j} e^{-\lambda_j |\mathbf{r} - \mathbf{r}'|} \frac{1}{|\mathbf{r} - \mathbf{r}'|^2} \frac{\partial |\mathbf{r} - \mathbf{r}'|}{\partial \mathbf{n}} \\
&= -(\lambda_j |\mathbf{r} - \mathbf{r}'| + 1) \frac{e^{-\lambda_j |\mathbf{r} - \mathbf{r}'|}}{4\pi\varepsilon_j |\mathbf{r} - \mathbf{r}'|^2} \frac{\partial |\mathbf{r} - \mathbf{r}'|}{\partial \mathbf{n}} \\
&= -(\lambda_j |\mathbf{r} - \mathbf{r}'| + 1) \frac{e^{-\lambda_j |\mathbf{r} - \mathbf{r}'|}}{4\pi\varepsilon_j |\mathbf{r} - \mathbf{r}'|^3} (\mathbf{r} - \mathbf{r}') \cdot \mathbf{n}
\end{aligned} \tag{32}$$

Repeating the same steps again but with respect to $\mathbf{r}'$, we have

$$\frac{\partial P_j}{\partial \mathbf{n}'}(\mathbf{r}, \mathbf{r}') = (\lambda_j |\mathbf{r} - \mathbf{r}'| + 1) \frac{e^{-\lambda_j |\mathbf{r} - \mathbf{r}'|}}{4\pi\varepsilon_j |\mathbf{r} - \mathbf{r}'|^3} (\mathbf{r} - \mathbf{r}') \cdot \mathbf{n}' \tag{33}$$

For $\partial^2 P_j/\partial\mathbf{n}\partial\mathbf{n}'$, we apply $\partial/\partial\mathbf{n}'$ to the second line of (32) to get

$$
\begin{aligned}
\frac{\partial^2 P_j}{\partial\mathbf{n}'\partial\mathbf{n}}(\mathbf{r},\mathbf{r}') = & \\
& -\frac{\lambda_j}{4\pi\varepsilon_j}\frac{\partial}{\partial\mathbf{n}'}[e^{-\lambda_j\cdot|\mathbf{r}-\mathbf{r}'|}]\frac{1}{|\mathbf{r}-\mathbf{r}'|}\frac{\partial|\mathbf{r}-\mathbf{r}'|}{\partial\mathbf{n}} - \frac{\lambda_j}{4\pi\varepsilon_j}e^{-\lambda_j|\mathbf{r}-\mathbf{r}'|}\frac{\partial}{\partial\mathbf{n}'}[\frac{1}{|\mathbf{r}-\mathbf{r}'|}]\frac{\partial|\mathbf{r}-\mathbf{r}'|}{\partial\mathbf{n}} \\
& -\frac{\lambda_j}{4\pi\varepsilon_j}e^{-\lambda_j|\mathbf{r}-\mathbf{r}'|}\frac{1}{|\mathbf{r}-\mathbf{r}'|}\frac{\partial^2|\mathbf{r}-\mathbf{r}'|}{\partial\mathbf{n}'\partial\mathbf{n}} - \frac{1}{4\pi\varepsilon_j}\frac{\partial}{\partial\mathbf{n}'}[e^{-\lambda_j|\mathbf{r}-\mathbf{r}'|}]\frac{1}{|\mathbf{r}-\mathbf{r}'|^2}\frac{\partial|\mathbf{r}-\mathbf{r}'|}{\partial\mathbf{n}} \\
& -\frac{1}{4\pi\varepsilon_j}e^{-\lambda_j|\mathbf{r}-\mathbf{r}'|}\frac{\partial}{\partial\mathbf{n}'}[\frac{1}{|\mathbf{r}-\mathbf{r}'|^2}]\frac{\partial|\mathbf{r}-\mathbf{r}'|}{\partial\mathbf{n}} - \frac{1}{4\pi\varepsilon_j}e^{-\lambda_j|\mathbf{r}-\mathbf{r}'|}\frac{1}{|\mathbf{r}-\mathbf{r}'|^2}\frac{\partial^2|\mathbf{r}-\mathbf{r}'|}{\partial\mathbf{n}'\partial\mathbf{n}} \\
= & -\frac{\lambda_j}{4\pi\varepsilon_j}(-\lambda_j e^{-\lambda_j|\mathbf{r}-\mathbf{r}'|}\frac{\partial|\mathbf{r}-\mathbf{r}'|}{\partial\mathbf{n}'})\frac{1}{|\mathbf{r}-\mathbf{r}'|}\frac{\partial|\mathbf{r}-\mathbf{r}'|}{\partial\mathbf{n}} \\
& -\frac{\lambda_j}{4\pi\varepsilon_j}e^{-\lambda_j|\mathbf{r}-\mathbf{r}'|}(-\frac{1}{|\mathbf{r}-\mathbf{r}'|^2}\frac{\partial|\mathbf{r}-\mathbf{r}'|}{\partial\mathbf{n}'})\frac{\partial|\mathbf{r}-\mathbf{r}'|}{\partial\mathbf{n}} \\
& -\frac{\lambda_j}{4\pi\varepsilon_j}e^{-\lambda_j|\mathbf{r}-\mathbf{r}'|}\frac{1}{|\mathbf{r}-\mathbf{r}'|}\frac{\partial^2|\mathbf{r}-\mathbf{r}'|}{\partial\mathbf{n}'\partial\mathbf{n}} \\
& -\frac{1}{4\pi\varepsilon_j}(-\lambda_j e^{-\lambda_j|\mathbf{r}-\mathbf{r}'|}\frac{\partial|\mathbf{r}-\mathbf{r}'|}{\partial\mathbf{n}'})\frac{1}{|\mathbf{r}-\mathbf{r}'|^2}\frac{\partial|\mathbf{r}-\mathbf{r}'|}{\partial\mathbf{n}} \\
& -\frac{1}{4\pi\varepsilon_j}e^{-\lambda_j|\mathbf{r}-\mathbf{r}'|}(-2\frac{1}{|\mathbf{r}-\mathbf{r}'|^3}\frac{\partial|\mathbf{r}-\mathbf{r}'|}{\partial\mathbf{n}'})\frac{\partial|\mathbf{r}-\mathbf{r}'|}{\partial\mathbf{n}} \\
& -\frac{1}{4\pi\varepsilon_j}e^{-\lambda_j|\mathbf{r}-\mathbf{r}'|}\frac{1}{|\mathbf{r}-\mathbf{r}'|^2}\frac{\partial^2|\mathbf{r}-\mathbf{r}'|}{\partial\mathbf{n}'\partial\mathbf{n}} \\
= & \frac{e^{-\lambda_j|\mathbf{r}-\mathbf{r}'|}}{4\pi\varepsilon_j}(\lambda_j^2\frac{1}{|\mathbf{r}-\mathbf{r}'|} + 2\lambda_j\frac{1}{|\mathbf{r}-\mathbf{r}'|^2} + 2\frac{1}{|\mathbf{r}-\mathbf{r}'|^3})\frac{\partial|\mathbf{r}-\mathbf{r}'|}{\partial\mathbf{n}'}\frac{\partial|\mathbf{r}-\mathbf{r}'|}{\partial\mathbf{n}} \\
& -(\lambda_j\frac{1}{|\mathbf{r}-\mathbf{r}'|} + \frac{1}{|\mathbf{r}-\mathbf{r}'|^2})\frac{\partial^2|\mathbf{r}-\mathbf{r}'|}{\partial\mathbf{n}'\partial\mathbf{n}}
\end{aligned}
\tag{34}
$$

We now have G and all the necessary derivatives of G.

2.3 Boundary Integral Equations

In this section, we will derive the BIEs of the second kind and the corresponding discrete matrix equation. First, it is necessary to introduce a new mathematical domain with a smoother boundary upon which the BIEs will be formulated. In Fig. 2,

the boundary of the cylinder has sharp corners which will affect the accuracy of BEMs. While many techniques have been proposed to obtain an accurate solution such as graded meshes [8] [2] [21] and pre-calculated charge basis functions [5], we employ a more straightforward approach first proposed in [23]. Specifically, we add a semi-sphere to the top and bottom of the cylinder and consider the resulting pill-shaped domain, shown in Fig. 3, denoted by Ω with a boundary $S = \partial\Omega$, which is composed of the two semi-spheres and the side wall of the cylinder. These semi-spheres are purely *mathematical* and do not have any impact on the underlying physical problem under study, namely, the potential distribution around the finite height cylinder as depicted in Fig. 2. Moreover, note that when Green's identity is applied, the integrals along the horizontal interfaces will cancel, leaving only integrals over S. If we set the physical constants inside the semi-spheres equal to the corresponding ones outside, we obtain Fig. 2. In [23], integral equations of the first kind were derived on S, following the approach of [29]. However, these integral equations are ill-conditioned [6]. In this chapter, we will use BIEs of the second kind, instead.

2.3.1 Boundary Integral Equations of the First Kind

Summarizing the results in [23], the integral equation of the first kind are given as follows.

Let $\mathbf{r}'$ be outside Ω. Then we consider a three-layer domain where $\varepsilon(\mathbf{r})$ and $\lambda(\mathbf{r})$ are constant on each layer. Outside the boundary of the pill domain, we have no charges. As such, we begin with equation (1) with 0 on the right hand side and equation (3),

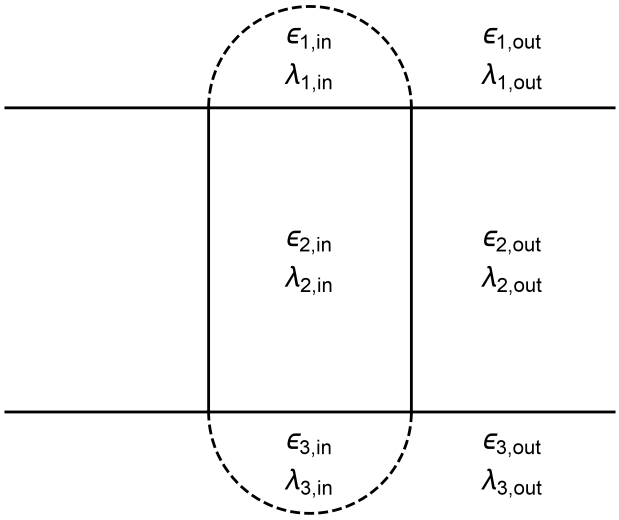

Figure 3: Schematic illustration of a round-top cylinder.

reproduced here for convenience.

$$\nabla^2\phi_{\text{out}}(\mathbf{r}) - \lambda^2_{\text{out}}(\mathbf{r})\phi_{out}(\mathbf{r}) = 0 \tag{35}$$

$$\varepsilon_{\text{out}}(\mathbf{r})[\nabla^2 G_{out}(\mathbf{r},\mathbf{r}') - \lambda^2_{out}(\mathbf{r})G_{out}(\mathbf{r},\mathbf{r}')] = -\delta(\mathbf{r}-\mathbf{r}') \tag{36}$$

We multiply (35) by $\varepsilon_{\text{out}}(\mathbf{r})G_{\text{out}}(\mathbf{r},\mathbf{r}')$ and multiply (36) by $\phi_{\text{out}}(\mathbf{r})$ and integrate their difference to get

$$\int_{\mathbb{R}^3\setminus(\Omega\cup B(\mathbf{r}',\rho))} \varepsilon_{\text{out}}(\mathbf{r})\left[G_{\text{out}}(\mathbf{r},\mathbf{r}')\nabla^2\phi_{out}(\mathbf{r}) - \phi_{\text{out}}(\mathbf{r})\nabla^2 G_{\text{out}}(\mathbf{r},\mathbf{r}')\right] d\mathbf{r} = 0 \tag{37}$$

where $B(\mathbf{r}',\rho)$ is a ball of radius ρ at $\mathbf{r}'$. Using Green's identity, we move the domain of integration to the boundary S. Details can be found in the appendix.

$$\phi_{\text{out}}(\mathbf{r}') = \int_S \varepsilon_{\text{out}}(\mathbf{r})\left[\phi_{\text{out}}(\mathbf{r})\frac{\partial G_{\text{out}}(\mathbf{r},\mathbf{r}')}{\partial\mathbf{n}} - G_{\text{out}}(\mathbf{r},\mathbf{r}')\frac{\partial\phi_{\text{out}}(\mathbf{r})}{\partial\mathbf{n}}\right] dS(\mathbf{r}) \tag{38}$$

Taking the limit as $\mathbf{r}'$ approaches $\mathbf{p}$ in S in equation (38) and using the boundary

conditions (2), we have

$$\frac{1}{2}\phi_{\text{ins}}(\mathbf{p}) = \int_S \varepsilon_{\text{out}}(\mathbf{r}) \left[\phi_{\text{ins}}(\mathbf{r})\frac{\partial G_{\text{out}}(\mathbf{r},\mathbf{p}')}{\partial \mathbf{n}} - G_{\text{out}}(\mathbf{r},\mathbf{p})\frac{\varepsilon_{\text{ins}(\mathbf{r})}}{\varepsilon_{\text{out}(\mathbf{r})}}\frac{\partial \phi_{\text{ins}}(\mathbf{r})}{\partial \mathbf{n}}\right] dS(\mathbf{r}). \quad (39)$$

Let $\mathbf{r}'$ be inside Ω. Then we consider a three-layer domain where $\varepsilon(\mathbf{r})$ and $\lambda(\mathbf{r})$ are constant on each layer. We begin with equations (1) and (3) for N charges.

$$\nabla^2\phi_{ins}(\mathbf{r}) - \lambda_{ins}^2(\mathbf{r})\phi_{ins}(\mathbf{r}) = -\frac{1}{\varepsilon(\mathbf{r})}\sum_{k=1}^{N} q_k\delta(\mathbf{r}-\mathbf{r}_k) \quad (40)$$

$$\varepsilon_{ins}(\mathbf{r})[\nabla^2 G_{ins}(\mathbf{r},\mathbf{r}') - \lambda_{ins}^2(\mathbf{r})G_{ins}(\mathbf{r},\mathbf{r}')] = -\delta(\mathbf{r}-\mathbf{r}') \quad (41)$$

Next, we multiply (40) by $\varepsilon_{\text{ins}}(\mathbf{r})G_{\text{ins}}(\mathbf{r},\mathbf{r}')$ and multiply (41) by $\phi_{\text{ins}}(\mathbf{r})$ and integrate their difference to get

$$\begin{aligned}\int_{\Omega\cup B(\mathbf{r}',\rho)} \varepsilon_{\text{ins}}(\mathbf{r}) \left[G_{\text{ins}}(\mathbf{r},\mathbf{r}')\nabla^2\phi_{ins}(\mathbf{r}) - \phi_{ins}(\mathbf{r})\nabla^2 G_{\text{ins}}(\mathbf{r},\mathbf{r}')\right] d\mathbf{r} \\ = -\sum_{i=1}^{N} q_i G_{\text{ins}}(\mathbf{r}_i,\mathbf{p})\end{aligned} \quad (42)$$

where $B(\mathbf{r}',\rho)$ is a ball of radius ρ at $\mathbf{r}'$. Applying Green's identity, we move the integral to the boundary S. Details can be found in the appendix.

$$\begin{aligned}\phi_{\text{ins}}(\mathbf{r}') = \int_S \varepsilon_{\text{ins}}(\mathbf{r}) \left[G_{\text{ins}}(\mathbf{r},\mathbf{r}')\frac{\partial\phi_{\text{ins}}(\mathbf{r})}{\partial\mathbf{n}} - \phi_{\text{ins}}(\mathbf{r})\frac{\partial G_{\text{ins}}(\mathbf{r},\mathbf{r}')}{\partial\mathbf{n}}\right] dS(\mathbf{r}) \\ + \sum_{i=1}^{N} q_i G_{\text{ins}}(\mathbf{r}_i,\mathbf{r}')\end{aligned} \quad (43)$$

Taking the limit as $\mathbf{r}'$ approaches a point $\mathbf{p}$ in S from the inside, we have

$$\begin{aligned}\frac{1}{2}\phi_{\text{ins}}(\mathbf{p}) = \int_S \varepsilon_{\text{ins}}(\mathbf{r}) \left[G_{\text{ins}}(\mathbf{r},\mathbf{p})\frac{\partial\phi_{\text{ins}}(\mathbf{r})}{\partial\mathbf{n}} - \phi_{\text{ins}}(\mathbf{r})\frac{\partial G_{\text{ins}}(\mathbf{r},\mathbf{p})}{\partial\mathbf{n}}\right] dS(\mathbf{r}) \\ + \sum_{i=1}^{N} q_i G_{\text{ins}}(\mathbf{r}_i,\mathbf{p})\end{aligned} \quad (44)$$

Together, equations (39) and (44) make up the integral equations of the first kind.

However, they form an ill-conditioned system of equations. Thus, we will consider integral equations of the second kind.

2.3.2 Boundary Integral Equations of the Second Kind

Taking the normal derivative of (38) with respect to $\mathbf{r}'$, we get the following equation for $\mathbf{r}'$ outside Ω.

$$\frac{\partial \phi_{\text{out}}(\mathbf{r}')}{\partial \mathbf{n}'} = \int_S \varepsilon_{\text{out}}(\mathbf{r}) \left[\phi_{\text{out}}(\mathbf{r}) \frac{\partial^2 G_{\text{out}}(\mathbf{r}, \mathbf{r}')}{\partial \mathbf{n}' \partial \mathbf{n}} - \frac{\partial G_{\text{out}}(\mathbf{r}, \mathbf{r}')}{\partial \mathbf{n}'} \frac{\partial \phi_{\text{out}}(\mathbf{r})}{\partial \mathbf{n}} \right] dS(\mathbf{r}). \tag{45}$$

On the other hand, taking the limit from the outside as $\mathbf{r}'$ approaches a point $\mathbf{p}$ on S in (45) and using the boundary conditions (2), we have

$$\frac{1}{2} \frac{\varepsilon_{\text{in}}(\mathbf{p})}{\varepsilon_{\text{out}}(\mathbf{p})} \frac{\partial \phi_{\text{in}}(\mathbf{p})}{\partial \mathbf{n}'} = \int_S \varepsilon_{\text{out}}(\mathbf{r}) \left[\phi_{\text{in}}(\mathbf{r}) \frac{\partial^2 G_{\text{out}}(\mathbf{r}, \mathbf{p})}{\partial \mathbf{n}' \partial \mathbf{n}} - \frac{\partial G_{\text{out}}(\mathbf{r}, \mathbf{p})}{\partial \mathbf{n}'} \frac{\varepsilon_{\text{in}}(\mathbf{r})}{\varepsilon_{\text{out}}(\mathbf{r})} \frac{\partial \phi_{\text{in}}(\mathbf{r})}{\partial \mathbf{n}} \right] dS(\mathbf{r}). \tag{46}$$

Next, taking the normal derivative of (43) with respect to $\mathbf{r}'$, we get the following equation for $\mathbf{r}'$ inside Ω,

$$\begin{aligned} \frac{\partial \phi_{\text{in}}(\mathbf{r}')}{\partial \mathbf{n}'} = & \int_S \varepsilon_{\text{in}}(\mathbf{r}) \left[\frac{\partial G_{\text{in}}(\mathbf{r}, \mathbf{r}')}{\partial \mathbf{n}'} \frac{\partial \phi_{\text{in}}(\mathbf{r})}{\partial \mathbf{n}} - \phi_{\text{in}}(\mathbf{r}) \frac{\partial^2 G_{\text{in}}(\mathbf{r}, \mathbf{r}')}{\partial \mathbf{n}' \partial \mathbf{n}} \right] dS(\mathbf{r}) \\ & + \sum_{i=1}^{N} q_i \frac{\partial G_{\text{in}}(\mathbf{r}_i, \mathbf{r}')}{\partial \mathbf{n}'}. \end{aligned} \tag{47}$$

Then, allowing $\mathbf{r}'$ approach a point $\mathbf{p}$ on S from the inside, we have

$$\begin{aligned} \frac{1}{2} \frac{\partial \phi_{\text{in}}(\mathbf{p})}{\partial \mathbf{n}'} = & \int_S \varepsilon_{\text{in}}(\mathbf{r}) \left[\frac{\partial G_{\text{in}}(\mathbf{r}, \mathbf{p})}{\partial \mathbf{n}'} \frac{\partial \phi_{\text{in}}(\mathbf{r})}{\partial \mathbf{n}} - \phi_{\text{in}}(\mathbf{r}) \frac{\partial^2 G_{\text{in}}(\mathbf{r}, \mathbf{p})}{\partial \mathbf{n}' \partial \mathbf{n}} \right] dS(\mathbf{r}) \\ & + \sum_{i=1}^{N} q_i \frac{\partial G_{\text{in}}(\mathbf{r}_i, \mathbf{p})}{\partial \mathbf{n}'}. \end{aligned} \tag{48}$$

The first integral equation of the second kind is obtained by summing (39) and

(44),

$$\begin{aligned}\phi_{\text{in}}(\mathbf{p}) = &\int_S \left[\varepsilon_{\text{in}}(\mathbf{r})G_{\text{in}}(\mathbf{r},\mathbf{p}) - \varepsilon_{\text{in}}(\mathbf{r})G_{\text{out}}(\mathbf{r},\mathbf{p})\right]\frac{\partial\phi_{\text{in}}(\mathbf{r})}{\partial\mathbf{n}}dS(\mathbf{r}) \\ &- \int_S \left[\varepsilon_{\text{in}}(\mathbf{r})\frac{\partial G_{\text{in}}(\mathbf{r},\mathbf{p})}{\partial\mathbf{n}} - \varepsilon_{\text{out}}(\mathbf{r})\frac{\partial G_{\text{out}}(\mathbf{r},\mathbf{p}')}{\partial\mathbf{n}}\right]\phi_{\text{in}}(\mathbf{r})dS(\mathbf{r}) \\ &+ \sum_{i=1}^{N} q_i G_{\text{in}}(\mathbf{r}_i,\mathbf{p}).\end{aligned} \tag{49}$$

Meanwhile, the second integral equation of the second kind is the sum of (46) and (48),

$$\begin{aligned}\left(\frac{1}{2}+\frac{1}{2}\frac{\varepsilon_{\text{in}}(\mathbf{p})}{\varepsilon_{\text{out}}(\mathbf{p})}\right)\frac{\partial\phi_{\text{in}}(\mathbf{p})}{\partial\mathbf{n}'} = &\int_S \left[\varepsilon_{\text{in}}(\mathbf{r})\frac{\partial G_{\text{in}}(\mathbf{r},\mathbf{p})}{\partial\mathbf{n}'} - \varepsilon_{\text{in}}(\mathbf{r})\frac{\partial G_{\text{out}}(\mathbf{r},\mathbf{p})}{\partial\mathbf{n}'}\right]\frac{\partial\phi_{\text{in}}(\mathbf{r})}{\partial\mathbf{n}}dS(\mathbf{r}) \\ &- \int_S \left[\varepsilon_{\text{in}}(\mathbf{r})\frac{\partial^2 G_{\text{in}}(\mathbf{r},\mathbf{p})}{\partial\mathbf{n}'\partial\mathbf{n}} - \varepsilon_{\text{out}}(\mathbf{r})\frac{\partial^2 G_{\text{out}}(\mathbf{r},\mathbf{p})}{\partial\mathbf{n}'\partial\mathbf{n}}\right]\phi_{\text{in}}(\mathbf{r})dS(\mathbf{r}) \\ &+ \sum_{i=1}^{N} q_i \frac{\partial G_{\text{in}}(\mathbf{r}_i,\mathbf{p})}{\partial\mathbf{n}'}.\end{aligned} \tag{50}$$

2.4 Matrix Equation

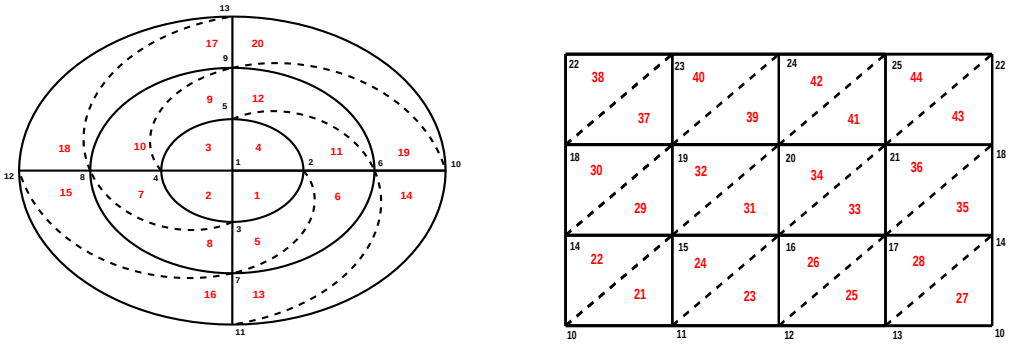

Figure 4: The planar projection of the body-fitted mesh. Left: top semi-sphere surface; right: the side surface of the cylinder.

To solve the BIEs (49) and (50), we discretize the boundary S using a finite element

type triangulation. Specifically, we introduce a mesh of curvilinear triangles that conform to S. Fig. 4 shows the projections of such a mesh and details concerning its construction can be found in [23]. Let $\mathbf{r}_t$ denote the coordinates of the t^{th} mesh point and $\psi_t(\mathbf{r})$ be the Lagrange basis functions with the Kronecker delta property, $\psi_{t_i}(\mathbf{r}_{t_j}) = \delta_{i,j}$. This means that for the first degree basis functions, all points $\mathbf{r}_t$ are vertices of triangles. For the second degree basis functions, the points $\mathbf{r}_t$ can be vertices or be on the edges of the triangles. Next, let

$$f(\mathbf{r}) = \phi_{\text{in}}(\mathbf{r}), \tag{51}$$

$$h(\mathbf{r}) = \frac{\partial \phi_{\text{in}}(\mathbf{r})}{\partial n}, \tag{52}$$

and we can interpolate f and h using the basis functions to get

$$f(\mathbf{r}) \approx \sum_t f_t \psi_t(\mathbf{r}) = \sum_t f(\mathbf{r}_t)\psi_t(\mathbf{r}), \tag{53}$$

$$h(\mathbf{r}) \approx \sum_t h_t \psi_t(\mathbf{r}) = \sum_t h(\mathbf{r}_t)\psi_t(\mathbf{r}). \tag{54}$$

Rewriting (49) and (50) in terms of the unknowns f_t and h_t, we have

$$\begin{aligned} f(\mathbf{p}) = & \sum_t h_t \int_S \left[\varepsilon_{\text{in}}(\mathbf{r}) G_{\text{in}}(\mathbf{r},\mathbf{p}) - \varepsilon_{\text{in}}(\mathbf{r}) G_{\text{out}}(\mathbf{r},\mathbf{p})\right] \psi_t(\mathbf{r}) dS(\mathbf{r}) \\ & - \sum_t f_t \int_S \left[\varepsilon_{\text{in}}(\mathbf{r}) \frac{\partial G_{\text{in}}(\mathbf{r},\mathbf{p})}{\partial \mathbf{n}} - \varepsilon_{\text{out}}(\mathbf{r}) \frac{\partial G_{\text{out}}(\mathbf{r},\mathbf{p})}{\partial \mathbf{n}}\right] \psi_t(\mathbf{r}) dS(\mathbf{r}) \\ & + \sum_{i=1}^{N} q_i G_{\text{in}}(\mathbf{r}_i,\mathbf{p}), \end{aligned} \tag{55}$$

$$\left(\frac{1}{2}+\frac{1}{2}\frac{\varepsilon_{\rm in}(\mathbf{p})}{\varepsilon_{\rm out}(\mathbf{p})}\right)h(\mathbf{p}) = \sum_t h_t \int_S \left[\varepsilon_{\rm in}(\mathbf{r})\frac{\partial G_{\rm in}(\mathbf{r},\mathbf{p})}{\partial \mathbf{n}'} - \varepsilon_{\rm in}(\mathbf{r})\frac{\partial G_{\rm out}(\mathbf{r},\mathbf{p})}{\partial \mathbf{n}'}\right]\psi_t(\mathbf{r})dS(\mathbf{r})$$
$$- \sum_t f_t \int_S \left[\varepsilon_{\rm in}(\mathbf{r})\frac{\partial^2 G_{\rm in}(\mathbf{r},\mathbf{p})}{\partial \mathbf{n}'\partial \mathbf{n}} - \varepsilon_{\rm out}(\mathbf{r})\frac{\partial^2 G_{\rm out}(\mathbf{r},\mathbf{p})}{\partial \mathbf{n}'\partial \mathbf{n}}\right]\psi_t(\mathbf{r})dS(\mathbf{r})$$
$$+ \sum_{i=1}^{N} q_i \frac{\partial G_{\rm in}(\mathbf{r}_i,\mathbf{p})}{\partial \mathbf{n}'}. \tag{56}$$

For the sake of simplicity, we define the following shorthand for the integral operators,

$$\begin{aligned}
{\rm S0} &= \int_S G_{\rm in}(\mathbf{r},\mathbf{p})\psi_t(\mathbf{r})dS(\mathbf{r}) & {\rm S1} &= \int_S G_{\rm out}(\mathbf{r},\mathbf{p})\psi_t(\mathbf{r})dS(\mathbf{r}) \\
{\rm D0} &= \int_S \frac{\partial G_{\rm in}(\mathbf{r},\mathbf{p})}{\partial \mathbf{n}}\psi_t(\mathbf{r})dS(\mathbf{r}) & {\rm D1} &= \int_S \frac{\partial G_{\rm out}(\mathbf{r},\mathbf{p})}{\partial \mathbf{n}}\psi_t(\mathbf{r})dS(\mathbf{r}) \\
{\rm D2} &= \int_S \frac{\partial G_{\rm in}(\mathbf{r},\mathbf{p})}{\partial \mathbf{n}'}\psi_t(\mathbf{r})dS(\mathbf{r}) & {\rm D3} &= \int_S \frac{\partial G_{\rm out}(\mathbf{r},\mathbf{p})}{\partial \mathbf{n}'}\psi_t(\mathbf{r})dS(\mathbf{r}) \\
{\rm T0} &= \int_S \frac{\partial^2 G_{\rm in}(\mathbf{r},\mathbf{p})}{\partial \mathbf{n}'\partial \mathbf{n}}\psi_t(\mathbf{r})dS(\mathbf{r}) & {\rm T1} &= \int_S \frac{\partial^2 G_{\rm out}(\mathbf{r},\mathbf{p})}{\partial \mathbf{n}'\partial \mathbf{n}}\psi_t(\mathbf{r})dS(\mathbf{r}) \\
b &= \sum_{i=1}^{N} q_i G_{\rm in}(\mathbf{r}_i,\mathbf{p}) & c &= \sum_{i=1}^{N} q_i \frac{\partial G_{\rm in}(\mathbf{r}_i,\mathbf{p})}{\partial \mathbf{n}'}.
\end{aligned} \tag{57}$$

Then we can rewrite (55) and (56) as

$$[I' + A]\begin{pmatrix} f \\ \\ h \end{pmatrix} = \begin{pmatrix} b \\ \\ c \end{pmatrix}, \tag{58}$$

where

$$I = \begin{pmatrix} I & 0 \\ \\ 0 & (\frac{1}{2}+\frac{1}{2}\frac{\varepsilon_{\rm in}}{\varepsilon_{\rm out}})I \end{pmatrix}, \tag{59}$$

$$A = \begin{pmatrix} (\varepsilon_{\rm in}{\rm D0} - \varepsilon_{\rm out}{\rm D1}) & -(\varepsilon_{\rm in}{\rm S0} - \varepsilon_{\rm in}{\rm S1}) \\ \\ (\varepsilon_{\rm in}{\rm T0} - \varepsilon_{\rm out}{\rm T1}) & -(\varepsilon_{\rm in}{\rm D2} - \varepsilon_{\rm in}{\rm D3}) \end{pmatrix}, \tag{60}$$

and $\mathbf{p}$ takes different mesh points $\mathbf{r}_t$ in different rows of the matrices. An elemental

mapping is employed so that all integrals are performed on a reference triangle with vertices at $(0,0)$, $(0,1)$, and $(1,0)$. The exact definition of the mapping is given in [23]. Since the integral equations are of the second kind, the coefficient matrix in (58) will be shown to have a low condition number, which ensures a small number of iterations by the GMRES solver for solving the matrix equation.

2.5 Quadrature Rules

When the singularity of the integrand $\mathbf{r}'$ is inside an element to be integrated, special treatment will be needed to handle the singularity. Otherwise, the integrals can be computed by means of quadrature points for a regular integral on the reference triangle. First, we will determine the order of the singularities of the Green's function's normal derivatives. Then we will describe the quadrature points to be used, accordingly.

As shown above, for $\mathbf{r}'$ on the element i to be integrated, there is a weak singularity on the order of $1/|\mathbf{r}-\mathbf{r}'|$. We employ the polar transformation described in [23] to compute the CPV of the integral when the singularity is at a vertex of the reference triangle. When the singularity is at the midpoint of an edge of the reference triangle, we modify the method by subdividing the triangle along the line that goes from the singularity to the opposite vertex. Specifically, let the polar transformation be defined by $\xi = \rho\cos(\alpha) + s_x$ and $\eta = \rho\sin(\alpha) + s_y$ where $\mathbf{s} = (s_x, s_y)$ is the singularity on the reference triangle. When $\mathbf{s} = (0,0)$, the triangle is defined by

$$T = \{(\rho,\alpha) : \rho \in [0, \frac{1}{\cos(\alpha)+\sin(\alpha)}] \text{ and } \alpha \in [0, \pi/2]\}. \tag{61}$$

When $\mathbf{s} = (0, 1)$, the triangle is defined by

$$T = \{(\rho, \alpha) : \rho \in [0, \frac{1}{\cos(\alpha - 3\pi/2)}] \text{ and } \alpha \in [3\pi/2, 7\pi/4]\}. \tag{62}$$

When $\mathbf{s} = (1, 0)$, the triangle is defined by

$$T = \{(\rho, \alpha) : \rho \in [0, \frac{1}{\cos(\pi - \alpha)}] \text{ and } \alpha \in [3\pi/4, \pi]\}. \tag{63}$$

When $\mathbf{s} = (0, 1/2)$, the two subtriangles are defined by

$$\begin{aligned} T_1 &= \{(\rho, \alpha) : \rho \in [0, \frac{1}{2\cos(\alpha - 3\pi/2)}] \text{ and } \alpha \in [-\frac{\pi}{2}, -\cos^{-1}(\frac{1}{\sqrt{1.25}})]\}, \\ T_2 &= \{(\rho, \alpha) : \rho \in [0, \frac{1}{2(\cos(\alpha) + \sin(\alpha))}] \text{ and } \alpha \in [-\cos^{-1}(\frac{1}{\sqrt{1.25}}), \frac{\pi}{2}]\}. \end{aligned} \tag{64}$$

When $\mathbf{s} = (1/2, 1/2)$, the two subtriangles are defined by

$$\begin{aligned} T_1 &= \{(\rho, \alpha) : \rho \in [0, \frac{1}{2\cos(\pi - \alpha)}] \text{ and } \alpha \in [\frac{3\pi}{4}, \frac{5\pi}{4}]\}, \\ T_2 &= \{(\rho, \alpha) : \rho \in [0, \frac{1}{2\cos(\alpha - 3\pi/2)}] \text{ and } \alpha \in [\frac{5\pi}{4}, \frac{7\pi}{4}]\}. \end{aligned} \tag{65}$$

When $\mathbf{s} = (1/2, 0)$, the two subtriangles are defined by

$$\begin{aligned} T_1 &= \{(\rho, \alpha) : \rho \in [0, \frac{1}{2(\cos(\alpha) + \sin(\alpha))}] \text{ and } \alpha \in [0, \cos^{-1}(\frac{-1}{2\sqrt{1.25}})]\}, \\ T_2 &= \{(\rho, \alpha) : \rho \in [0, \frac{1}{2\cos(\pi - \alpha)}] \text{ and } \alpha \in [\cos^{-1}(\frac{-1}{2\sqrt{1.25}}), \pi]\}. \end{aligned} \tag{66}$$

Fig. 5 shows the locations of 8 quadrature points in each triangle when subdivision is not required. Fig. 6 shows the locations of 8 quadrature points in each subtriangle when subdivision is required.

When $\mathbf{r}'$ is not on the element i to be integrated, there is no singularity in the integrand. Two different methods for finding quadrature points for this case can be used. When symmetric points are required, we use a method described by Dunavant

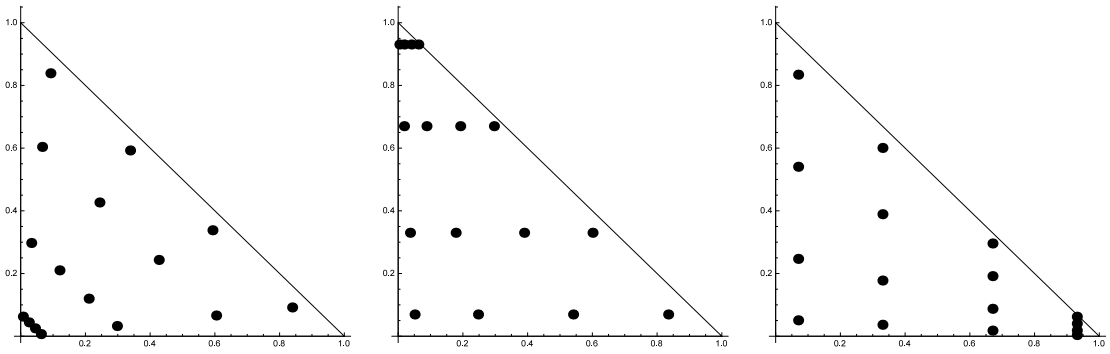

Figure 5: From the left to the right, the plots show the quadrature points when the singularity is at $(0,0)$, $(0,1)$, and $(1,0)$, respectively.

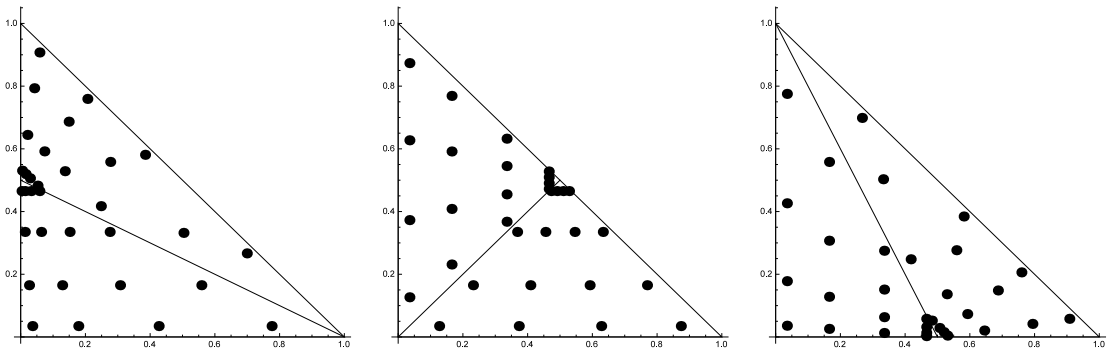

Figure 6: From the left to the right, the plots show the quadrature points when the singularity is at $(0,1/2)$, $(1/2,1/2)$, and $(1/2,0)$, respectively.

in [15] and implemented by Burkardt. Table 1 gives the coordinates for six symmetric points and Fig. 7 give the corresponding plot of the points. Alternatively, we begin with Gauss-Kronrod points and weights, provided by [1], defined on $[-1,1]$ and map them to the unit square $[0,1]\times[0,1]$. Then, we collapse the top edge of the square to the point $(0,1)$ according to the method in [13]. The mapping from the square to the triangle is given by

$$\xi(a,b)=\frac{(1+a)(1-b)}{4},\qquad \eta(a,b)=\frac{1+b}{2}, \tag{67}$$

with a Jacobian

$$J(a,b)=\frac{1-b}{8}. \tag{68}$$

Table 1: Quadrature points for a regular integral over the reference triangle.

i	ξ_i	η_i	w_i
1	0.10810301816807000	0.44594849091596500	0.22338158967801100
2	0.44594849091596500	0.44594849091596500	0.22338158967801100
3	0.44594849091596500	0.10810301816807000	0.22338158967801100
4	0.81684757298045896	0.09157621350977100	0.10995174365532200
5	0.09157621350977100	0.09157621350977100	0.10995174365532200
6	0.09157621350977100	0.81684757298045896	0.10995174365532200

While this approach involving the unit square lacks symmetry and efficiency, it provides an easy way to increase the number of quadrature points; see Fig. 7.

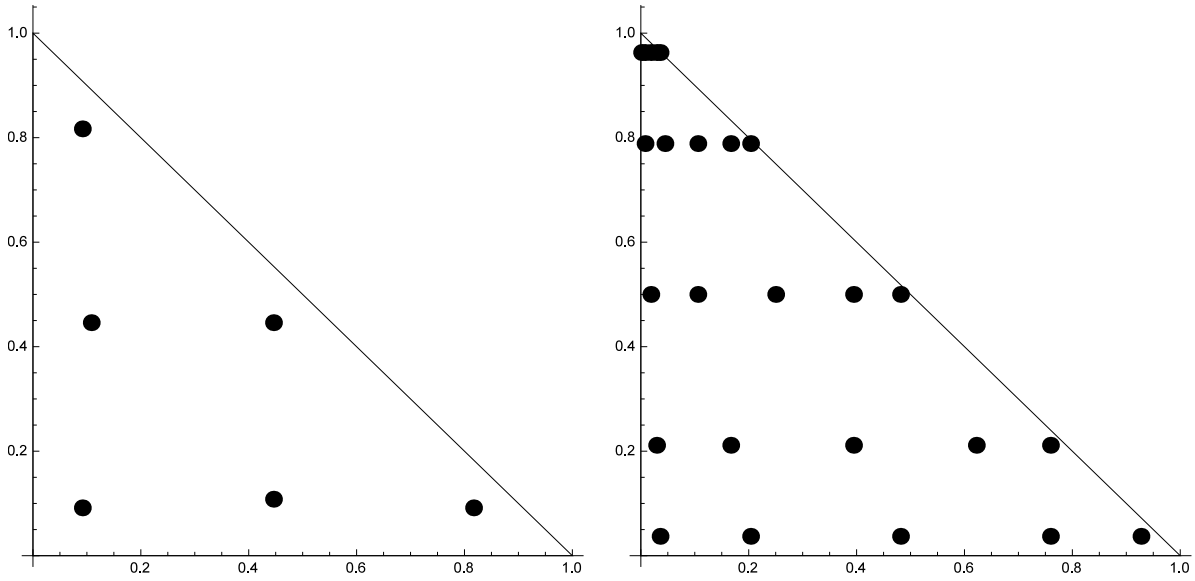

Figure 7: Quadrature points for a regular integral over the reference triangle with symmetric sample points (left) and sample points mapped from a cube (right).

2.6 Singular Integrands

We will show that all the singular integrals involved have weakly singular integrands on the order of $1/|\mathbf{r} - \mathbf{r}'|$. This is critical for the second kind integral equations (49) and (50) as it will allow the CPV integrals to be calculated by a simple polar transformation with a Jacobian on the order $O(|\mathbf{r} - \mathbf{r}'|)$. The singular part of G is contained in P_j, defined in (6); $G = O(1/|\mathbf{r} - \mathbf{r}'|)$. Similarly, the singular part

of $\partial G/\partial \mathbf{n}$ is contained in $\partial P_j/\partial \mathbf{n}$, given by (32). Since $\partial|\mathbf{r}-\mathbf{r}'|/\partial \mathbf{n} = O(|\mathbf{r}-\mathbf{r}'|)$, $\partial G/\partial \mathbf{n} = O(1/|\mathbf{r}-\mathbf{r}'|)$. Likewise, $\partial G/\partial \mathbf{n}' = O(1/|\mathbf{r}-\mathbf{r}'|)$. Similarly, the singular part of $\partial^2 G/\partial \mathbf{n}'\partial \mathbf{n}$ is contained in $\partial^2 P_j/\partial \mathbf{n}'\partial \mathbf{n}$, provided here for convenience.

$$\begin{aligned}\frac{\partial^2 P_j}{\partial \mathbf{n}'\partial \mathbf{n}}(\mathbf{r},\mathbf{r}') = &\frac{e^{-\lambda_j|\mathbf{r}-\mathbf{r}'|}}{4\pi\varepsilon_j}(\lambda_j^2\frac{1}{|\mathbf{r}-\mathbf{r}'|}+2\lambda_j\frac{1}{|\mathbf{r}-\mathbf{r}'|^2}+2\frac{1}{|\mathbf{r}-\mathbf{r}'|^3})\frac{\partial|\mathbf{r}-\mathbf{r}'|}{\partial \mathbf{n}'}\frac{\partial|\mathbf{r}-\mathbf{r}'|}{\partial \mathbf{n}}\\ &-\frac{e^{-\lambda_j|\mathbf{r}-\mathbf{r}'|}}{4\pi\varepsilon_j}(\lambda_j\frac{1}{|\mathbf{r}-\mathbf{r}'|}+\frac{1}{|\mathbf{r}-\mathbf{r}'|^2})\frac{\partial^2|\mathbf{r}-\mathbf{r}'|}{\partial \mathbf{n}'\partial \mathbf{n}}.\end{aligned} \tag{69}$$

The first term of has $\partial|\mathbf{r}-\mathbf{r}'|/\partial \mathbf{n}$ and $\partial|\mathbf{r}-\mathbf{r}'|/\partial \mathbf{n}'$, both of which are $O(|\mathbf{r}-\mathbf{r}'|)$. Thus, the first term is $O(1/|\mathbf{r}-\mathbf{r}'|)$ To determine the singularity of the second term, we note that

$$\begin{aligned}\frac{\partial^2|\mathbf{r}-\mathbf{r}'|}{\partial \mathbf{n}'\partial \mathbf{n}} =&\frac{\partial}{\partial \mathbf{n}'}[\frac{1}{|\mathbf{r}-\mathbf{r}'|}(\mathbf{r}-\mathbf{r}')\cdot\mathbf{n}]\\ =&-\frac{1}{|\mathbf{r}-\mathbf{r}'|^2}\frac{\partial|\mathbf{r}-\mathbf{r}'|}{\partial \mathbf{n}'}(\mathbf{r}-\mathbf{r}')\cdot\mathbf{n}+\frac{1}{|\mathbf{r}-\mathbf{r}'|}\frac{\partial}{\partial \mathbf{n}'}[\mathbf{r}'\cdot\mathbf{n}]\\ =&\frac{1}{|\mathbf{r}-\mathbf{r}'|}\frac{\partial|\mathbf{r}-\mathbf{r}'|}{\partial \mathbf{n}'}\frac{\partial|\mathbf{r}-\mathbf{r}'|}{\partial \mathbf{n}}+\frac{1}{|\mathbf{r}-\mathbf{r}'|}\mathbf{n}'\cdot\mathbf{n}.\end{aligned} \tag{70}$$

We can see that $\partial^2|\mathbf{r}-\mathbf{r}'|/\partial \mathbf{n}'\partial \mathbf{n} = O(1/|\mathbf{r}-\mathbf{r}'|)$. Thus, $\partial^2 G/\partial \mathbf{n}'\partial \mathbf{n}$ has a hypersingularity on the order of $1/|\mathbf{r}-\mathbf{r}'|^3$. However, in the integral equations of the second kind in (49) and (50), $\partial^2 G/\partial \mathbf{n}'\partial \mathbf{n}$ only appears in the difference $\varepsilon_{\text{in}}\partial^2 G_{\text{in}}/\partial \mathbf{n}'\partial \mathbf{n} - \varepsilon_{\text{out}}\partial^2 G_{\text{out}}/\partial \mathbf{n}'\partial \mathbf{n}$. To determine the behavior of the singularity of the difference, we omit the first term of $\partial^2 P_j/\partial \mathbf{n}'\partial \mathbf{n}$ since it is weakly singular and get

$$\begin{aligned}&\varepsilon_{\text{in}}\frac{\partial^2 G_{\text{in}}}{\partial \mathbf{n}'\partial \mathbf{n}}-\varepsilon_{\text{out}}\frac{\partial^2 G_{\text{out}}}{\partial \mathbf{n}'\partial \mathbf{n}}\\ &\simeq -\frac{e^{-\lambda_{\text{in}}|\mathbf{r}-\mathbf{r}'|}}{4\pi}(\lambda_{\text{in}}\frac{1}{|\mathbf{r}-\mathbf{r}'|}+\frac{1}{|\mathbf{r}-\mathbf{r}'|^2})\frac{\partial^2|\mathbf{r}-\mathbf{r}'|}{\partial \mathbf{n}'\partial \mathbf{n}}\\ &+\frac{e^{-\lambda_{\text{out}}|\mathbf{r}-\mathbf{r}'|}}{4\pi}(\lambda_{\text{out}}\frac{1}{|\mathbf{r}-\mathbf{r}'|}+\frac{1}{|\mathbf{r}-\mathbf{r}'|^2})\frac{\partial^2|\mathbf{r}-\mathbf{r}'|}{\partial \mathbf{n}'\partial \mathbf{n}}.\end{aligned} \tag{71}$$

We proceed by approximating the exponential term as

$$e^{-\lambda|\mathbf{r}-\mathbf{r}'|} = 1 - \lambda|\mathbf{r}-\mathbf{r}'| + O(|\mathbf{r}-\mathbf{r}'|^2) \tag{72}$$

to obtain

$$\begin{aligned}
&\varepsilon_{ins}\partial^2 G_{ins}/\partial\mathbf{n}\partial\mathbf{n}' - \varepsilon_{out}\partial^2 G_{out}/\partial\mathbf{n}\partial\mathbf{n}' \\
&\simeq -\frac{1-\lambda_{ins}|\mathbf{r}-\mathbf{r}'|}{4\pi}(\lambda_{ins}\frac{1}{|\mathbf{r}-\mathbf{r}'|} + \frac{1}{|\mathbf{r}-\mathbf{r}'|^2})\frac{\partial^2|\mathbf{r}-\mathbf{r}'|}{\partial\mathbf{n}'\partial\mathbf{n}} \\
&+ \frac{1-\lambda_{out}|\mathbf{r}-\mathbf{r}'|}{4\pi}(\lambda_{out}\frac{1}{|\mathbf{r}-\mathbf{r}'|} + \frac{1}{|\mathbf{r}-\mathbf{r}'|^2})\frac{\partial^2|\mathbf{r}-\mathbf{r}'|}{\partial\mathbf{n}'\partial\mathbf{n}} \\
=& -\frac{1}{4\pi}(\lambda_{ins}^2 - \lambda_{out}^2)\frac{\partial^2|\mathbf{r}-\mathbf{r}'|}{\partial\mathbf{n}'\partial\mathbf{n}}
\end{aligned} \tag{73}$$

Finally, we can see that

$$\varepsilon_{\text{in}}\frac{\partial^2 G_{\text{in}}}{\partial\mathbf{n}'\partial\mathbf{n}} - \varepsilon_{\text{out}}\frac{\partial^2 G_{\text{out}}}{\partial\mathbf{n}'\partial\mathbf{n}} = O(\frac{1}{|\mathbf{r}-\mathbf{r}'|}). \tag{74}$$

In summary, all the integrands for our second kind integral equations have, at most, a weak singularity and the integral can be correctly calculated by means of a local polar transformation centered at the singularity.

2.7 Numerical Results

We first specify various numerical parameters for our numerical tests. The mesh size is specified by a single number n, which is the number of times the azimuthal angle, the height of the cylinder, and the angle of inclination in the semi-sphere are subdivided. Moreover, to ensure no points are evaluated on the interfaces at $z = 0$ or $z = D$ (to avoid ambiguity for the dielectric constants), we shift the mesh points on the interfaces in the z direction by 10^{-14}. For calculating the Sommerfeld integral (10) in the definition of Green's functions of a layered medium, we truncate the length

Table 2: Quadrature rule used for a given example and mesh size.

Physical domain	Mesh size n	Gauss-Kronrod points	Symmetric Gauss points
Dielectric sphere	< 32	81	N/A
	64	289	N/A
Janus particle	< 32	81	N/A
	64	289	N/A
Ion channel	< 32	N/A	42

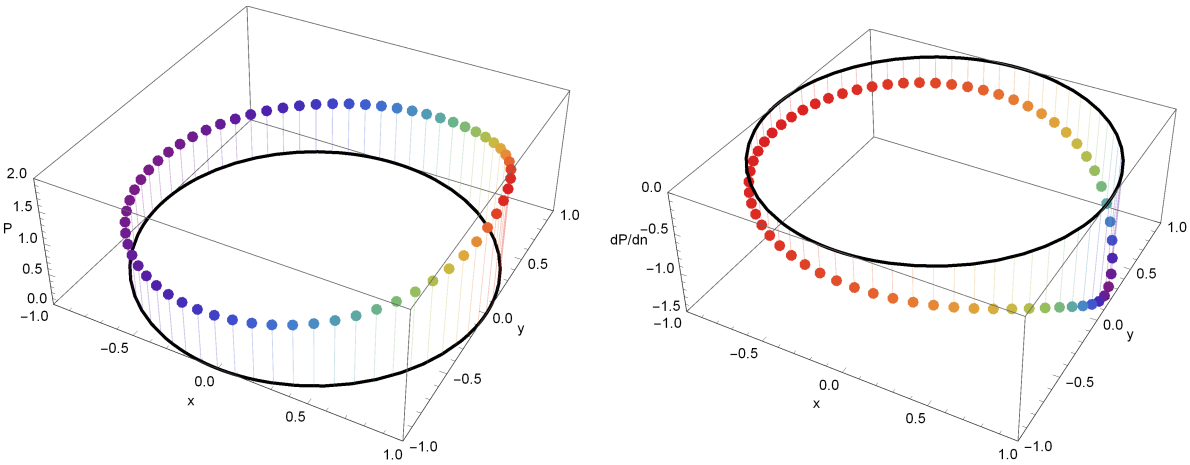

Figure 8: Potential (left) and its derivative (right) on the dielectric sphere's boundary when $z = 0$ and the charge is inside the sphere at $(0.5, 0.1, 0.2)$.

from infinity to 80 and use 10 subintervals with 30 Gaussian quadrature points per subinterval. The number of regular quadrature points used depends on the mesh parameter, as shown in Table 2. The quadrature rule for the weakly singular integrals uses 256 points if the singularity is at a vertex and 512 points if the singularity is on an edge.

2.7.1 Dielectric Sphere

To illustrate the method's ability to capture different values of ε inside and outside the physical domain, we consider a dielectric sphere where $\varepsilon_{\text{in}} = 2$, $\varepsilon_{\text{out}} = 1$, $\lambda = 0$, and the source charge is located at $\mathbf{r}' = (0.5, 0.1, 0.2)$ with magnitude 1. In this case, the mathematical domain is just a sphere. For the charge inside the sphere, the true

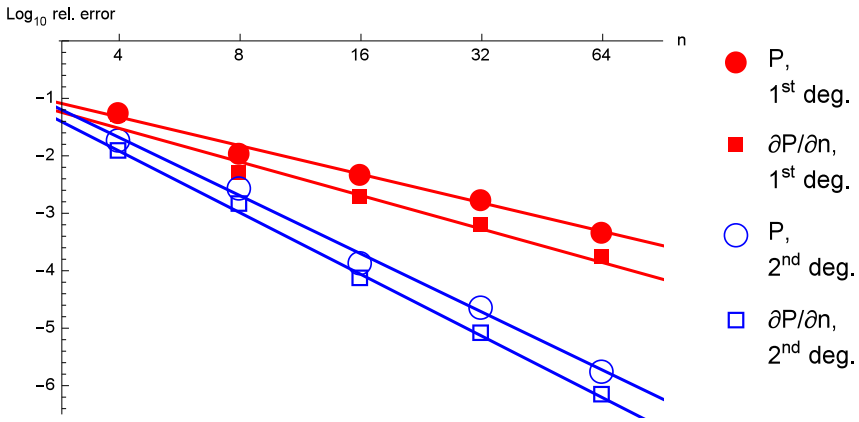

Figure 9: Convergence of the potential and its normal derivatives on the dielectric sphere's boundary with the charge inside the sphere at $(0.5, 0.1, 0.2)$ as the mesh size n increases. The points mark our results and the lines are linear fits.

Table 3: Relative error and convergence rate r of the potential and its normal derivative on the dielectric sphere's boundary; the charge is inside the sphere at $(0.5, 0.1, 0.2)$.

	Potential				Derivative			
	1^{st} degree		2^{nd} degree		1^{st} degree		2^{nd} degree	
Mesh	Rel. error	r	Rel. error	r	Rel. error	r	Rel. error	r
2	2.2×10^{-1}	N/A	2.5×10^{-2}	N/A	2.0×10^{-1}	N/A	2.2×10^{-2}	N/A
4	5.7×10^{-2}	2.0	1.9×10^{-2}	0.4	4.7×10^{-2}	2.1	1.1×10^{-2}	1.0
8	1.1×10^{-2}	2.4	2.7×10^{-3}	2.8	4.6×10^{-3}	3.3	1.3×10^{-3}	3.1
16	4.8×10^{-3}	1.2	1.8×10^{-4}	4.3	1.8×10^{-3}	1.4	7.9×10^{-5}	4.0
32	1.7×10^{-3}	1.5	2.3×10^{-5}	2.6	5.8×10^{-4}	1.6	7.5×10^{-6}	3.5
64	4.7×10^{-4}	1.9	1.8×10^{-6}	3.7	1.6×10^{-4}	1.8	6.4×10^{-7}	3.6

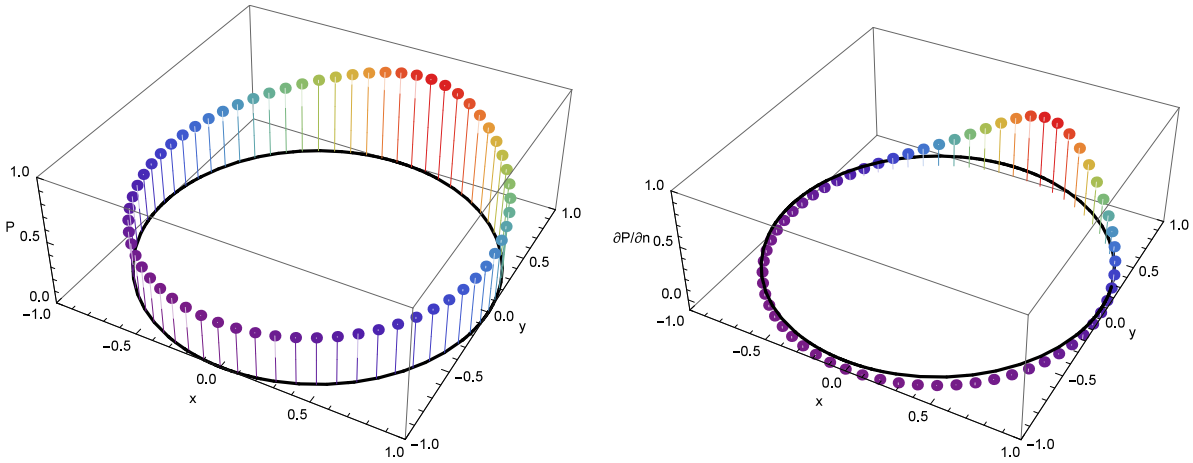

Figure 10: Potential (left) and its derivative (right) on the dielectric sphere's boundary when $z = 0$ and the charge is outside the sphere at $(0.5, 2, 0.2)$.

solution at the boundary is

$$\phi_{\text{true}}(\mathbf{r}) = \frac{1+\gamma}{2\varepsilon_{in}} \sum_{m=0}^{\infty} |\mathbf{r}_s|^m \left(2 + \frac{2\gamma}{1-\gamma+2m}\right) P_m(\cos\theta), \tag{75}$$

where $\gamma = (\varepsilon_{\text{in}} - \varepsilon_{\text{out}})/(\varepsilon_{\text{in}} + \varepsilon_{\text{out}})$, $\mathbf{r}_s$ is the source charge's location, θ is the angle between $\mathbf{r}$ and $\mathbf{r}_s$, and P_m is the m^{th} order Legendre polynomial [7]. Basis functions of degree 1 and 2 are used with the number of mesh divisions $n = 2$, 4, 8, 16, 32, and 64, respectively. A cross-section at $z = 0$ of our results is given in Fig. 8 when $n = 64$ and the basis degree is 2. Convergence to the true solution as the mesh is refined is given in Fig. 9 and Table 3.

Next we consider the case when $\mathbf{r}' = (0.5, 2, 0.2)$ is outside the dielectric sphere. In this case, the BIE takes the form

$$\begin{aligned}\phi_{\text{in}}(\mathbf{p}) = &\int_S \left[\varepsilon_{\text{in}}(\mathbf{r}) G_{\text{in}}(\mathbf{r},\mathbf{p}) - \varepsilon_{\text{in}}(\mathbf{r}) G_{\text{out}}(\mathbf{r},\mathbf{p})\right] \frac{\partial \phi_{\text{in}}(\mathbf{r})}{\partial \mathbf{n}} dS(\mathbf{r}) \\ &- \int_S \left[\varepsilon_{\text{in}}(\mathbf{r}) \frac{\partial G_{\text{in}}(\mathbf{r},\mathbf{p})}{\partial \mathbf{n}} - \varepsilon_{\text{out}}(\mathbf{r}) \frac{\partial G_{\text{out}}(\mathbf{r},\mathbf{p}')}{\partial \mathbf{n}}\right] \phi_{\text{in}}(\mathbf{r}) dS(\mathbf{r}) \\ &+ 4\pi \sum_{i=1}^{N} q_i G_{\text{out}}(\mathbf{r}_i, \mathbf{p}),\end{aligned} \tag{76}$$

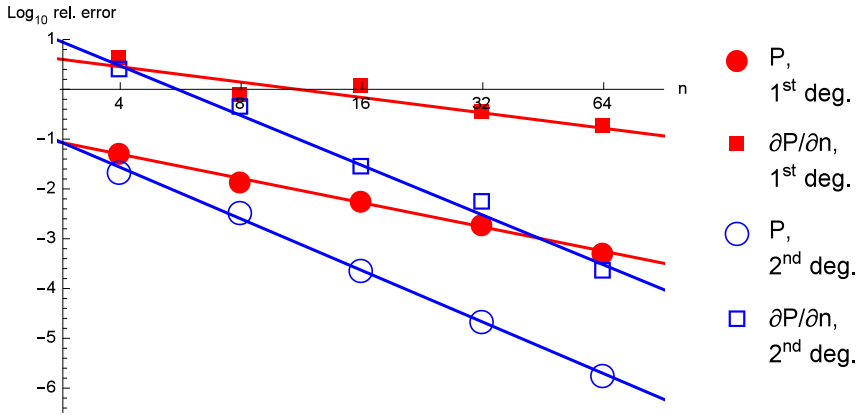

Figure 11: Convergence of potential and its normal derivative on the dielectric sphere's boundary with the charge outside the sphere at $(0.5, 2, 0.2)$ as the mesh size n increases. The points mark our results and the lines are linear fits.

Table 4: Relative error and convergence rate r of the potential and its normal derivative on the dielectric sphere's boundary; the charge is outside the sphere at $(0.5, 2, 0.2)$.

	Potential				Derivative			
	1^{st} degree		2^{nd} degree		1^{st} degree		2^{nd} degree	
Mesh	Rel. error	r	Rel. error	r	Rel. error	r	Rel. error	r
2	1.5×10^{-1}	N/A	1.2×10^{-1}	N/A	6.2×10^{-1}	N/A	3.7×10^{-1}	N/A
4	5.2×10^{-2}	1.5	2.2×10^{-2}	2.5	3.9×10^{0}	-2.6	2.3×10^{0}	-2.6
8	1.4×10^{-2}	1.9	3.3×10^{-3}	2.7	6.9×10^{-1}	2.5	4.0×10^{-1}	2.5
16	5.7×10^{-3}	1.3	2.3×10^{-4}	3.9	1.1×10^{0}	-0.7	2.5×10^{-2}	4.0
32	1.9×10^{-3}	1.6	2.2×10^{-5}	3.4	3.1×10^{-1}	1.8	5.0×10^{-3}	2.3
64	5.2×10^{-4}	1.9	1.8×10^{-6}	3.6	1.6×10^{-1}	0.9	2.0×10^{-4}	4.6

$$\begin{aligned}\left(\frac{1}{2}+\frac{1}{2}\frac{\varepsilon_{\text{in}}(\mathbf{p})}{\varepsilon_{\text{out}}(\mathbf{p})}\right)&\frac{\partial\phi_{\text{in}}(\mathbf{p})}{\partial\mathbf{n}'}\\ &=\int_S\left[\varepsilon_{\text{in}}(\mathbf{r})\frac{\partial G_{\text{in}}(\mathbf{r},\mathbf{p})}{\partial\mathbf{n}'}-\varepsilon_{\text{in}}(\mathbf{r})\frac{\partial G_{\text{out}}(\mathbf{r},\mathbf{p})}{\partial\mathbf{n}'}\right]\frac{\partial\phi_{\text{in}}(\mathbf{r})}{\partial\mathbf{n}}dS(\mathbf{r})\\ &\quad-\int_S\left[\varepsilon_{\text{in}}(\mathbf{r})\frac{\partial^2 G_{\text{in}}(\mathbf{r},\mathbf{p})}{\partial\mathbf{n}'\partial\mathbf{n}}-\varepsilon_{\text{out}}(\mathbf{r})\frac{\partial^2 G_{\text{out}}(\mathbf{r},\mathbf{p})}{\partial\mathbf{n}'\partial\mathbf{n}}\right]\phi_{\text{in}}(\mathbf{r})dS(\mathbf{r})\\ &\quad+4\pi\sum_{i=1}^{N}q_i\frac{\partial G_{\text{out}}(\mathbf{r}_i,\mathbf{p})}{\partial\mathbf{n}'},\end{aligned}\tag{77}$$

and the true solution on the boundary is given by

$$\phi_{\text{true}}(\mathbf{r})=\frac{1-\gamma}{2\varepsilon_{\text{out}}}\sum_{m=0}^{\infty}\frac{1}{|\mathbf{r}_s|^{m+1}}\left(2+\frac{2\gamma}{1-\gamma+2m}\right)P_m(\cos(\theta)),\tag{78}$$

where $\gamma=(\varepsilon_{\text{in}}-\varepsilon_{\text{out}})/(\varepsilon_{\text{in}}+\varepsilon_{\text{out}})$, $\mathbf{r}_s$ is the source charge's location, θ is the angle between $\mathbf{r}$ and $\mathbf{r}_s$, and P_m is the m^{th} order Legendre polynomial [7]. A cross-section at $z=0$ of the results with a 2^{nd} degree basis and mesh parameter 64 is given in Fig. 10. Convergence to the true solution as the mesh is refined is given in Fig. 11 and Table 4. Convergence may slow when the source charge is too close to the dielectric sphere as the potential becomes more singular near the spherical boundary.

2.7.2 Janus Particle

In the next examples, we will compute the electric potential around a Janus particle. A Janus particle is a sphere made up of two semi-spheres, each having a different dielectric constant ε. Janus particles have attracted much attention as an efficient and distinctive means to accomplish complex self-assembled materials and realize properties not possible by homogeneous particles or symmetric patchy particles [40].

For simplicity, we take $\lambda=0$ and $\varepsilon_{\text{out}}=1$ in three cases to be considered. In the first case, $\varepsilon_{\text{in}}=2$ in the lower half of the particle and $\varepsilon_{\text{in}}=2.1$ in the upper half

Table 5: Relative error and convergence rate r of the potential on the two planes $x = 0$ and $x = 1.2$ for the Janus particle. The reference solution is obtained from when the mesh parameter is 64.

	$\varepsilon_{top} = 2.1, \varepsilon_{bottom} = 2$				$\varepsilon_{top} = 18, \varepsilon_{bottom} = 3.9$			
	1^{st} degree		2^{nd}degree		1^{st}degree		2^{nd}degree	
Mesh	Rel. error	r	Rel. error	r	Rel. error	r	Rel. error	r
2	7.9×10^{-1}	N/A	7.3×10^{-1}	N/A	3.6×10^{0}	N/A	3.6×10^{0}	N/A
4	2.0×10^{-1}	2.0	9.7×10^{-2}	2.9	1.3×10^{0}	1.4	4.8×10^{-1}	2.9
8	2.5×10^{-2}	3.0	2.3×10^{-2}	2.1	9.8×10^{-2}	3.8	5.4×10^{-2}	3.1
16	2.7×10^{-3}	3.2	1.6×10^{-3}	3.9	4.4×10^{-2}	1.1	2.1×10^{-2}	1.4
32	6.0×10^{-4}	2.2	1.5×10^{-4}	3.4	1.5×10^{-2}	1.5	3.9×10^{-3}	2.4

to test convergence. In the second case, $\varepsilon_{\text{in}} = 3.9$ in the lower half and $\varepsilon_{\text{in}} = 18$ in the upper half to simulate realistic conditions. Last, we take $\varepsilon_{\text{in}} = 2$ in the lower half and $\varepsilon_{\text{in}} = 80$ in the upper half to illustrate an extreme case. We will use the BIEs for a charge outside the sphere, given by (76) and (77) since we place the source charge at $(1, 1, 1)$. Fig. 12 shows the potential inside the Janus particles for the three cases while Fig. 13 shows the convergence of the potential for both cross-sections at $z = 0$ (the reference solution is obtained numerically on the mesh $n = 64$). The small condition number of the matrix and number of iterations GMRES required for convergence show the benefit of the second kind integral equation formulation. Table 6 gives the condition numbers κ and the number of iterations N the GMRES solver took to solve the linear system for the first case.

2.7.3 Ion Channel

In the hybrid model for an ion channel, we consider the following setup, as shown in Fig. 14. Let the cylinder's radius be 4 and its height 12. Inside the cylinder, let $\varepsilon_0 = 1$ and $\lambda_0 = 0$. In the upper layer, let $\varepsilon_1 = 80$ and $\lambda_1 = 2.5$. Outside the cylinder in the middle layer, let $\varepsilon_2 = 2$ and $\lambda_2 = 0$. In the upper layer, let $\varepsilon_3 = 80$

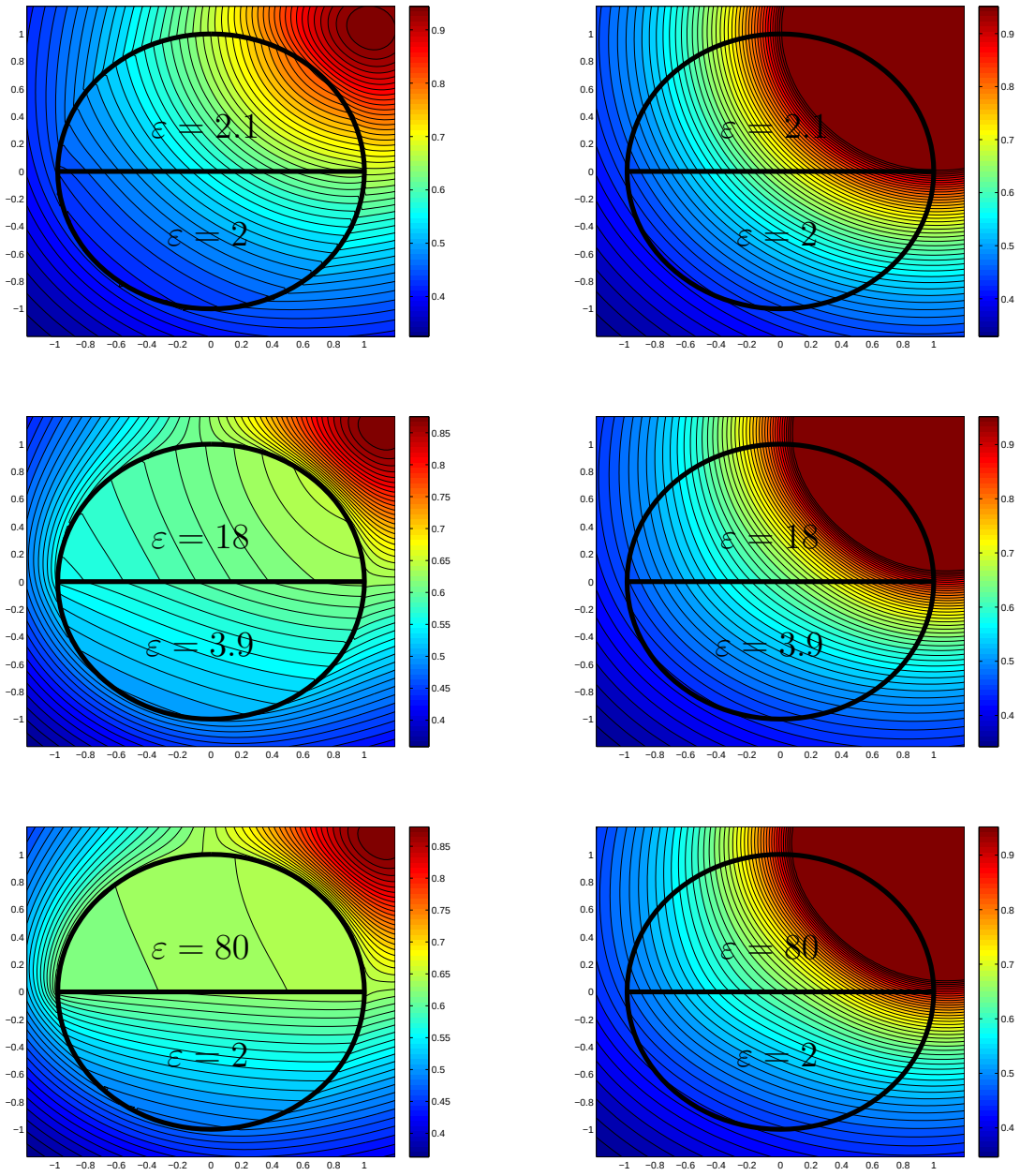

Figure 12: Potential in and around Janus particles when $x = 0$ (left) and when $x = 1.2$ (right) for various values of ε.

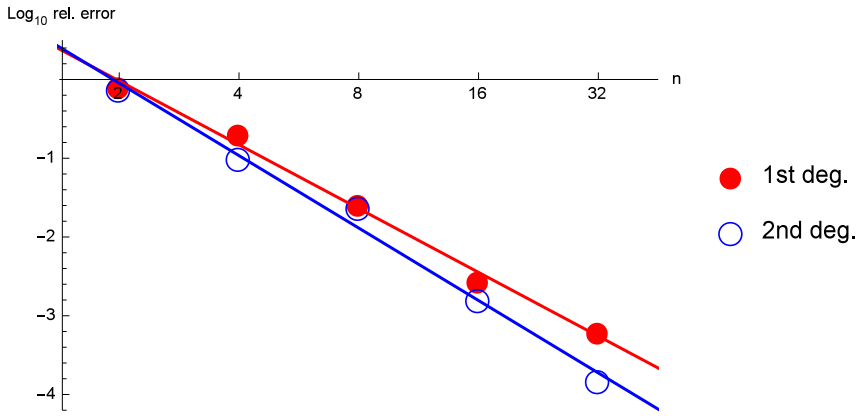

Figure 13: Convergence of the potential in a Janus particle when ε is perturbed by 10^{-1} in the upper hemisphere as the mesh size n increases. The points mark our results and the lines are linear fits.

Table 6: Condition number κ and number of iterations N to solve the matrix equation corresponding to the Janus particle with a perturbation of 10^{-1}.

			BIE 1st kind				BIE 2nd kind			
	Matrix sizes		1st degree		2nd degree		1st degree		2nd degree	
Mesh	1st degree	2nd degree	κ	N	κ	N	κ	N	κ	N
2	16	52	13.8	4	34.2	8	2.8	1	3.2	9
4	60	228	25.1	31	63.3	49	2.8	9	3.2	9
8	244	964	68.3	52	167.2	65	2.8	9	3.3	9
16	996	3972	244.0	65	605.5	90	2.8	9	3.4	9
32	4036	16132	948.6	78	2358.9	134	2.8	9	3.4	9
64	16260	65028	3761.6	99	9345.4	217	2.8	9	3.4	9

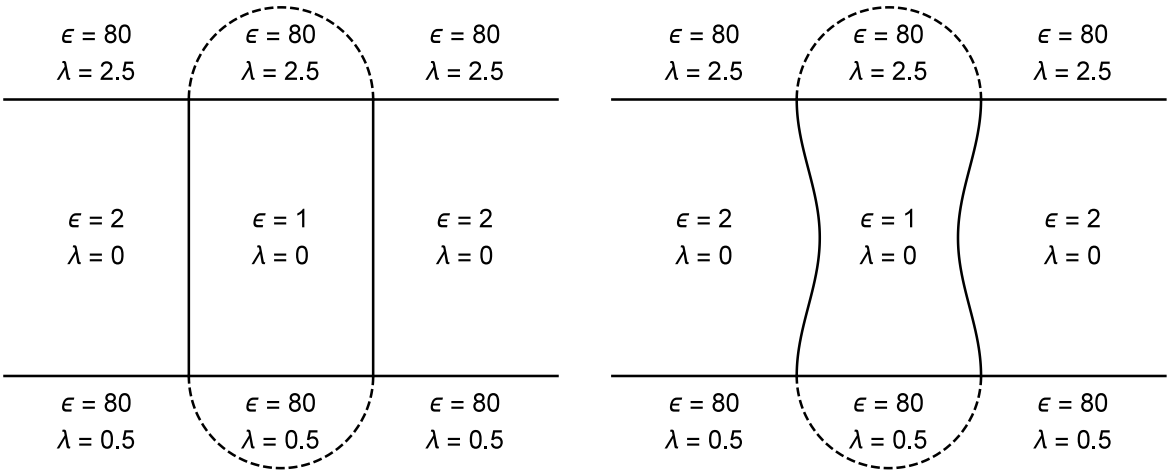

Figure 14: Schematic illustration of model setup for an ion channel with a cylindrical boundary (left) and with a deformed boundary (right).

and $\lambda_1 = 0.5$.

We place 19 source charges along the cylinder's axis of magnitude 1 at $z = 1.5$, 2.0 , ..., 10.5. The true solution of the potential is unknown and a reference solution is calculated on a fine mesh $n = 16$.

First, we calculate the self-energy of a point charge given by

$$V(\mathbf{r}_s) = q_s \phi_{\text{rf}}(\mathbf{r}_s)/2, \tag{79}$$

where the reaction field $\phi_{\text{rf}}(\mathbf{r}_s)$ at the source charge location is the total potential field minus the primary Coulomb potential produced by the source charge q_s itself. Fig. 15 (left) shows the self-energy when calculated using a 2^{nd} degree basis and the reference solution calculated on the mesh $n = 16$ while Fig. 16 (left) shows the convergence of the self-energy with respect to the reference solution as the mesh is refined for both sets of basis functions.

Second, the potential is calculated at 19 interior points at the positions of the

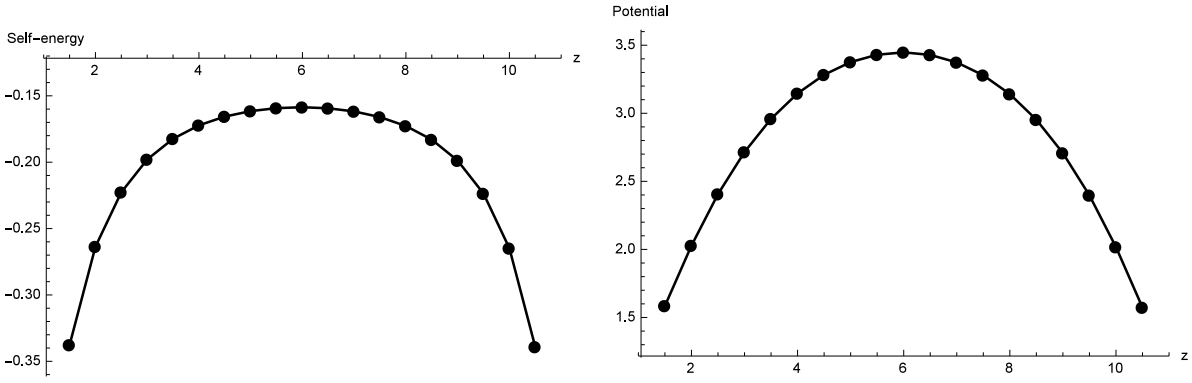

Figure 15: Self-energy (left) and potential (right) in the ion channel with cylindrical sides, calculated using BIE of the 2nd kind, 2nd degree basis, and mesh parameter 16.

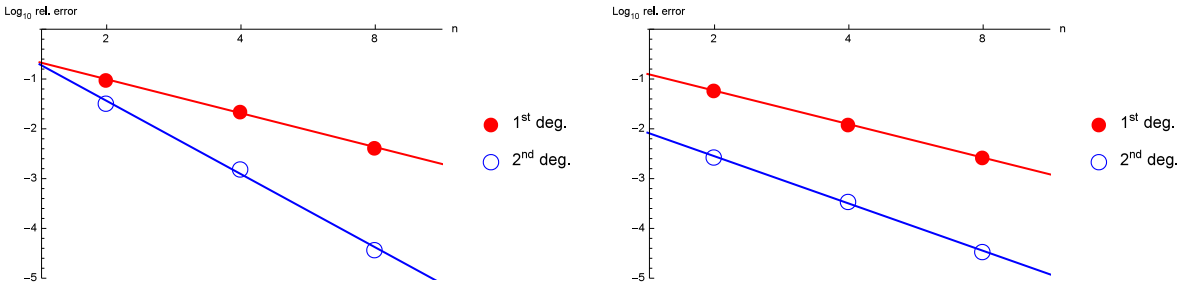

Figure 16: Convergence of the self-energy (left) and potential (right) inside the ion channel with cylindrical sides using BIE of the 2nd kind as the mesh size n increases. The points mark our results and the lines are linear fits.

Table 7: Relative error and convergence rate r of the potential and self-energy for the ion channel with a cylindrical boundary using BIEs of the 2^{nd} kind. The reference solution is obtained from when the mesh parameter is 16.

	Potential				Self-energy			
	1^{st} degree		2^{nd}degree		1^{st}degree		2^{nd}degree	
Mesh	Rel. error	r	Rel. error	r	Rel. error	r	Rel. error	r
2	5.9×10^{-2}	N/A	2.7×10^{-3}	N/A	9.5×10^{-2}	N/A	3.2×10^{-2}	N/A
4	1.2×10^{-2}	2.3	3.4×10^{-4}	3.0	2.2×10^{-2}	2.1	1.5×10^{-3}	4.4
8	2.7×10^{-3}	2.2	3.4×10^{-5}	3.3	4.1×10^{-3}	2.4	3.7×10^{-5}	5.4

Table 8: Condition number κ and number of iterations N to solve matrix equation corresponding to the ion channel with a cylindrical boundary.

			BIE 1^{st} kind				BIE 2^{nd} kind			
	Matrix sizes		1^{st} degree		2^{nd} degree		1^{st} degree		2^{nd} degree	
Mesh	1^{st} degree	2^{nd} degree	κ	N	κ	N	κ	N	κ	N
2	24	84	12.5	12	33.8	30	1.4	6	1.5	9
4	92	356	23.7	25	62.2	43	1.5	9	1.5	9
8	372	1476	66.0	42	164.7	64	1.5	10	1.5	10
16	1508	6020	238.6	60	598.6	101	1.5	10	1.5	10

source locations shifted by 2 in the positive x direction. Fig. 15 (right) shows the potential when calculated using a 2^{nd} degree basis and mesh parameter $n = 16$ while Fig. 16 (right) shows the convergence of the potential as the mesh is refined for both sets of basis functions. Table 6 summarizes the errors and convergence rate for this case.

Finally, it is noteworthy that the Sommerfeld integral is computationally expensive, especially for the second derivative of the Green's function. In order to justify the use of BIEs of the second kind, Table 8 gives the condition numbers κ and the number of iterations N the GMRES solver took to solve the linear system. Obviously, the lower condition number and number of iterations required demonstrate that BIEs of the second kind will result in a significantly more stable matrix equation.

In an attempt to match the physical shape of an ion channel more accurately, we

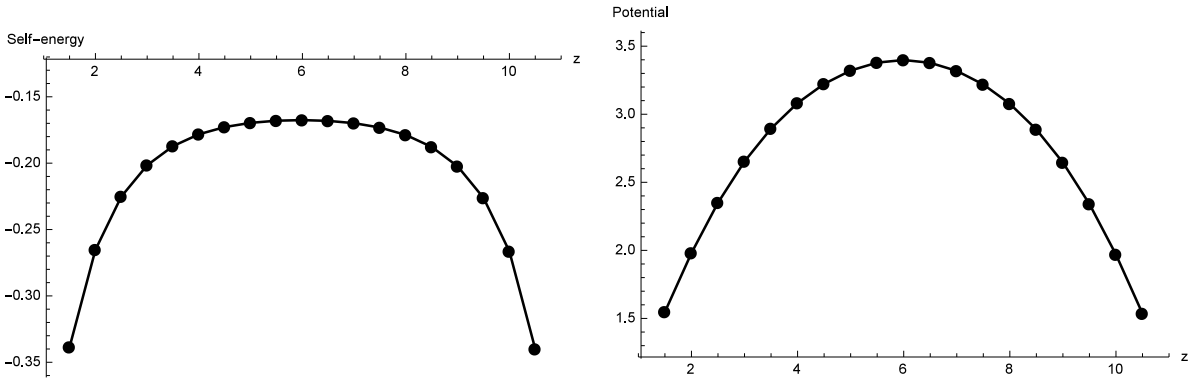

Figure 17: Self-energy (left) and potential (right) in the ion channel with deformed sides, calculated using BIE of the 2nd kind, 2nd degree basis, and mesh parameter 16.

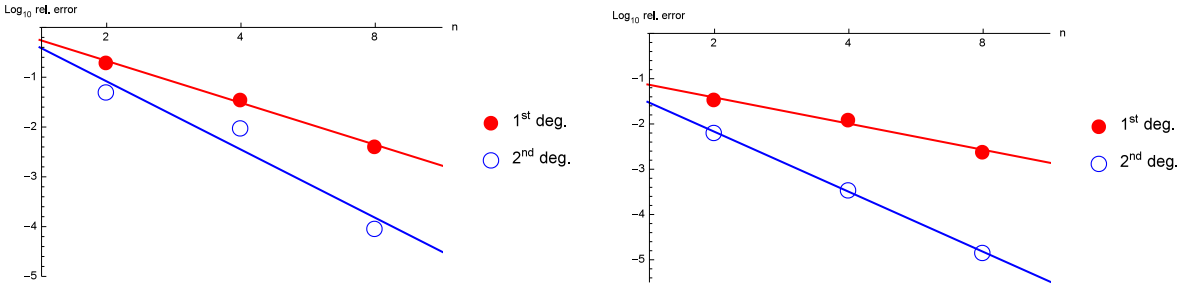

Figure 18: Convergence of the self-energy (left) and potential (right) inside the ion channel with deformed sides using BIE of the 2nd kind as the mesh size n increases. The points mark our results and the lines are linear fits.

repeat the calculations for the ion channel except the cylindrical part of the domain is deformed so that it is narrower in the region that the selectivity filter of a biological KcsA ion channel would be located. Specifically, we apply the mapping

$$f(\rho,\theta,z)=\left(\frac{\rho}{8}\left(\cos\left(\frac{2\pi z}{3}\right)+7\right),\theta,z\right) \tag{80}$$

to the cylindrical region so the radial direction decreases to three-fourths of its maximum value halfway up the cylinder, as shown in Fig. 14. Results are shown in Figs. 17 and 18. Table 8 summarizes the errors and convergence rate for this case. Similar information concerning the condition number of the matrix as in Table 8 is found in this case.

Table 9: Relative error and convergence rate r of the potential and self-energy for the ion channel with a deformed boundary using BIEs of the 2nd kind. The reference solution is obtained from when the mesh parameter is 16.

	Potential				Self-energy			
	1st degree		2nddegree		1stdegree		2nddegree	
Mesh	Rel. error	r	Rel. error	r	Rel. error	r	Rel. error	r
2	3.5×10^{-2}	N/A	6.4×10^{-3}	N/A	2.0×10^{-1}	N/A	5.0×10^{-2}	N/A
4	1.2×10^{-2}	1.5	3.5×10^{-4}	4.2	3.6×10^{-2}	2.5	9.5×10^{-3}	2.4
8	2.4×10^{-3}	2.4	1.4×10^{-5}	4.6	4.1×10^{-3}	3.1	9.1×10^{-5}	6.7

2.8 Future Work Concerning the PB Equation

Work has already begun on obtaining better convergence rates for when the singularity is outside and close to the boundary. We begin by performing a change of variables on the PB equation (1). Let $H(\mathbf{r}) = 4\pi \sum_{k=1}^{N} q_k G_{out}(\mathbf{r}, \mathbf{r}_k)$. Then define

$$w(\mathbf{r}) = \begin{cases} \phi_{out}(\mathbf{r}) - H(\mathbf{r}) & \text{if } \mathbf{r} \in \Omega_{out} \\ \\ \phi_{ins}(\mathbf{r}) & \text{if } \mathbf{r} \in \Omega_{ins} \end{cases} \tag{81}$$

so that the PB equation is

$$\varepsilon[\nabla^2 w(\mathbf{r}) - \lambda^2 w(\mathbf{r})] = 0. \tag{82}$$

The advantage in this approach lies in the fact that $w_{out}(\mathbf{r})$ is not near-singular on the boundary. This can be seen by recognizing that the singular part of ϕ behaves the same as the free-space Green's function. Since

$$w_{out}(\mathbf{r}) = \phi_{out}(\mathbf{r}) - 4\pi \sum_{k=1}^{N} q_k G_{out}(\mathbf{r}, \mathbf{r}_k), \tag{83}$$

the singularity has been removed by subtraction. What remains is the part of ϕ due to inhomogeneities in the dielectric material. A comparison of the smoothness is given in Fig. 19 when the singularity is close to the boundary of the dielectric sphere in

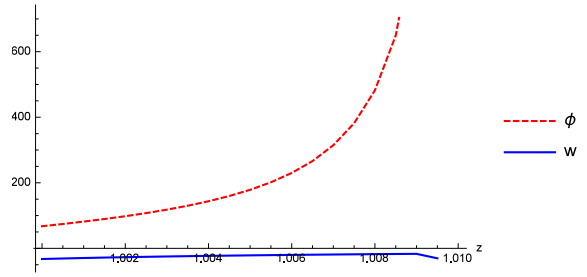

Figure 19: ϕ_{out} contains a singularity and is difficult to solve for. w_{out} is smooth. The source charge is at $(0, 0, 1.01)$.

section 2.7.1. This is similar to the approaches in [10] [11].

We are also interested in performing a molecular dynamics (MD) simulation. Our BIE method for the PB equation can calculate the potential at any location. The potential can be used to calculate the electric field, which can then be used to calculate the force $\mathbf{F} = q\mathbf{E}$ at the desired point. MD simulations of Janus particles provide information on how colloidal solutions can be manipulated. MD simulations of ion channels provide information on the path particles take through the channel as well as information concerning the selectivity filter. Moreover, if the boundary in the BIE does not move, the matrix does not have to be recalculated and each step of the MD simulation only requires the right-hand side of the matrix equation to be calculated and the matrix equation to be solved. The boundary in the ion channel model has no physical significance; it only denotes where the atomistic region ends and the implicit continuum region begins. Thus, MD of the ion channel could be handled efficiently by our method and more source charges could be placed to accurately model the proteins that make up the ion channel's wall and selectivity filter.

The Sommerfeld integral in (10) is difficult when the $z - z'$ is small. Specifically, we calculate the Sommerfeld integral by truncating its length to a small number, say

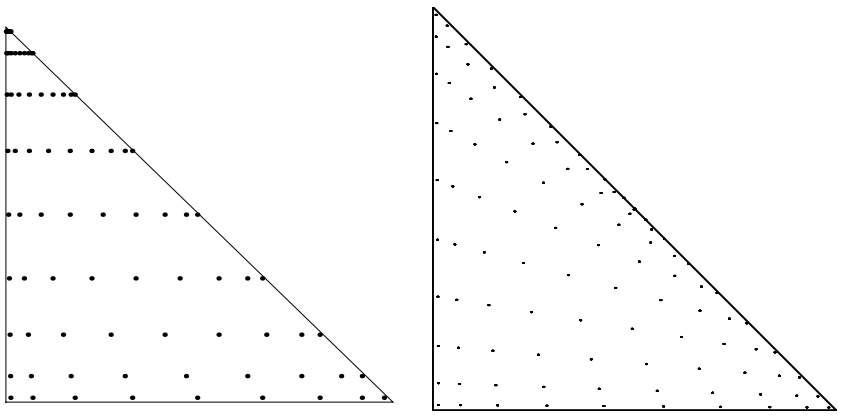

Figure 20: Points on a triangle for regular integration with the sample points mapped from a square by collapsing the top edge (left) and the new mapping that avoids clustering (right).

80. When $z - z'$ is small, say 10^{-4}, we can maintain the same level of accuracy by increasing the truncation length. However, doing so requires many more function evaluations and increases the runtime significantly. Thus, the ion channel model, which is the only model that requires the Sommerfeld integral, can be made more accurate and efficient through the introduction of a window function, similar to the ones described in [46].

Finally, one of the quadrature rules for regular integrals is inefficient because the sample points are clustered near one vertex; they are shown on the left of Fig. 20. Instead of using (67) to map from a square to a triangle, we can use

$$(\xi, \eta) \to \left(\xi - \frac{\xi\eta}{2}, y - \frac{\xi\eta}{2}\right), \tag{84}$$

which avoids clustering the sample points near any one vertex. A plot of the sample points is given on the right side of Fig. 20. The Jacobian for this bilinear mapping is $1-\xi/2-\eta/2$. Beginning with this new mapping, we would like to further modify it so that for a singularity $\mathbf{r}'$ and elemental mapping Γ, the difference $\mathbf{r}'_z - \Gamma(\xi - \xi\eta/2, y -$

$\xi\eta/2)_z$ is as large as possible to assist in accurately calculating the Sommerfled integral in (10).

2.9 Summary for Modeling with the PB Equation

In this chapter we have proposed a well-conditioned hypersingular integral equation method for computing the electrostatic potential in the presence of inhomogeneities embedded in layered media for ionic (Poisson-Boltzmann equations) or non-ionic (Poisson equations) systems with applications in biomolecular solvation and colloidal solutions. Due to the Müller's subtraction approach, the resulting second kind integral equations only involves $O(1/r)$ singularities which can be treated easily with a local polar coordinate transform. Numerical results for Janus particles and an ion channel model have shown the robustness and desired accuracy of the proposed method with both first and second order basis.

CHAPTER 3: SINGULAR INTEGRALS IN THREE DIMENSIONS

3.1 Calculation of Integrals with Singular Kernels

The computation of hypersingular integrals associated with CPVs is the most time consuming and challenging task in solving integral equations for many mathematical physics equations, for example, Maxwell equations, elasticity equations, etc. The CPV is defined by the integration of the singular function by first excluding a small volume around the singularity, then letting the size of the exclusion volume shrink to zero to produce the CPV. Namely, the CPV is defined as

$$\text{p.v.} \int_{\Omega} \frac{f(\mathbf{r})}{|\mathbf{r}-\mathbf{r}'|^k} d\mathbf{r} = \lim_{\delta \to \mathbf{0}} \int_{\Omega \backslash V_\delta(\mathbf{r}')} \frac{f(\mathbf{r})}{|\mathbf{r}-\mathbf{r}'|^k} d\mathbf{r}, \tag{85}$$

where Ω is a bounded domain in R^3 assumed to be a cube, rectangular prism, cylinder, sphere, or ellipsoid in this chapter and $V_\delta(\mathbf{r}')$ is an exclusion volume centered at $\mathbf{r}'$ of spherical shape of radius δ.

The objective of this chapter is to develop an accurate and efficient quadrature formula to compute the integral over $\Omega \backslash V_\delta(\mathbf{r}')$ in (85). We will closely follow [48]. For any fixed $\delta > 0$, the integral over domain $\Omega \backslash V_\delta(\mathbf{r}')$ can be calculated by a naive brute-force approach to a given accuracy if a large number of sample points are used. Fortunately, the function $f(\mathbf{r})$ in the numerator, which can take a general form in the integral equation method, is often smooth; therefore, $f(\mathbf{r})$ can be well represented through an interpolation of its values on the three-dimensional tensor product of

1-D Gauss quadrature or midpoint nodes. Using this simple fact, any brute-force integration quadrature involving a large number of values of $f(\mathbf{r})$ can be converted into an equivalent quadrature formula using only values at the small number of nodes of a tensor-product form in Ω. Moreover, the new weights on the tensor-product nodes can be pre-computed and tabulated to be used for a general function $f(\mathbf{r})$. This will be the approach in this chapter, and the resulting weights have been used to calculate the matrix entries for a discretized Nyström VIE for Maxwell equations in Chapter 4, where the issue of CPV limit is also addressed. There are other approaches in computing the CPV in (85), including direct evaluations of hypersingular integrals [38]. Moreover, similar work has been done in one dimension using modified Newton-Cotes integration rules in [24][45][42][14][37][41][26][25].

3.2 Quadrature Formula over Tensor-Product Nodes

Consider a hypersingular integrand formed by the product of some smooth function $f(\mathbf{r})$ with a singular kernel $1/|\mathbf{r}-\mathbf{r}'|^k$ over a domain Ω, where the singularity is at $\mathbf{r}' \in \Omega$ and k can be 1, 2, or 3, i.e.,

$$\int_{\Omega \setminus V_\delta(\mathbf{r}')} \frac{f(\mathbf{r})}{|\mathbf{r}-\mathbf{r}'|^k} d\mathbf{r}. \tag{86}$$

First, assume we have an N point quadrature rule that uses points $\hat{\mathbf{r}}_i$ and weights $\hat{w}_i$,

$$\int_{\Omega \setminus V_\delta(\mathbf{r}')} \frac{f(\mathbf{r})}{|\mathbf{r}-\mathbf{r}'|^k} d\mathbf{r} \approx \sum_{i=1}^{N} \frac{f(\hat{\mathbf{r}}_i)}{|\hat{\mathbf{r}}_i-\mathbf{r}'|^k} \hat{w}_i. \tag{87}$$

As the function $f(\mathbf{r})$ is generally smooth, it can be well approximated through an interpolation of its values over a small number of tensor-product nodes $\{\mathbf{r}_i\}|_{i=1}^{M}$. Letting $\phi_j(\mathbf{r})$ denote a set of M basis functions that satisfy the Kronecker delta

property $\phi_j(\mathbf{r}_i) = \delta_{i,j}$, we have the following approximation:

$$f(\mathbf{r}) \approx \sum_{j=1}^{M} f(\mathbf{r}_j)\phi_j(\mathbf{r}). \tag{88}$$

Then, we can manipulate (86) as follows:

$$\begin{aligned}\int_{\Omega\setminus V_\delta(\mathbf{r}')} \frac{f(\mathbf{r})}{|\mathbf{r}-\mathbf{r}'|^k} d\mathbf{r} &\approx \sum_{i=1}^{N} \frac{f(\hat{\mathbf{r}}_i)}{|\hat{\mathbf{r}}_i-\mathbf{r}'|^k}\hat{w}_i \approx \sum_{i=1}^{N}\left(\sum_{j=1}^{M}\frac{f(\mathbf{r}_j)\phi_j(\hat{\mathbf{r}}_i)}{|\hat{\mathbf{r}}_i-\mathbf{r}'|^k}\hat{w}_i\right) \\ &= \sum_{j=1}^{M} f(\mathbf{r}_j)\left(\sum_{i=1}^{N}\frac{\phi_j(\hat{\mathbf{r}}_i)}{|\hat{\mathbf{r}}_i-\mathbf{r}'|^k}\hat{w}_i\right).\end{aligned} \tag{89}$$

Therefore, we obtain an M-point quadrature formula over the tensor-product nodes as follows:

$$\int_{\Omega\setminus V_\delta(\mathbf{r}')} \frac{f(\mathbf{r})}{|\mathbf{r}-\mathbf{r}'|^k} d\mathbf{r} \approx \sum_{j=1}^{M} f(\mathbf{r}_j) w_{j,k}, \tag{90}$$

where the quadrature weights are given by

$$w_{j,k} = \sum_{i=1}^{N} \frac{\phi_j(\hat{\mathbf{r}}_i)}{|\hat{\mathbf{r}}_i-\mathbf{r}'|^k}\hat{w}_i. \tag{91}$$

It can be easily seen that the weight is a quadrature approximation for the following integral

$$w_{j,k} \simeq \int_{\Omega\setminus V_\delta(\mathbf{r}')} \frac{\phi_j(\mathbf{r})}{|\mathbf{r}-\mathbf{r}'|^k} d\mathbf{r}. \tag{92}$$

It should be noted that $w_{j,k}$ can be precalculated. In the appendix, a method of using rotation matrices is given for the purpose of reducing the number of quadrature tables that need to be saved. Moreover, in our implementation of the quadrature rule in (87), we use spherical coordinates in a region around $\mathbf{r}'$; $\hat{w}_i$ then contains the Jacobian $|\hat{\mathbf{r}}_i - \mathbf{r}'|^2$ when $\hat{\mathbf{r}}_i$ is near $\mathbf{r}'$, which reduces the order of the singularity. When k is less than 3, the limit in (85) can be evaluated once this Jacobian is applied and the

size δ of the exclusion volume $V_\delta(\mathbf{r}')$ can be taken to be zero. As M is usually small ($M << N$) in the interpolation formula (88) for $f(\mathbf{r})$, the new quadrature formula (90) will be fast, using only a small number of samples. The error committed in (90) is twofold: error occurs when we use the initial brute-force quadrature rule to approximate the integral in (87), which can be controlled by increasing the number N, and when we approximate $f(\mathbf{r})$ by using basis functions $\phi_j(\mathbf{r})$ and the samples $f(\mathbf{r}_j)$. However, if the basis $\phi_j(\mathbf{r})$ is the same one used to approximate the solution of, for example, a VIE by a Nyström collocation method, then the error due to interpolating $f(\mathbf{r})$ will be of the same order as expected in the underlying Nyström VIE method.

Finally, it is desirable to make a reference domain $\Omega \backslash V_\delta(\mathbf{r}')$ for calculating the integral over some different sized domain $\hat{\Omega}$ where the mapping from $\Omega \backslash V_\delta(\mathbf{r}')$ to $\hat{\Omega}$ is given by $\gamma(\mathbf{r}) = a\mathbf{r}$ for some a. Then the Jacobian is given by $J_\gamma = a^{3-k}$ so that (90) becomes

$$\int_{\hat{\Omega}} \frac{f(\mathbf{r})}{|\mathbf{r} - \mathbf{r}'|^k} d\mathbf{r} \approx \sum_{j=1}^{M} f(\gamma(\mathbf{r}_j)) J_\gamma w_{j,k}. \tag{93}$$

This is because the sum over i in (89) is calculated on the reference element. If an exclusion $V_\delta(\mathbf{r}')$ is present, care should be taken to be aware of any deformation caused by the mapping, if any.

3.3 M-Point Tensor-Product Quadratures for a Cube or Rectangular Prism

For the cube, we first introduce a brute-force method for integrating when the singularity is at the center of the cube. Second, we consider when the singularity is not at the center and proceed by subdividing so that a subcube exists whose center coincides with the singularity. Third, we give a set of basis functions defined on the

cube for interpolation.

3.3.1 Quadrature Rule when the Singularity $\mathbf{r}'$ is at the Center of the Cube

In the derivation of (90) for a cube, we take $\Omega = [-1, 1]^3$. We proceed by subdividing Ω so that we have six pyramids P_i, $i = 1, 2, \ldots, 6$, each using a different side of the cube as its base and $\mathbf{r}' = (0, 0, 0)$ for its pinnacle. Since we wish to use spherical coordinates (ρ, φ, θ) to reduce the singularity of the kernel, we rewrite (92) as

$$\begin{aligned}\int_{\Omega \setminus V_\delta(\mathbf{r}')} \frac{\phi_j(\mathbf{r})}{|\mathbf{r}-\mathbf{r}'|^k} d\mathbf{r} &= \sum_{i=1}^{6} \int_{P_i \setminus V_\delta(\mathbf{r}')} \frac{\phi_j(\mathbf{r})}{|\mathbf{r}-\mathbf{r}'|^k} d\mathbf{r} \\ &= \sum_{i=1}^{6} \int_{\rho_{i,min}}^{\rho_{i,max}} \int_{\theta_{i,min}}^{\theta_{i,max}} \int_{\varphi_{i,min}}^{\varphi_{i,max}} \frac{\phi_j(\mathbf{r})}{|\mathbf{r}-\mathbf{r}'|^k} \rho^2 \sin(\theta) d\varphi d\theta d\rho.\end{aligned} \tag{94}$$

For the pyramid with a base at $x = 1$, the limits of integration are

$$\begin{aligned}&\varphi_{min} = -\tfrac{\pi}{4}, \quad \theta_{min} = \tfrac{\pi}{2} - \tan^{-1}(\cos(\varphi)), \quad \rho_{min} = \delta, \\ &\varphi_{max} = \tfrac{\pi}{4}, \quad \theta_{max} = \tfrac{\pi}{2} + \tan^{-1}(\cos(\varphi)), \quad \rho_{max} = \tfrac{1}{\cos(\varphi)\sin(\theta)}.\end{aligned} \tag{95}$$

We now define several mappings from $[0, 1]$, where we have n one-dimensional Gauss points and weights (t_ℓ, w_ℓ^t), to the variables of integration in (95).

Working with the pyramid whose base satisfies $x = 1$, we map a Gauss point-weight pair (t_k, w_k^t) to its corresponding azimuthal angle and weight (φ_k, w_k^φ) by

$$\varphi_k = \tfrac{\pi}{4}(t_k - 1), \qquad w_k^\varphi = w_k^t. \tag{96}$$

Next, for a fixed angle φ_k, we map a Gauss point-weight pair (t_j, w_j^t) to its corre-

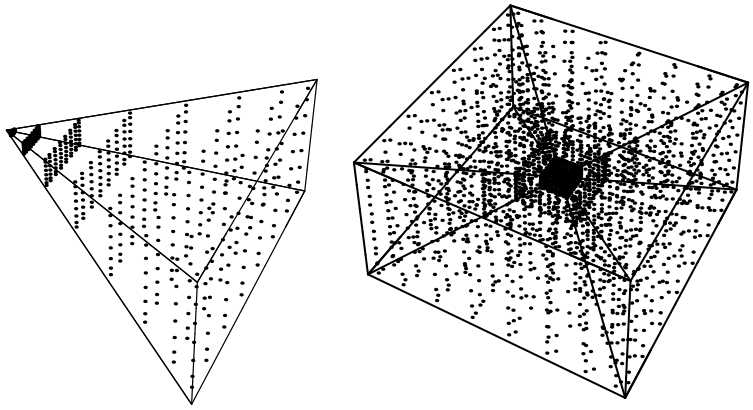

Figure 21: Quadrature points on the pyramid with base satisfying $x = 1$ (left) and on the cube $[-1, 1]^3$ (right).

sponding angle of inclination and weight (θ_j, w_j^θ) by

$$\begin{aligned} \theta_{j,k} &= 2\tan^{-1}(\cos(\varphi_k))t_j + \frac{\pi}{2} - \tan^{-1}(\cos(\varphi_k)), \\ w_{j,k}^\varphi &= 2\tan^{-1}(\cos(\varphi_k))w_j^t. \end{aligned} \tag{97}$$

For fixed angles φ_k and θ_j, we map a Gauss point-weight pair (t_i, w_i^t) to its corresponding radius and weight (ρ_i, w_i^r) by

$$\begin{aligned} \rho_{i,j,k} &= \left(\frac{1}{\cos(\varphi_k)\sin(\theta_{j,k})} - \rho_{min}\right) t_i + \rho_{min}, \\ w_{i,j,k}^\rho &= \left(\frac{1}{\cos(\varphi_k)\sin(\theta_{j,k})} - \rho_{min}\right) w_i^t, \end{aligned} \tag{98}$$

where $\rho_{min} = \delta$ if a sphere around the singularity is excluded. Otherwise, $\rho_{min} = 0$. Matching indices, we now have a set of n^3 points and weights on the pyramid given by

$$\{(\rho_{i,j,k}, \theta_{j,k}, \varphi_k) : 1 \le i, j, k \le n\},\ \{w_{i,j,k}^\rho w_{j,k}^\theta w_k^\varphi : 1 \le i, j, k \le n\}. \tag{99}$$

Finally, the points are converted to Cartesian coordinates. The quadrature points on the remaining five pyramids can either be handled by the same method or can be

calculated from these points and weights by a rotation. We take the latter approach. For $n = 8$, the resulting quadrature points are plotted in Fig. 21. In total, there are $N = 6n$ sample points in the cube on the right of Fig. 21. While the points are mostly symmetrical, the y-coordinates differ from the z-coordinates slightly in the pyramid on the left. If desired, a more symmetrical quadrature rule could be found without difficulty.

3.3.2 Quadrature Rule when the Singularity $\mathbf{r}'$ is not at the Center of the Cube

There are two straightforward approaches for the case when $\mathbf{r}'$ is not at the center of the cube. One way is to modify the formulas for finding the quadrature points on the pyramids so that the pyramids are deformed; in this case, each pyramid should be calculated independently instead of using a rotation as before. However, this will result in some pyramids that are too flat to be integrated accurately if the singularity is located near the edge of the cube. As our primary goal is to compute the integral near the singularity accurately, we implemented a second way where a subcube is made with the singularity at its center; the remaining regions of the parent cube $[-1, 1]^3$ are subdivided and integrated using the cross-product of n_{reg} Gauss points and weights (t_ℓ, w_ℓ^t) defined on a reference cube $[0, 1]^3$ by

$$\begin{aligned} &\{(t_i, t_j, t_k) : 1 \le i, j, k \le n_{reg}\}, \\ &\{w_i^t w_j^t w_k^t : 1 \le i, j, k \le n_{reg}\}. \end{aligned} \tag{100}$$

We take the subcube with the singularity at its center to be the largest contained in the parent cube $[-1, 1]^3$. In our implementation, this means that if the singularity is at the center of the parent cube, the subcube is identical to the parent cube. If the

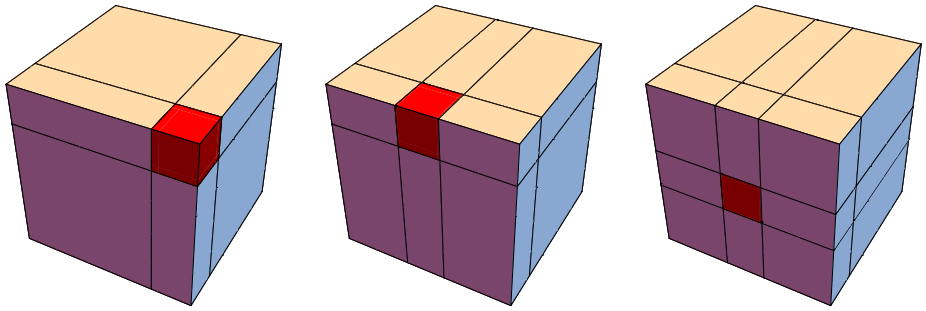

Figure 22: From left to right, the illustrations correspond to subdivisions when the singularity is in a corner, near an edge, and at the center of a face. The subcube with a singularity is red.

singularity is equidistant from three adjacent faces of the parent cube, it is in a corner and we calculate 7 additional nonsingular integrals. If the singularity is equidistant from two adjacent faces, it is near an edge and we calculate 11 additional integrals. Otherwise, we calculate 17 additional integrals so N is given by

$$N \leq 6n^3 + 17n_{reg}^3. \tag{101}$$

Illustrations of these cases are shown in Fig. 22. The integral in (92) can be rewritten to include I nonsingular subregions R_i, $i = 1, 2, \ldots, I$, as

$$\begin{aligned}\int_{\Omega\setminus V_\delta(\mathbf{r}')} \frac{\phi_j(\mathbf{r})}{|\mathbf{r}-\mathbf{r}'|^k} d\mathbf{r} &= \sum_{i=1}^{6} \int_{P_i\setminus V_\delta(\mathbf{r}')} \frac{\phi_j(\mathbf{r})}{|\mathbf{r}-\mathbf{r}'|^k} d\mathbf{r} + \sum_{i=1}^{I} \int_{R_i} \frac{\phi_j(\mathbf{r})}{|\mathbf{r}-\mathbf{r}'|^k} d\mathbf{r} \\ &= \sum_{i=1}^{6} \int_{\rho_{i,min}}^{\rho_{i,max}} \int_{\theta_{i,min}}^{\theta_{i,max}} \int_{\varphi_{i,min}}^{\varphi_{i,max}} \frac{\phi_j(\mathbf{r})}{|\mathbf{r}-\mathbf{r}'|^k} \rho^2 \sin(\theta) d\varphi d\theta d\rho \\ &+ \sum_{i=1}^{I} \int_{x_{i,min}}^{x_{i,max}} \int_{y_{i,min}}^{y_{i,max}} \int_{z_{i,min}}^{z_{i,max}} \frac{\phi_j(\mathbf{r})}{|\mathbf{r}-\mathbf{r}'|^k} dz dy dx,\end{aligned} \tag{102}$$

where the union of the regions P_i make up the singular subcube, requiring $\rho_{i,max}$ to be scaled appropriately.

These additional subregions allow Ω to be a rectangular prism, if desired. None of the subregions should have a dimension that is significantly larger than one of its

other dimensions; otherwise this could lead to an inaccurate approximation over the subregion. Our code provides the option to allow further subdivision in case this is an issue.

3.3.3 M-Point Tensor-Product Quadratures for a Cube

To construct the quadrature weights defined in (91) for a set of tensor-product nodes corresponding to 1-D Gauss points on $[-1, 1]$, we will first define the interpolation functions. We use the cross-product of Lagrange polynomials defined on $[-1, 1]$ for interpolation. Thus, we use

$$\{(2t_i - 1, 2t_j - 1, 2t_k - 1) : 1 \leq i, j, k \leq m\} \tag{103}$$

for our $M = m^3$ interpolation points $\mathbf{r}_j$ in $\mathbb{R}^3$, where t_ℓ are the m gauss points defined on $[0, 1]$. For the x-axis, the i^{th} Lagrange polynomial is given by

$$\ell_i^x(x) = \prod_{1 \leq p \leq m, p \neq i} \frac{x - t_p}{t_i - t_p}. \tag{104}$$

The polynomials for y and z are similar. The resulting three-dimensional Lagrange polynomials are given by

$$L_{i,j,k}(\mathbf{r}) = \ell_i^x(x)\ell_j^y(y)\ell_k^z(z). \tag{105}$$

Renaming and reindexing $L_{i,j,k}(\mathbf{r})$ as $\phi_j(\mathbf{r})$, we get a set of basis functions that satisfies (88). Then, we use our N-point quadrature rule over the cube to integrate the basis functions against the singular kernel as in (91). This produces the weights $w_{j,k}$. Finally, the integral over the cube $[-1, 1]^3$ is given by (90). The degree of the one-dimensional basis functions can be set independently in case one dimension is much

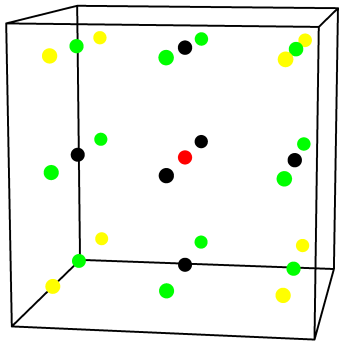

Figure 23: Interpolation points, colored to show rotationally symmetric points, on the cube when $m = 3$ and $M = 27$.

larger than another one, as is sometimes the case for a rectangular prism.

3.4 M-Point Tensor-Product Quadratures for a Cylinder

Interpolation points will never coincide with the center of the cylinder. Thus, under the assumption that the singularity will be at an interpolation point, we disregard the possibility that subdivisions are unnecessary. Similar to the cube, we first work with the case when the singularity is at the center of a cylinder, but this cylinder will always be mapped to a subcylinder. Second, we define the required subdivisions explicitly. Third, we give basis functions on the cylinder for interpolation.

3.4.1 Quadrature Rule for a Subcylinder Centered at the Singularity $\mathbf{r}'$

We begin with a cylinder of radius 1 whose bases satisfy $z = -1$ and $z = 1$. For now, let the singularity $\mathbf{r}' = (0, 0, 0)$ be at the center of the cylinder. The cylinder can be subdivided into two cones C_1 and C_2 with the same bases as the cylinder and a third subregion C_3 that contains the sides of the cylinder. Using spherical coordinates

(ρ, φ, θ) to reduce the singularity of the kernel, (92) becomes

$$\int_{\Omega \setminus V_\delta(\mathbf{r}')} \frac{\phi_j(\mathbf{r})}{|\mathbf{r}-\mathbf{r}'|^k} d\mathbf{r} = \sum_{i=1}^{3} \int_{C_i \setminus V_\delta(\mathbf{r}')} \frac{\phi_j(\mathbf{r})}{|\mathbf{r}-\mathbf{r}'|^k} d\mathbf{r} \tag{106}$$
$$= \left[\int_\delta^{\frac{1}{\cos(\theta)}} \int_0^{\frac{\pi}{4}} + \int_\delta^{\frac{1}{\sin(\theta)}} \int_{\frac{\pi}{4}}^{\frac{3\pi}{4}} + \int_\delta^{-\frac{1}{\cos(\theta)}} \int_{\frac{3\pi}{4}}^{\pi} \right] \int_0^{2\pi} \frac{\phi_j(\mathbf{r}) \rho^2 \sin(\theta)}{|\mathbf{r}-\mathbf{r}'|^k} d\varphi d\theta d\rho.$$

Let the n one-dimensional Gauss points and weights over $[0, 1]$ be denoted by (t_ℓ, w_ℓ^t). For the azimuthal angle,

$$\varphi_k = 2\pi \left(k + \frac{1}{2} \right) / n, \quad w_k^\varphi = 2\pi k / n. \tag{107}$$

The angle of inclination is divided into three regions. For the cone with an apex at the singularity and the base at $z = 1$,

$$\theta_j = \frac{\pi}{4} t_j, \quad w_j^\theta = \frac{\pi}{4} w_j^t. \tag{108}$$

For the cone with an apex at the singularity and the base at $z = -1$,

$$\theta_j = \frac{\pi}{4} t_j + \frac{3\pi}{4}, \quad w_j^\theta = \frac{\pi}{4} w_j^t. \tag{109}$$

For the remaining region along the sides of the cylinder,

$$\theta_j = \frac{\pi}{2} t_j + \frac{\pi}{4}, \quad w_j^\theta = \frac{2\pi}{4} w_j^t. \tag{110}$$

Combining the n points for θ in each region, we use $3n$ points to integrate in the θ direction. Since ρ depends on θ, its formula changes depending on the region. For the upper cone, let $\rho_j^{max} = 1/\cos(\theta_j)$. For the lower cone, let $\rho_j^{max} = -1/\cos(\theta_j)$. For the remaining side regions, let $\rho_j^{max} = 1/\sin(\theta_j)$. Then the points and weights for ρ

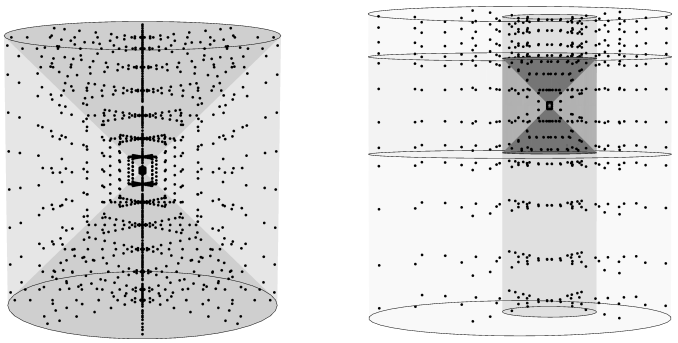

Figure 24: Quadrature points for the subcylinders. Left: The subcylinder with $\mathbf{r}'$ at its center when $n = 8$; right: all subcylinders when $\mathbf{r}' = (0.2, 0.3, 0.4)$ when $n = n_{cyl} = n_w = 4$.

are given by

$$\begin{aligned} \rho_{i,j} &= \left(\rho_j^{max} - \rho_{min}\right) t_i + \rho_{min}, \\ w_{i,j}^{\rho} &= \left(\rho_j^{max} - \rho_{min}\right) w_i^t, \end{aligned} \tag{111}$$

where $\rho_{min} = \delta$ if a sphere around the singularity is excluded. Otherwise, $\rho_{min} = 0$. Thus, this cylinder with the singularity at its center uses a total of $3n^3$ points given by

$$\begin{aligned} &\{(\rho_{i,j}, \theta_j, \varphi_k) : 1 \le i, k \le n, 1 \le j \le 3n\}, \\ &\{w_{i,j}^{\rho} w_j^{\theta} w_k^{\varphi} : 1 \le i, k \le n, 1 \le j \le 3n\}, \end{aligned} \tag{112}$$

which can be seen on the left of Fig. 24.

3.4.2 Quadrature Rule for all Subcylinders not Containing the Singularity $\mathbf{r}'$

We subdivide the cylinder into a total of three cylindrical regions and three washer-shaped regions, even if the singularity is at the center of the parent cylinder. Before subdividing, the distances from the three boundaries of the parent cylinder to the exclusion $V_\delta(\mathbf{r}')$ are measured. Let d be half of the minimum of the three distances.

First, the radial direction ρ^{cyl}, measured from the singularity, is divided into two intervals with boundaries 0, $d+\delta$, and ρ^{cyl}_{max}, where

$$\rho^{cyl}_{max}(\varphi) = -\rho'(\varphi) + \sqrt{1 - \mathbf{r}'^2_x - \mathbf{r}'^2_y + \rho'^2(\varphi)} \tag{113}$$

and

$$\rho'(\varphi) = \mathbf{r}'_x \cos(\varphi) + \mathbf{r}'_y \sin(\varphi). \tag{114}$$

This results in a cylindrical core containing the singularity with a washer, whose hole may be off center, wrapped around it. Second, the height of the parent cylinder is divided into the three intervals with boundaries at -1, $\mathbf{r}'_z - d - \delta$, $\mathbf{r}'_z + d + \delta$, and 1. The resulting six regions, with quadrature points, can be seen on the right of Fig. 24. Let S_1 and S_2 be the nonsingular subcylinders, given in cylinderical coordinates (ρ, φ, z) as $S_1 = [0, d+\delta] \times [0, 2\pi] \times [\mathbf{r}'_z + d + \delta, 1]$, $S_2 = [0, d+\delta] \times [0, 2\pi] \times [-1, \mathbf{r}'_z - d - \delta]$, and let W_1, W_2, W_3 be the washers, given in cylindrical coordinates as $W_1 = [d + \delta, \rho^{cyl}_{max}] \times [0, 2\pi] \times [\mathbf{r}'_z + d + \delta, 1]$, $W_2 = [d+\delta, \rho^{cyl}_{max}] \times [0, 2\pi] \times [\mathbf{r}'_z - d - \delta, \mathbf{r}'_z + d + \delta]$, $W_3 = [d+\delta, \rho^{cyl}_{max}] \times [0, 2\pi] \times [-1, \mathbf{r}'_z - d - \delta]$. Then (92) becomes

$$\begin{aligned}
&\int_{\Omega \setminus V_\delta(\mathbf{r}')} \frac{\phi_j(\mathbf{r})}{|\mathbf{r} - \mathbf{r}'|^k} d\mathbf{r} \\
&= \left(\int_\delta^{\frac{d+\delta}{\cos\theta}} \int_0^{\frac{\pi}{4}} + \int_\delta^{\frac{d+\delta}{\sin\theta}} \int_{\frac{\pi}{4}}^{\frac{3\pi}{4}} + \int_\delta^{-\frac{d+\delta}{\sin\theta}} \int_{\frac{3\pi}{4}}^{\pi} \right) \int_0^{2\pi} \frac{\phi_j(\mathbf{r}) \rho^2 \sin\theta}{|\mathbf{r} - \mathbf{r}'|^k} d\varphi d\theta d\rho \\
&+ \sum_{i=1}^{2} \int_{S_i} \frac{\phi_j(\mathbf{r})}{|\mathbf{r} - \mathbf{r}'|^k} \rho d\varphi dz d\rho + \sum_{i=1}^{3} \int_{W_i} \frac{\phi_j(\mathbf{r})}{|\mathbf{r} - \mathbf{r}'|^k} \rho d\varphi dz d\rho.
\end{aligned} \tag{115}$$

Only the middle subcylinder contains a singularity; the quadrature rule for it is described in the previous subsection and is mapped to this region. The remaining regions can be integrated in cylindrical coordinates (ρ^{cyl}, φ, z), with Gaussian quadra-

ture used in ρ^{cyl} and z, and the midpoint rule in φ. Specifically, with Gauss point-weights (t_ℓ, w_ℓ^t) defined on $[0,1]$, each cylinder with no singularity uses n_{cyl}^3 points and weights in cylindrical coordinates given by

$$\begin{aligned} &\{(t_i, \frac{2\pi(j+0.5)}{n_{cyl}}, t_k) : 1 \le i,j,k \le n_{cyl}\}, \\ &\{\frac{2\pi}{n_{cyl}} w_i^t w_k^t : 1 \le i,j,k \le n_{cyl}\}. \end{aligned} \tag{116}$$

Using n_w^ρ, n_w^φ, and n_w^z to denote the number of points on the washer regions in each direction, the quadrature points and weights are given in cylindrical coordinates by

$$\begin{aligned} &\{(t_i, \frac{2\pi(j+0.5)}{n_w^\varphi}, t_k) : 1 \le i \le n_w^\rho, 1 \le j \le n_w^\varphi, 1 \le k \le n_w^z\}, \\ &\{\frac{2\pi}{n_w^\varphi} w_i^t w_k^t : 1 \le i \le n_w^\rho, 1 \le j \le n_w^\varphi, 1 \le k \le n_w^z\}. \end{aligned} \tag{117}$$

Since it is best to use twice as many points in the φ direction, let $n_w = n_w^\rho$ so that a total of $2n_w^3$ points and weights are on each washer. Counting all six subregions, the cylinder uses a total of $N = 3n^3 + 2n_{cyl}^3 + 6n_w^3$ points; the points and weights are converted to Cartesian coordinates. Our code provides the option to allow further subdivisions in case a cylinder or washer has a dimension that is significantly larger than one of its other dimensions.

3.4.3 M-Point Tensor-Product Quadratures for a Cylinder

To construct the quadrature weights defined in (91) for a set of tensor-product nodes corresponding to 1-D Gauss points on $[-1,1]$ or uniform points over $[0,2\pi]$, we will first define the interpolation functions. We will use Lagrange interpolation in ρ and z and Fourier interpolation for φ. Let m_ρ, m_φ, and m_z be the number of sample points in ρ^{cyl}, φ, and z, respectively. Since twice as many points are needed in the φ

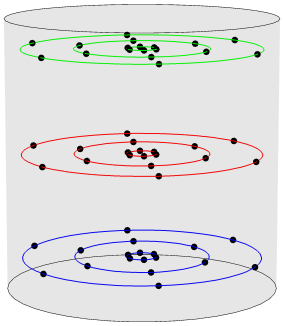

Figure 25: Interpolation points on the cylinder with circles when φ is a free variable and $m = 3$ and $M = 54$.

direction, let $m = m_\rho$ so that $M = 2m^3$ sample points are used. Shown in Fig. 25, the interpolation points are

$$\{(t_i, \frac{2\pi(j+0.5)}{m_\varphi}, t_k) : 1 \le i \le m_\rho, 1 \le j \le m_\varphi, 1 \le k \le m_z\}, \tag{118}$$

where t_ℓ are the Gauss points defined on $[0, 1]$. For the basis functions, let $\ell_i^\rho(\rho)$ be the i^{th} Lagrange polynomial for ρ, given by

$$\ell_i^\rho(\rho) = \prod_{1 \le p \le m_\rho, p \ne i} \frac{\rho - t_p}{t_i - t_p}. \tag{119}$$

The k^{th} Lagrange polynomial for z is similar. The Fourier interpolation polynomial for the φ direction can be shown to have the form

$$\ell_j^\varphi(\varphi) = \begin{cases} \frac{1}{m_\varphi} \frac{\sin(m_\varphi(\varphi-\varphi_j)/2)}{\sin((\varphi-\varphi_j)/2)} & : m_\varphi \text{ is odd and } \varphi \ne \varphi_j, \\ \frac{1}{m_\varphi} \frac{\sin(m_\varphi(\varphi-\varphi_j)/2)}{\sin((\varphi-\varphi_j)/2)} \cos((\varphi-\varphi_j)/2) & : m_\varphi \text{ is even and } \varphi \ne \varphi_j, \\ 1 & : \varphi = \varphi_j. \end{cases} \tag{120}$$

Multiplying the basis functions together yields

$$L_{i,j,k}^{cyl}(\rho, \varphi, z) = \ell_i^\rho(\rho) \ell_j^\varphi(\varphi) \ell_k^z(z). \tag{121}$$

Letting $\mathbf{r}$ be the Cartesian coordinates for (ρ, φ, z), $L_{i,j,k}(\mathbf{r}) = L^{cyl}_{i,j,k}(\rho, \varphi, z)$. Then, renaming and reindexing $L_{i,j,k}(\mathbf{r})$ as $\phi_j(\mathbf{r})$, we get a set of basis functions that satisfies (88). Next, we use our N-point quadrature rule over the cylinder to integrate the basis functions against the singular kernel, as in (91). This produces the weights $w_{j,k}$. Finally, the integral over the cylinder with radius 1 and bases satisfying $z = -1$ and $z = 1$ is given by (90).

3.5 M-Point Tensor-Product Quadratures for a Sphere

For the sphere, no subdivisions are ever made. First, we provide a brute-force quadrature rule for a singularity at any point inside the sphere. Second, we give basis functions for interpolation.

3.5.1 Quadrature Rule over a Sphere for a Singular Kernel

We consider the unit sphere for Ω. In terms of (92), we want to calculate

$$\int_{\Omega \setminus V_\delta(\mathbf{r}')} \frac{\phi_j(\mathbf{r})}{|\mathbf{r} - \mathbf{r}'|^k} d\mathbf{r} = \int_\delta^{\rho_{max}} \int_0^\pi \int_0^{2\pi} \frac{\phi_j(\mathbf{r})}{|\mathbf{r} - \mathbf{r}'|^k} \rho^2 \sin(\theta) d\varphi d\theta d\rho, \tag{122}$$

where ρ_{max} will be given later. Using spherical coordinates (ρ, φ, θ) to reduce the singularity, we use a midpoint rule for the azimuthal angle φ and Gauss quadrature for ρ and θ.

The n_φ points and weights for the azimuthal angle are given by

$$\varphi_k = 2\pi \left(k + \frac{1}{2} \right) / n_\varphi, \quad w^\varphi_k = 2\pi k / n_\varphi. \tag{123}$$

Let n_θ one-dimensional gauss points and weights over $[0, 1]$ be denoted by (t_j, w^t_j).

Then, the points and weights (θ_j, w_j^θ) for the angle of inclination are given by

$$\theta_{j,k} = \pi t_j, \quad w_{j,k}^\theta = \pi w_j^t. \tag{124}$$

For a fixed singularity $\mathbf{r}'$, let

$$\rho'(\varphi,\theta) = \mathbf{r}'_x \cos(\varphi)\sin(\theta) + \mathbf{r}'_y \sin(\varphi)\sin(\theta) + \mathbf{r}'_z \cos(\theta). \tag{125}$$

Then, in terms of φ and θ, the maximum value of ρ is given by

$$\rho_{max}(\varphi,\theta) = -\rho'(\varphi,\theta) + \sqrt{1 - \mathbf{r}'^2_x - \mathbf{r}'^2_y - \mathbf{r}'^2_z + \rho'^2(\varphi,\theta)}. \tag{126}$$

Let n_ρ one-dimensional gauss points and weights over $[0,1]$ be denoted by (t_i, w_i^t). Thus, for fixed angles φ_k and θ_j, we map a gauss point-weight pair (t_i, w_i^t) to its corresponding radius and weight (ρ_i, w_i^r) by

$$\begin{aligned} \rho_{i,j,k} &= (\rho_{max}(\varphi,\theta) - \rho_{min})\, t_i + \rho_{min}, \\ w^\rho_{i,j,k} &= (\rho_{max}(\varphi,\theta) - \rho_{min})\, w_i^t. \end{aligned} \tag{127}$$

where $\rho_{min} = \delta$ if a sphere around the singularity is excluded. Otherwise, $\rho_{min} = 0$. Matching indices, we now have a set of $N = n_\rho n_\varphi n_\theta$ points and weights on the sphere given by

$$\begin{aligned} &\{(\rho_{i,j,k}, \theta_{j,k}, \varphi_k) : 1 \le i \le n_\rho, 1 \le j \le n_\varphi, 1 \le k \le n_\theta\}, \\ &\{w^\rho_{i,j,k} w^\theta_{j,k} w^\varphi_k : 1 \le i \le n_\rho, 1 \le j \le n_\varphi, 1 \le k \le n_\theta\}. \end{aligned} \tag{128}$$

Letting $n = n_\varphi = n_\theta$, we take $n_\rho = 2n$ for a total of $N = 2n^3$ points to get the best results. The points are converted to Cartesian coordinates. A set of quadrature points on the unit sphere is depicted in Fig. 26.

A similar method can be used to find a set of quadrature points on an ellipse by scaling the axis of the ellipse to a sphere. Letting $n = n_\rho$, we take $n_\varphi = n_\theta = 2n$ for a total of $N = 4n^3$ points to get the best results. The distribution of quadrature points is similar to the distribution for the sphere, shown in Fig. 26. For an explicit description, let a, b, and c be the semi-axis length in the x, y, and z directions, respectively. Also let the ellipsoid be centered at (x_0, y_0, z_0). Then the equation for the ellipse is

$$\frac{(x-x_0)^2}{a^2} + \frac{(y-y_0)^2}{b^2} + \frac{(z-z_0)^2}{c^2} = 1. \tag{129}$$

Expanding the terms and moving the constant ones to the right, we have

$$\frac{x^2}{a^2} + \frac{y^2}{b^2} + \frac{z^2}{c^2} - \left(\frac{2xx_0}{a^2} + \frac{2yy_0}{b^2} + \frac{2zz_0}{c^2}\right) = 1 - \frac{x_0^2}{a^2} + \frac{y_0^2}{b^2} + \frac{z_0^2}{c^2}. \tag{130}$$

In spherical coordinates,

$$\begin{aligned} &\rho^2 \left(\frac{1}{a^2}\cos^2(\phi)\sin^2(\theta) + \frac{1}{b^2}\sin^2(\phi)\sin^2(\theta) + \frac{1}{c^2}\cos^2(\theta)\right) \\ &\quad - 2\rho\left(\frac{x_0\cos(\phi)\sin(\theta)}{a^2} + \frac{y_0\sin(\phi)\sin(\theta)}{b^2} + \frac{z_0\cos(\theta)}{c^2}\right) \\ &\quad = 1 - \frac{x_0^2}{a^2} - \frac{y_0^2}{b^2} - \frac{z_0^2}{c^2}. \end{aligned} \tag{131}$$

For convenience, let

$$\begin{aligned} q_1 &= \frac{x_0^2}{a^2} + \frac{y_0^2}{b^2} + \frac{z_0^2}{c^2}, \\ q_2(\varphi,\theta) &= \frac{x_0\cos(\varphi)\sin(\theta)}{a^2} + \frac{y_0\sin(\varphi)\sin(\theta)}{b^2} + \frac{z_0\cos(\theta)}{c^2}, \\ &\text{and} \\ q_3(\varphi,\theta) &= \frac{\cos^2(\varphi)\sin^2(\theta)}{a^2} + \frac{\sin^2(\varphi)\sin^2(\theta)}{b^2} + \frac{\cos^2(\theta)}{c^2} \end{aligned} \tag{132}$$

so that

$$q_3(\varphi,\theta)\rho^2 - 2q_2(\varphi,\theta)\rho = 1 - q_1. \tag{133}$$

Next, we factor out the coefficient for ρ^2 and complete the square in terms of ρ to get

$$q_3(\varphi,\theta)\left[\rho^2 - 2\frac{q_2(\varphi,\theta)}{q_3(\varphi,\theta)}\rho + \left(\frac{q_2(\varphi,\theta)}{q_3(\varphi,\theta)}\right)^2\right] = 1 - q_1 + \frac{q_2(\varphi,\theta)^2}{q_3(\varphi,\theta)}. \tag{134}$$

Solving for ρ, we arrive at

$$\rho_{max}(\varphi,\theta) = \frac{q_2(\varphi,\theta)}{q_3(\varphi,\theta)} + \sqrt{(1 - q_1 + \frac{q_2(\varphi,\theta)^2}{q_3(\varphi,\theta)})/q_3(\varphi,\theta)}. \tag{135}$$

Letting $(x_0, y_0, z_0) = -(\mathbf{r}'_x, \mathbf{r}'_y, \mathbf{r}'_z)$,

$$\rho_{max}(\varphi,\theta) = -\frac{q_2(\varphi,\theta)}{q_3(\varphi,\theta)} + \sqrt{(1 - q_1 + \frac{q_2(\varphi,\theta)^2}{q_3(\varphi,\theta)})/q_3(\varphi,\theta)}. \tag{136}$$

Letting $n = n_\rho$, we take $n_\varphi = n_\theta = 2n$ for a total of $N = 4n^3$ points to get the best results.

3.5.2 M-Point Tensor-Product Quadratures for a Sphere

Similarly, to construct the quadrature weights defined in (91) for a tensor product nodes of 1-D Gauss points on $[-1, 1]$ or uniform points over $[0, \pi]$ or $[0, 2\pi]$, we will first define the interpolation functions. We will use Lagrange polynomials in ρ and the double Fourier basis described in [34] and [4] for φ and θ. Let m_ρ, m_φ, and m_θ be the number of sample points in ρ, φ, and θ, respectively. If m is specified for the sphere then $m = m_\rho = m_\varphi = m_\theta$. Tests have shown that $m_\varphi = m_\theta$ gives the best results. Shown in Fig. 26, a brief, initial description of the interpolation points is

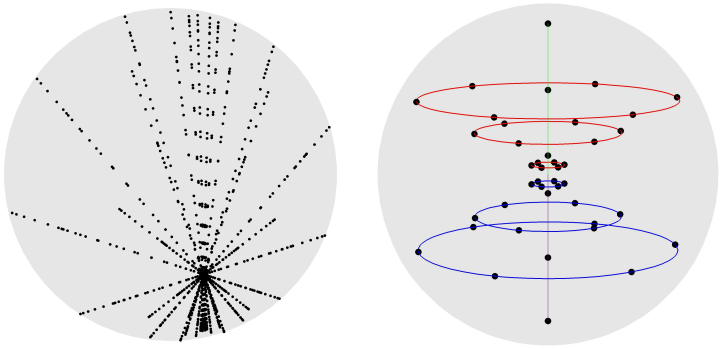

Figure 26: Sample points on the unit sphere. Left: Quadrature points when $\mathbf{r}' = (0.2, -0.3, -0.6)$ and $n = 8$; right: Interpolation points with circles when φ is a free variable, $m = 3$, and $M = 42$.

given by

$$\{(t_i, \frac{\pi j}{m_\varphi}, \frac{\pi k}{m_\theta}) : 1 \le i \le m_\rho, 0 \le j \le 2m_\varphi - 1, 0 \le k \le m_\theta\}. \tag{137}$$

where t_ℓ are the m_ρ gauss points defined on $[0, 1]$. For the basis functions, let $\ell_i^\rho(\rho)$ be the i^{th} Lagrange polynomial for ρ, given by

$$\ell_i^\rho(\rho) = \prod_{1 \le p \le m_\rho, p \ne i} \frac{\rho - t_p}{t_i - t_p}. \tag{138}$$

Defining

$$\ell_{p,q,k}^\theta(\theta) = \begin{cases} \sin(q\theta_k)\sin(q\theta) & : p \text{ is odd}, \\ \frac{1}{c_q c_k}\cos(q\theta_k)\cos(q\theta) & : p \text{ is even}, \end{cases} \tag{139}$$

where $c_q = 2$ if $q = 0$ or m_θ and $c_q = 1$ otherwise, the basis function for φ and θ is given by

$$\ell_{j,k}^{\varphi,\theta}(\varphi, \theta) = \frac{1}{m_\varphi m_\theta} \sum_{p=0}^{2m_\varphi - 1} \sum_{q=\text{mod}(p,2)}^{m_\theta - \text{mod}(p,2)} \ell_{p,q,k}^\theta(\theta) e^{i m_\varphi (\varphi - \varphi_j)}, \tag{140}$$

where $i = \sqrt{-1}$ in this equation, and only this equation. Multiplying the basis functions together yields

$$L^{sph}_{i,j,k}(\rho, \varphi, \theta) = \ell^{\rho}_{i}(\rho)\ell^{\varphi,\theta}_{j,k}(\varphi, \theta). \tag{141}$$

Letting $\mathbf{r}$ be the Cartesian coordinates for (ρ, φ, θ), $L_{i,j,k}(\mathbf{r}) = L_{i,j,k}(\rho, \varphi, \theta)$. Renaming and reindexing $L_{i,j,k}(\mathbf{r})$ as $\phi_j(\mathbf{r})$, we get a set of basis functions that satisfies (88). Then, the interpolation formula for $f(\mathbf{r})$ is

$$f(\mathbf{r}) \approx \sum_{i=1}^{m_\rho} \sum_{j=0}^{2m_\varphi - 1} \sum_{k=0}^{m_\theta} f(\rho_i, \varphi_j, \theta_k) L_{i,j,k}(\rho, \varphi, \theta). \tag{142}$$

This formula is valid unless the Kronecker delta property is needed; there are many terms in the summation that share the same sample point if we consider Cartesian coordinates. Specifically, taking $k = 0$ or m_θ and fixing i in $(\rho_i, \varphi_j, \theta_k)$ determines the sample point regardless of the value j takes. Thus, the basis functions fail to satisfy the Kronecker delta property in Cartesian coordinates. After calculating the weights according to (91) for the $2m_\rho m_\varphi(m_\theta + 1)$ points given in (137), we determine which ones are not unique and add them together; the integral is then calculated with $M = m_\rho(2m_\varphi(m_\theta - 1) + 2)$ distinct points in Cartesian coordinates according to (90). This is equivalent to consolidating all basis functions with $k = 0$ or m_θ and defining a new one for each i by

$$\hat{L}_{i,k}(\rho, \theta) = \sum_{j=0}^{2m_\varphi - 1} L_{i,j,k}(\rho, \varphi, \theta). \tag{143}$$

An example of $\hat{L}_{i,k}(\rho, \theta)$ is given in Fig. 27. With an implied change of coordinates,

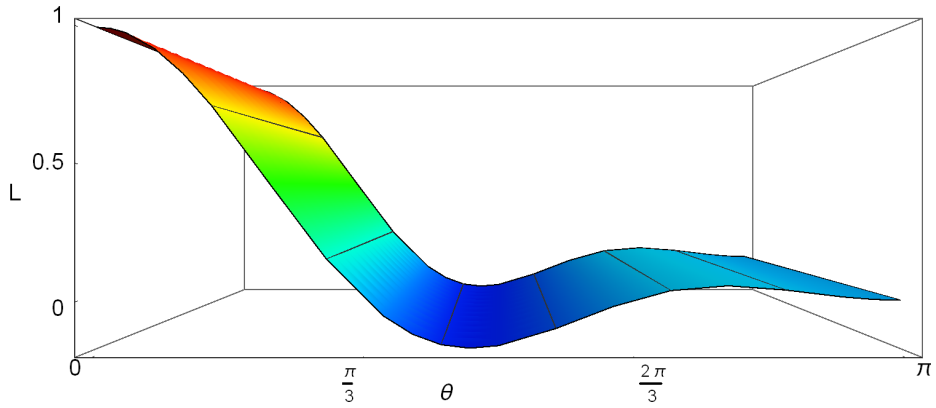

Figure 27: A plot of $\hat{L}_{i,k}(\rho,\theta)$ when $m_\theta = 3$. The Kronecker delta property is satisfied at $\theta = 0, \pi/3, 2\pi/3, \pi$. Note that the function does not depend on the ϕ axes, which goes into the page.

the basis functions in the new interpolation formula

$$f(\mathbf{r}) \approx \sum_{i=1}^{m_\rho} \Bigg(f(\rho_i, \varphi_0, \theta_0)\hat{L}_{i,0}(\rho,\theta) + f(\rho_i, \varphi_0, \theta_{m_\theta})\hat{L}_{i,m_\theta}(\rho,\theta) + \sum_{k=1}^{m_\theta - 1} \sum_{j=0}^{2m_\varphi - 1} f(\rho_i, \varphi_j, \theta_k) L_{i,j,k}(\rho,\varphi,\theta) \Bigg) \tag{144}$$

satisfy the Kronecker delta property in Cartesian coordinates. In practice, we have obtained the same results regardless of whether we consolidate the points or use them with a pseudo-Kronecker delta property.

For interpolation over an ellipsoid, the interpolation points and basis functions defined on the sphere are used with mappings between the sphere and ellipsoid. The mapping from the sphere to the ellipsoid is given by

$$(x, y, z) \mapsto (ax, by, cz) \tag{145}$$

and the mapping from the ellipsoid to the sphere is given by

$$(x, y, z) \mapsto (x/a, y/b, z/c), \tag{146}$$

where a, b, and c are again the semi-axes lengths in the x, y, and z directions. The distribution of interpolation points is similar to the distribution for the sphere, shown in Fig. 26.

3.6 Algorithm Outline

The algorithm for calculating the weights in (91) does not heavily depend on the shape of the domain Ω. Here, we will provide an outline of the algorithm with some notes about what considerations each domain requires. While similar, considerations for the rectangular prism and ellipsoid are not given here.

The input to the algorithm consists of the dimensions of Ω, the location of the singularity $\mathbf{r}'$, the radius δ of the spherical exclusion V_δ, the number m of interpolation points in each direction, the number n of one dimensional brute-force quadrature points in spherical coordinates for the subregion containing the singularity, and the number n_{reg}, n_{cyl}, or n_w of one dimensional brute-force quadrature points for any subregions not containing the singularity. The dimensions and directions are defined in Cartesian, cylindrical, and spherical coordinates for the cuboid, cylindrical, and spherical regions, respectively. Spherical regions do not have any subregions.

If the domain is not spherical, the first step is to determine if subdivisions are necessary given the location of the singularity $\mathbf{r}'$. If they are, the dimensions of each subregion must be calculated. If desired, these subregions can be further subdivided until no region has a single dimension that is significantly larger than any other dimension.

After all required subregions are specified, the brute-force quadrature rule is made.

Points and weights are calculated for subregions not containing the singularity according to formula (100) for the cube and formulas (116) and (117) for the cylinder. For all domains, there is a subregion, perhaps identical to Ω, that contains the singularity. Using spherical coordinates, points and weights are calculated for this subregion according to the formulas (99), (112), and (128) for the cuboid, cylindrical, and spherical regions, respectively. Note that the formula for the cuboid gives the points and weights for only one of the six pyramids that make up the cuboid.

Next, the sample points for interpolation are calculated according to (103), (118), and (137) for the cuboid, cylindrical, and spherical regions, respectively. The basis functions are defined by these interpolation points so there is no need to construct them.

Finally, the desired tensor-product quadrature rule is made by calculating the brute force integrals of the basis functions against the singular kernel, according to (91). The points for the tensor-product quadrature rule are the interpolation points and the weights are the $w_{j,k}$ in (91). For the sphere, the number of sample points and weights can be reduced by combining the weights that correspond to the same points in Cartesian coordinates.

The output from the algorithm is the set of sample points and corresponding weights $w_{j,k}$. When implemented in computer code, these points and weights can be saved to a file for use in the future. Thus, the algorithm needs to only be used once for each set of inputs even if there are many integrals to calculate. If the domain of integration has different dimensions from the one used to calculate the weights $w_{j,k}$, the Jacobian given by (93) can be used to calculate the correct integral at runtime.

3.7 Numerical Results

We use our method to approximate several integrals, subdividing the domain when necessary as in Fig. 22 and Fig. 24. For convenience, let $R = |\mathbf{r} - \mathbf{r}'|$ in this section. In each test we increase the value of M and place the singularity at the interpolation point closest to the boundary to show the most difficult case; as M increases, the singularity will get closer to the boundary. When the denominator contains R^3, even if we reduce the order of the singularity in some way, δ is taken as half of the distance from the singularity to the boundary; otherwise $\delta = 0$. All reference solutions are calculated with our method by performing the brute-force integral with twice as many quadrature points in each direction. While not reported here, we also check our results against Mathematica's NIntegrate function to make sure our method converges to the same value Mathematica's does [1].

There are three tests we perform for when the domain is a cube, cylinder, or sphere; we have obtained good results for when the domain is a rectangular prism or an ellipsoid, but they are not provided here. First, we take $f(\mathbf{r}) = \cos(R)$ in (86) and consider the kernels $1/R$, $1/R^2$, and $1/R^3$. Second, we repeat the test for $\sin(R)$. Since $\sin(R)$ has a cusp at $R = 0$, we take $f(\mathbf{r}) = \sin(R)/R$ and consider the kernels 1, $1/R$, $1/R^2$. While not necessary to get good convergence for $\sin(R)/R^3$, we will take δ to be nonzero to illustrate good convergence for when an exponential function is split into sine and cosine by Euler's formula.

Third, we show a convergence result from a more realistic scenario. Consider a

Green's function defined by the matrix

$$\mathbf{G}(\mathbf{r},\mathbf{r}') = (\mathbf{I} + \frac{1}{k^2}\nabla\nabla)\frac{e^{-ikR}}{4\pi R}, \tag{147}$$

where $\mathbf{I}$ is the identity matrix. This is the Green's function in Chapter 4. Let $\mathbf{u}$ be the unit vector in the direction of $\mathbf{r}-\mathbf{r}'$. Then the hypersingular part of $\mathbf{G}(\mathbf{r},\mathbf{r}')$ has the same behavior as

$$\mathbf{H}(\mathbf{r},\mathbf{r}') = (\mathbf{I} - 3\mathbf{u}\otimes\mathbf{u})\frac{\cos(R)}{R^3}. \tag{148}$$

$\mathbf{H}(\mathbf{r},\mathbf{r}')$ is a symmetric matrix whose entries are defined by

$$\mathbf{H}_{u,v}(\mathbf{r},\mathbf{r}') = \left(\delta_{uv} - 3\frac{(\mathbf{r}_u - \mathbf{r}'_u)(\mathbf{r}_v - \mathbf{r}'_v)}{R^2}\right)\frac{\cos(R)}{R^3}, \tag{149}$$

where $\delta_{u,v}$ is the Kronecker delta and u, v take the values x, y, z. As the second term in the parenthesis depends on the variable of integration, we build on (91) by defining

$$w_j^{u,v} = \sum_{i=1}^{N}\left(\delta_{uv} - 3\frac{(\mathbf{r}_u - \mathbf{r}'_u)(\mathbf{r}_v - \mathbf{r}'_v)}{|\mathbf{r}_i - \mathbf{r}'|^2}\right)\frac{\phi_j(\hat{\mathbf{r}}_i)}{|\hat{\mathbf{r}}_i - \mathbf{r}'|^3}\hat{w}_i. \tag{150}$$

The difference in the weights $w_j^{u,v}$ removes the singularity from the diagonal entries of $\mathbf{H}(\mathbf{r},\mathbf{r}')$ so the integral over any sphere centered at $\mathbf{r}'$ is zero. Since, in a realistic scenario, $\mathbf{H}(\mathbf{r},\mathbf{r}')$ is multiplied by a basis function that destroys any symmetry, we take $\hat{\mathbf{H}}(\mathbf{r},\mathbf{r}') = b(\mathbf{r})\mathbf{H}(\mathbf{r},\mathbf{r}')$, where $b(\mathbf{r}) = (\mathbf{r}_x + 1/2)^2(\mathbf{r}_y + 1/4)^2(\mathbf{r}_z + 1/8)^2 + 1$. Thus, we use an exclusion $V_\delta(\mathbf{r}')$ to get good convergence. Then, we can integrate the entries of $\hat{\mathbf{H}}(\mathbf{r},\mathbf{r}')$ by the interpolation formula

$$\int_{\Omega\setminus V_\delta(\mathbf{r}')}\hat{\mathbf{H}}_{u,v}(\mathbf{r},\mathbf{r}')d\mathbf{r} \approx \sum_{j=1}^{M} b(\mathbf{r}_j)\cos(|\mathbf{r}_j - \mathbf{r}'|)w_j^{u,v}. \tag{151}$$

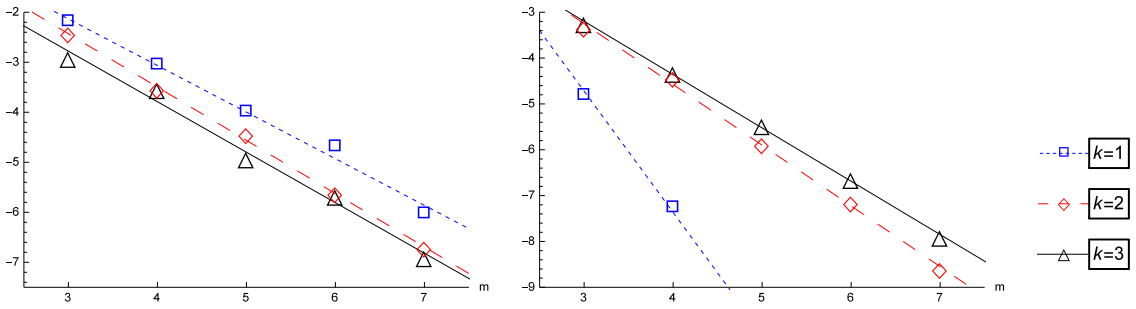

Figure 28: The $\log_{10}$ relative error of the integrals of $\cos(R)/R^k$ (left) and $\sin(R)/R^k$ (right) when Ω is the cube $\Omega = [-1, 1]^3$. $M = m^3$ sample points are used in (90).

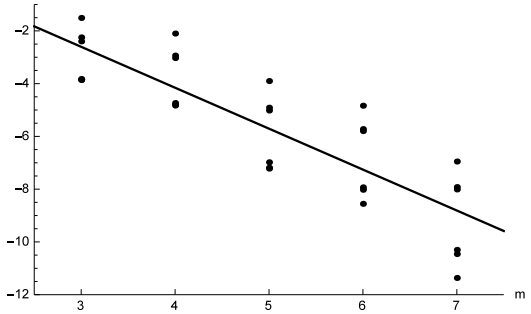

Figure 29: The $\log_{10}$ relative error of the integral of the entries of $\hat{\mathbf{H}}(\mathbf{r}, \mathbf{r}')$ when Ω is the cube $\Omega = [-1/4, 1/4]^3$. Each point corresponds to an entry of $\hat{\mathbf{H}}$ for a given m; the line is a linear fit for all points. $M = m^3$ sample points are used in (90).

3.7.1 Numerical Results for when Ω is a Cube

We take $\Omega = [-1/4, 1/4]^3$ when integrating $\hat{\mathbf{H}}_{u,v}(\mathbf{r}, \mathbf{r}')$, but take $\Omega = [-1, 1]^3$ for $f(\mathbf{r}) = \cos(R)$ or $f(\mathbf{r}) = \sin(R)/R$, for which machine error was quickly reached. Convergence results are given in Fig. 28 for the first two tests and in Fig. 29 for the third test. Our approximations are calculated using $n = n_{reg} = 32$ for all tests except $\cos(R)/R^3$ and $\hat{\mathbf{H}}_{u,v}(\mathbf{r}, \mathbf{r}')$; in these cases, $n = 64$. N is 53,248 and 1,601,536, respectively. The code is given permission to subdivide the nonsingular regions further, which will increase N.

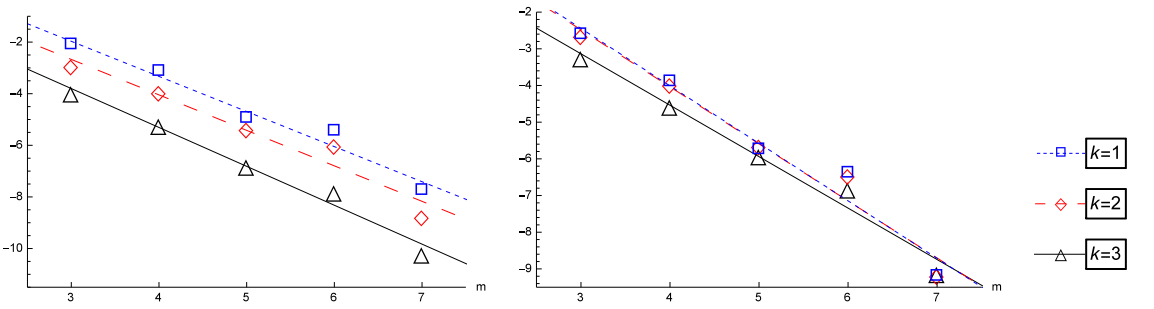

Figure 30: The $\log_{10}$ relative error of the integrals of $\cos(R)/R^k$ (left) and $\sin(R)/R^k$ (right). In the x, y, and z directions, basis functions were of degree $m-1$, m, and m, respectively. Ω is a rectangular prism.

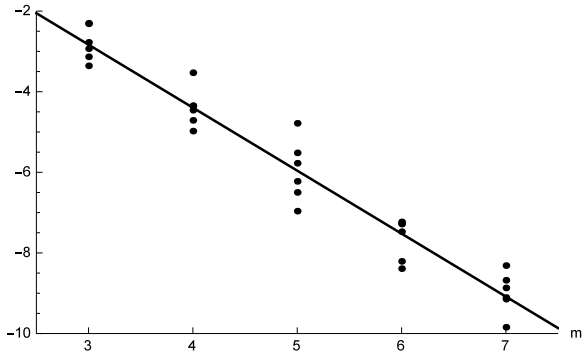

Figure 31: The $\log_{10}$ relative error of the integral of the entries of $\hat{\mathbf{H}}(\mathbf{r},\mathbf{r}')$. In the x, y, and z directions, basis functions were of degree $m-1$, m, and m, respectively. Ω is a rectangular prism.

3.7.2 Numerical Results for when Ω is a Rectangular Prism

Second, we will consider when the domain of integration is a rectangular prism. Let $\Omega = [0, 1.2] \times [0, 1.8] \times [0, 2]$ when $f(\mathbf{r}) = \cos(R)$ or $f(\mathbf{r}) = \sin(R)/R$. When integrating $\hat{\mathbf{H}}_{u,v}(\mathbf{r},\mathbf{r}')$, we divide each dimension of the prism by 4. Convergence results are given in Fig. 30 and Fig. 31, respectively. We took $n = n_{reg} = 16$ for all tests except $\cos(R)/R^3$ and $\hat{\mathbf{H}}_{u,v}(\mathbf{r},\mathbf{r}')$; in these cases, $n = 64$. The code is given permission to subdivide the nonsingular regions further, which increases N significantly; this becomes more necessary the more the cuboid region is deformed.

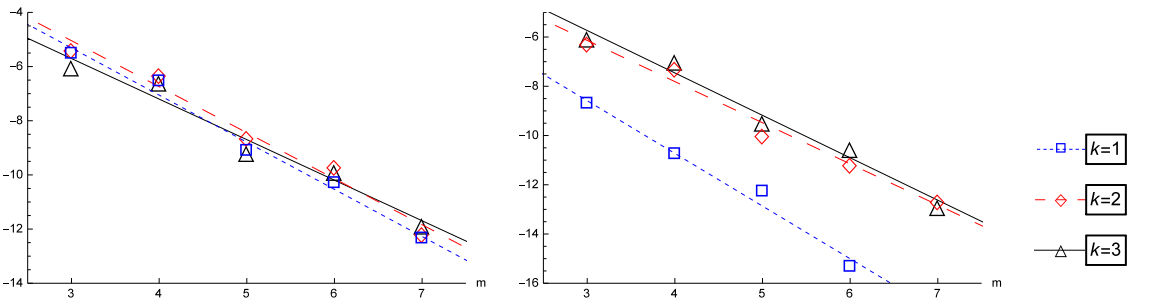

Figure 32: The $\log_{10}$ relative error of the integrals of $\cos(R)/R^k$ (left) and $\sin(R)/R^k$ (right) when Ω is a cylinder. $M = 2m^3$ sample points are used in (90).

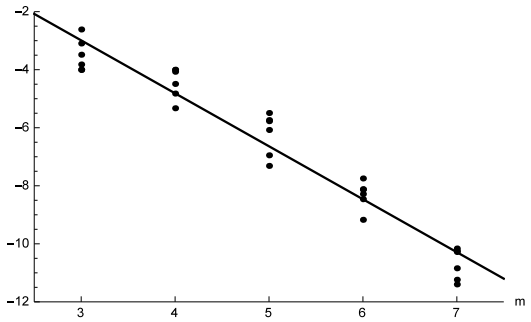

Figure 33: The $\log_{10}$ relative error of the integral of the entries of $\hat{\mathbf{H}}(\mathbf{r}, \mathbf{r}')$ when Ω is a cylinder. Each point corresponds to an entry of $\hat{\mathbf{H}}$ for a given m; the line is a linear fit for all points. $M = 2m^3$ sample points are used in (90).

3.7.3 Numerical Results for when Ω is a Cylinder

Ω is a cylinder of radius 1/4 and height 1/2. Convergence results are given in Fig. 32 for the first two tests and in Fig. 33 for the third test. Our approximations are calculated using $n = n_{cyl} = 16$ and $n_w = 64$ for all tests except $\cos(R)/R^3$ and $\hat{\mathbf{H}}_{u,v}(\mathbf{r}, \mathbf{r}')$; in these cases, $n = 64$. N is 3,166,208 and 3,940,352, respectively. The code is given permission to subdivide the nonsingular regions further, which will increase N.

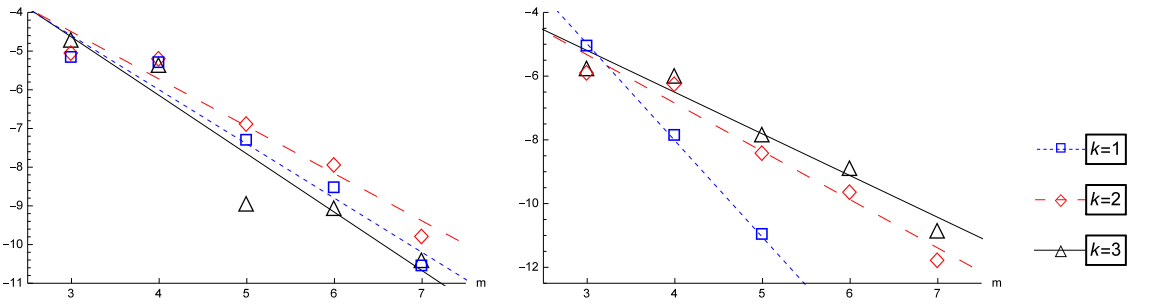

Figure 34: The $\log_{10}$ relative error of the integrals of $\cos(R)/R^k$ (left) and $\sin(R)/R^k$ (right) when Ω is a sphere. $M = m_\rho(2m_\varphi(m_\theta - 1) + 2)$ sample points are used in (90).

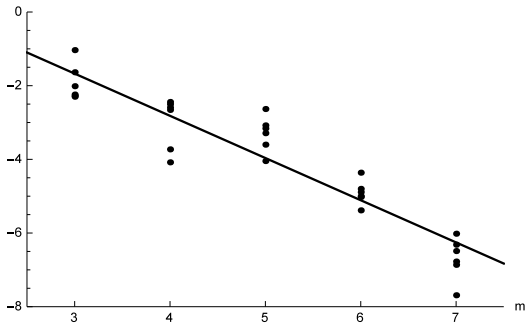

Figure 35: The $\log_{10}$ relative error of the integral of the entries of $\hat{\mathbf{H}}(\mathbf{r}, \mathbf{r}')$ when Ω is a sphere. Each point corresponds to an entry of $\hat{\mathbf{H}}$ for a given m; the line is a linear fit for all points. $M = m_\rho(2m_\varphi(m_\theta - 1) + 2)$ sample points are used in (90).

3.7.4 Numerical Results for when Ω is a Sphere

Ω is a sphere of radius 1 when $f(\mathbf{r}) = \cos(R)$ or $f(\mathbf{r}) = \sin(R)/R$, but Ω is a sphere of radius 1/4 when integrating $\hat{\mathbf{H}}_{u,v}(\mathbf{r}, \mathbf{r}')$. Convergence results are given in Fig. 34 for the first two tests and in Fig. 35 for the third test. Our approximations are calculated using $n = 64$ for all tests. $N = 524,288$. It is not possible to give the code permission to subdivide the sphere.

3.7.5 Numerical Results for when Ω is an Ellipsoid

Fifth, we will consider when the domain of integration is an ellipsoid. Let Ω be an ellipsoid with semi-axes $a = 1/4$, $b = 3/16$, and $c = 1/12$. Convergence results

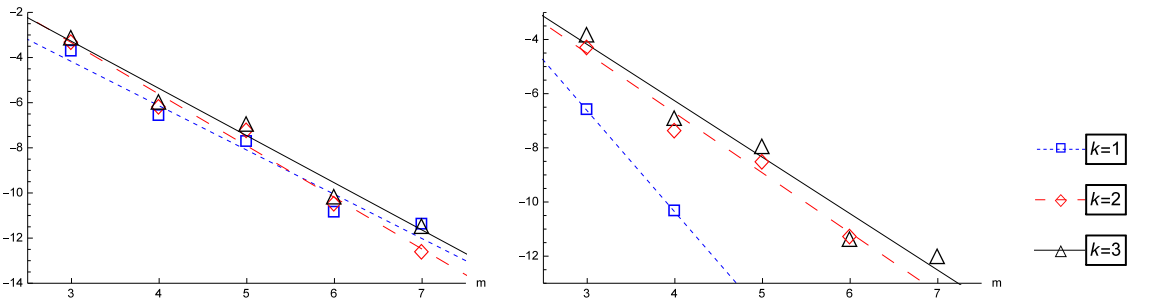

Figure 36: The $\log_{10}$ relative error of the integrals of $\cos(R)/R^k$ (left) and $\sin(R)/R^k$ (right) when Ω is an ellipsoid. $M = m_\rho(2m_\varphi(m_\theta - 1) + 2)$ sample points are used in (90).

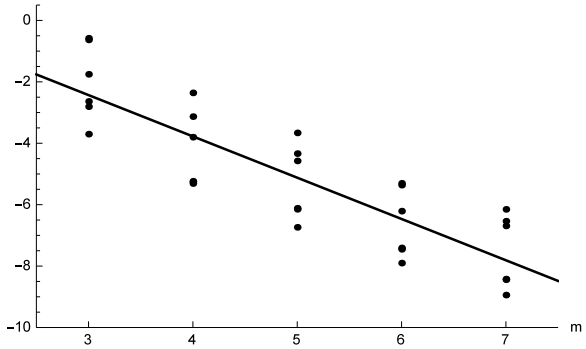

Figure 37: The $\log_{10}$ relative error of the integral of the entries of $\hat{\mathbf{H}}(\mathbf{r}, \mathbf{r}')$ when Ω is an ellipsoid. Each point corresponds to an entry of $\hat{\mathbf{H}}$ for a given m; the line is a linear fit for all points. $M = m_\rho(2m_\varphi(m_\theta - 1) + 2)$ sample points are used in (90).

are given in Fig. 36 for the first two tests and in Fig. 37 for the third test. Our approximations are calculated using $n = 128$ for all tests. $N = 8,388,608$. It is not possible to give the code permission to subdivide the ellipsoid.

3.8 Future Work for Integrating Singularities via Interpolation

Throughout the derivations for this new quadrature method, no integrals were actually calculated over a domain containing a singularity that have not been removed by the Jacobian for spherical coordinates. The singularity was removed by several techniques; we introduced a spherical exclusion V_δ centered at the singularity, we collected the singular kernel with $\sin(R)$ to interpolate $\sin(R)/R$, or we used spherical

coordinates so that the Jacobian would cancel with the singularity. Thus, the final calculation described here can be correctly described as providing accurate results for regular and near-singular integrands. Thus, a natural extension of this work would be to rewrite the formulas for when the singularity is outside the domain Ω, meaning the integral over Ω is near-singular. Since the cube and rectangular prism are useful for h-refinement in VIEs, code has already been written that uses the tensor product of a large number of Gauss points in place of (99) and (100) for the brute-force integration step. However, using this code requires generating more sets of weights than is desirable. Future work will include improving this approach to provide an accurate and efficient way to calculate the near-singular integrals that arise when performing h-refinement.

Implementations for cubes, rectangular prisms, cylinders, spheres, and ellipsoids have been written and produce good convergence results. However, many other geometries are used when solving VIEs. Specifically, tetrahedrons are very common in integral equation code and this method should be adapted to use them. One reason that tetrahedrons are often used is that, similar to cubes, they are easy to subdivide. Assume that there is a subtetrahedron containing a singularity, which uses brute-force integration in spherical coordinates similar to those that the pyramids use in (99), but with different limits of integration. Then the remaining subtetrahedrons do not contain a singularity and the brute-force integration can be handled by a tensor product of Gauss points on the cube $[0, 1]^3$ that are mapped to the standard tetrahedron

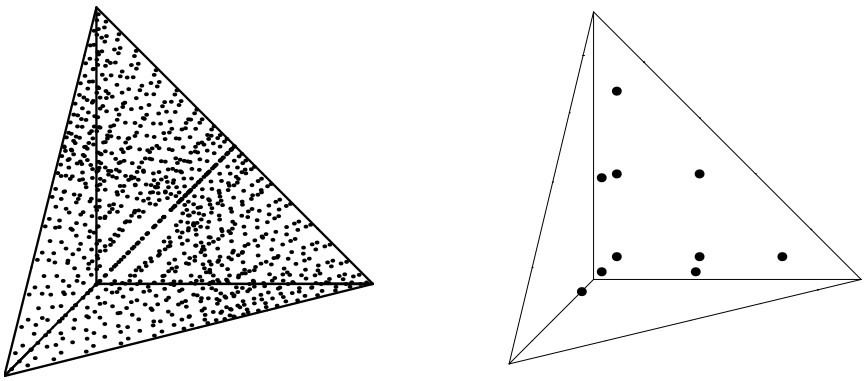

Figure 38: Regular quadrature points (left) and interpolation points (right) on the tetrahedron. While not shown here, the distribution of points in the singular region is similar to Fig. 21.

with vertices at $(0,0,0)$, $(1,0,0)$, $(0,1,0)$, and $(0,0,1)$ by the trilinear mapping

$$(x,y,z) \to \left(x - \frac{xy}{2} - \frac{xz}{2} - \frac{xyz}{3}, y - \frac{xy}{2} - \frac{yz}{2} - \frac{xyz}{3}, z - \frac{xz}{2} - \frac{yz}{2} - \frac{xyz}{3}\right), \quad (152)$$

whose Jacobian is

$$\begin{aligned} &1 - x - y - z + \frac{x^2}{4} + \frac{y^2}{4} + \frac{z^2}{4} + \frac{5xy}{6} + \frac{5xz}{6} + \frac{5yz}{6} \\ &- \frac{x^2y}{6} - \frac{xy^2}{6} - \frac{x^2z}{6} - \frac{xz^2}{6} - \frac{y^2z}{6} - \frac{yz^2}{6} \\ &- \frac{xyz}{2} + \frac{x^2yz}{12} + \frac{xy^2z}{12} + \frac{xyz^2}{12}. \end{aligned} \quad (153)$$

This mapping attempts to minimize the amount of clustering that occurs from mapping points from the cube to the tetrahedron while also providing an easy way to increase the number of sample points to obtain greater accuracy. The resulting set of points has some symmetry, as seen in Fig. 38. Interpolation can be performed as linear, quadratic, cubic, etc. in each direction with a Vandermonde matrix; this approach results in Lagrange polynomials defined over the tetrahedron. The main difficulty lies selecting sample points that lead to good interpolation. Thus far, good

results have been obtained for polynomials that are linear and quadratic in each direction by working with points similar to the ones Keast uses in his quadrature formulas [20]. For integrating $b(\mathbf{r}) * \cos(R)$, where $b(\mathbf{r}) = (\mathbf{r}_x + 1/2)^2(\mathbf{r}_y + 1/4)^2(\mathbf{r}_z + 1/8)^2 + 1$ again, the linear basis functions lead to integration error around 1×10^{-3} and the quadratic basis functions lead to integration error around 4×10^{-4}. Higher order interpolation has not been tested yet and convergence needs to be verified.

One the main difficulties in implementing the quadrature rule in (89) is that the weights have to be precalculated for a specific domain with specific dimensions and value for δ. The domain can then be scaled and the Jacobian is given by (93). However, it is often desirable to use a more complicated elemental mapping than a function that, in terms of the resulting Jacobian, merely scales the size of the domain. There are two issues that must be accounted for: any deformation of the spherical exclusion V_δ and any stretching of $|\mathbf{r} - \mathbf{r}'|$ in a non-uniform way.

In this chapter, we simply stated that the error due to the quadrature rule in (89) is due to two parts: brute-force integration and interpolation. This simple observation is sufficient for using (89) to calculate integrals in Chapter 4. However, more sophisticated error estimates were derived for the one dimensional Newton-Cotes rules in [24][45][42][14][37][41][26][25]. As such, future work includes formulating error estimates that correspond to (89).

Finally, some work on adapting the new quadrature rule defined by (89) to two dimensions was done for the Poisson-Boltzmann models in the previous chapter. While an especially wasteful quadrature rule was used when the implementation proved to be less trivial than expected, we expect that a two dimensional analog of this method

would produce excellent results once properly implemented.

3.9 Summary for Integrating Singular Integrands in Three Dimensions

In this chapter we have proposed a way to generate accurate and efficient tensor-product quadrature formula for hypersingular functions over cubes, rectangles, spheres, ellipsoids, and cylinders. The quadrature rule is derived from direct brute-force quadratures through an interpolation technique for the smooth part of the integrand. The resulting tensor product quadrature, which can be pre-computed and tabulated, can reproduce the brute-force quadrature results with only a small number of samples of the integrand.

CHAPTER 4: SOLAR CELLS

4.1 The Vector Wave Equation and its Corresponding Integral Equation

Maxwell's equation are the foundation of classical electromagnetism. With them, we will derive a vector wave equation with a corresponding integral representation. The integral equation will be used to solve for the electric field via a Nyström volume integral equation method. This chapter will closely follow [9].

4.1.1 Maxwell Equations

We begin with the time-harmonic Maxwell equations as given in [6]. Let $\mathbf{E}$ be the electric field, $\mathbf{D}$ be the electric displacement flux, $\mathbf{B}$ be the magnetic flux density, $\mathbf{H}$ be the derived magnetic field, $\mathbf{J}_m$ be the magnetic current, $\mathbf{J}_e$ be the steady free charge current density, ρ_e be the electric charge, $\rho_m(\equiv 0)$ be the magnetic charge, ϵ be the permittivity, and μ be the permeability. Then the time-harmonic Maxwell equations in materials are

$$\nabla \times \mathbf{E} = -\mathrm{i}\omega\mu\mathbf{H} - \mathbf{J}_m, \tag{154}$$

$$\nabla \times \mathbf{H} = \mathrm{i}\omega\epsilon\mathbf{E} + \mathbf{J}_e, \tag{155}$$

$$\nabla \cdot \mathbf{D} = \rho_e, \tag{156}$$

$$\nabla \cdot \mathbf{B} = \rho_m. \tag{157}$$

Since the equations are for time-harmonic fields, the time dependence is contained in $\exp(\mathrm{i}\omega t)$ and factored out. For two materials with different constants (ϵ_1, μ_1) and (ϵ_2, μ_2) with an interface σ, the corresponding boundary conditions are

$$[\mathbf{n} \times \mathbf{H}] = \mathbf{n} \times (\mathbf{H}_2 - \mathbf{H}_1) = \mathbf{J}_{e(\sigma)}, \tag{158}$$

$$[\mathbf{n} \times \mathbf{E}] = \mathbf{n} \times (\mathbf{E}_2 - \mathbf{E}_1) = -\mathbf{J}_{m(\sigma)}, \tag{159}$$

$$[\mathbf{n} \cdot \mathbf{B}] = \mathbf{n} \cdot (\mu_2 \mathbf{H}_2 - \mu_1 \mathbf{H}_1) = \rho_{m(\sigma)}, \tag{160}$$

$$[\mathbf{n} \cdot \mathbf{D}] = \mathbf{n} \cdot (\epsilon_2 \mathbf{E}_2 - \epsilon_1 \mathbf{E}_1) = \rho_{e(\sigma)}, \tag{161}$$

where $\mathbf{n}$ is a normal vector pointing into material 2, $[\cdot]$ is the jump across σ, and the subscripts 1, 2, and σ denote the location the quantity is defined.

The vector wave equations follow from the Maxwell equations. Dividing (154) by μ and applying $\nabla\times$, we get

$$\nabla \times \frac{1}{\mu} \nabla \times \mathbf{E} = -\mathrm{i}\omega \nabla \times \mathbf{H} - \nabla \times \frac{1}{\mu} \mathbf{J}_m. \tag{162}$$

Using (155) to substitute replace $\mathbf{H}$ with $\mathbf{E}$,

$$\nabla \times \frac{1}{\mu} \nabla \times \mathbf{E} - \omega^2 \epsilon \mathbf{E} = -\mathrm{i}\omega \mathbf{J}_e - \nabla \times \frac{1}{\mu} \mathbf{J}_m \tag{163}$$

is the vector wave equation for $\mathbf{E}$. Let Ω be the set of inhomogeneities, $\partial\Omega$ the boundary of Ω, Σ the set of boundaries between layers as in Fig. 39, $\mathcal{L} = \nabla \times \frac{1}{\mu} \nabla\times$, and $\mathbf{J}_m = 0$. Then the vector wave equation is given by

$$\mathcal{L}\mathbf{E}(\mathbf{r}) - \omega^2 \epsilon(\mathbf{r}) \mathbf{E}(\mathbf{r}) = -\mathrm{i}\omega \mathbf{J}_e(\mathbf{r}), \quad \mathbf{r} \in \mathbb{R}^3 \backslash (\Sigma \cup \partial\Omega), \tag{164}$$

where $\mathbf{J}_e(\mathbf{r})$ is due to a source far away and above the layered region. The incident

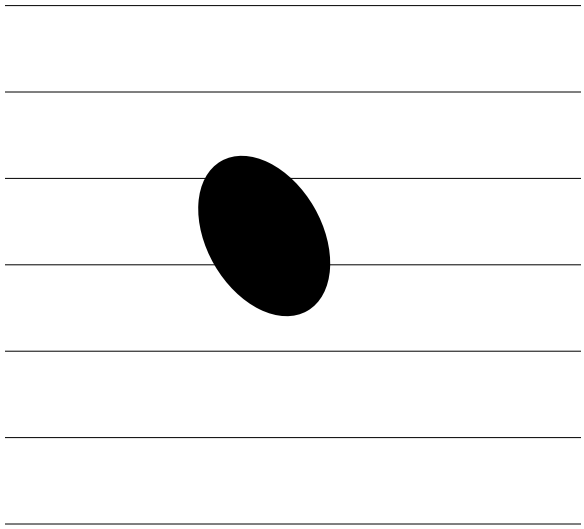

Figure 39: A scatterer Ω in a layered medium, whose boundaries make up Σ.

wave is

$$\mathbf{E}^{\text{inc}}(\mathbf{r}) = -\mathrm{i}\omega\mu(\mathbf{r}) \int_{\mathbb{R}^3} \overline{\mathbf{G}}_E(\mathbf{r}, \mathbf{r}') \cdot \mathbf{J}_e(\mathbf{r}')\mathrm{d}\mathbf{r}', \tag{165}$$

where $\overline{\mathbf{G}}_E(\mathbf{r}, \mathbf{r}')$ is the Green's function given by

$$\mathcal{L}\overline{\mathbf{G}}_E(\mathbf{r}, \mathbf{r}') - \omega^2\epsilon_L(\mathbf{r})\overline{\mathbf{G}}_E(\mathbf{r}, \mathbf{r}') = \frac{1}{\mu(\mathbf{r})}\bar{\mathbf{I}}\delta(\mathbf{r} - \mathbf{r}'), \ \mathbf{r} \in \mathbb{R}^3. \tag{166}$$

Specifically for a homogeneous medium,

$$\begin{aligned} &\overline{\mathbf{G}}_{\mathbf{E}}(\mathbf{r}, \mathbf{r}') = \overline{\mathbf{G}}_{\mathbf{E}}(\mathbf{r}', \mathbf{r}) = \left(\bar{\mathbf{I}} + \frac{1}{k^2}\nabla\nabla\right) g(\mathbf{r}, \mathbf{r}') \\ &= \frac{e^{-ikR}}{4\pi R}(\mathbf{I} - \mathbf{u} \otimes \mathbf{u}) - \frac{ie^{-ikR}}{4\pi R^2 k}(\mathbf{I} - 3\mathbf{u} \otimes \mathbf{u}) - \frac{e^{-ikR}}{4\pi R^3 k^2}(\mathbf{I} - 3\mathbf{u} \otimes \mathbf{u}), \end{aligned} \tag{167}$$

where $k^2 = \omega^2\epsilon_i\mu_i$, $\epsilon_i = \epsilon_L(\mathbf{r})$, $\mathbf{u} = (\mathbf{r} - \mathbf{r}')/R$, $\otimes$ the outer product for vectors, and

$$g(\mathbf{r}, \mathbf{r}') = \frac{1}{4\pi}\frac{\mathrm{e}^{-\mathrm{i}kR}}{R}, \qquad R = |\mathbf{r} - \mathbf{r}'|. \tag{168}$$

The inhomogeneities Ω have a different dielectric constant ε than the surrounding medium. Let $\epsilon(\mathbf{r}) = \epsilon_L(\mathbf{r}) + \Delta\epsilon(\mathbf{r})$, $\Delta\epsilon(\mathbf{r}) = 0, \mathbf{r} \notin \Omega$. Next, the equivalent current

source accounts for the inhomogeneity by $\mathbf{J}_{\text{eq}}(\mathbf{r}) = \mathrm{i}\omega\Delta\epsilon(\mathbf{r})\mathbf{E}(\mathbf{r})$ so that the vector wave equation can be written as

$$\mathcal{L}\mathbf{E}(\mathbf{r}) - \omega^2\epsilon_L(\mathbf{r})\mathbf{E}(\mathbf{r}) = -\mathrm{i}\omega\mathbf{J}(\mathbf{r}), \tag{169}$$

where $\mathbf{J}(\mathbf{r}) = \mathbf{J}_e(\mathbf{r}) + \mathbf{J}_{\text{eq}}(\mathbf{r})$.

4.1.2 Integral Equation Derivation

Let $\mathbf{r}' \in \Omega$, and let $V_\delta = V_\delta(\mathbf{r}') \subset \Omega$ be a small sphere centered at $\mathbf{r}'$ to eventually exclude. Following [38], we proceed by considering each coordinate separately. Let $\mathbf{e}$ be any of the Cartesian basis vectors. Then we multiply (169) by $\overline{\mathbf{G}}^1_E(\mathbf{r},\mathbf{r}')\cdot\mathbf{e}$ to get

$$\mathcal{L}\mathbf{E}_1(\mathbf{r})\cdot\overline{\mathbf{G}}^1_E(\mathbf{r},\mathbf{r}')\cdot\mathbf{e} - \omega^2\epsilon\mathbf{E}_1(\mathbf{r})\cdot\overline{\mathbf{G}}^1_E(\mathbf{r},\mathbf{r}')\cdot\mathbf{e} = -\mathrm{i}\omega\mathbf{J}_e(\mathbf{r})\cdot\overline{\mathbf{G}}^1_E(\mathbf{r},\mathbf{r}')\cdot\mathbf{e}. \tag{170}$$

We get a second equation by multiplying (166) by $\mathbf{E}_1$ on the left and by $\mathbf{e}$ on the right to get

$$\mathbf{E}_1(\mathbf{r})\cdot\mathcal{L}\overline{\mathbf{G}}^1_E(\mathbf{r},\mathbf{r}')\cdot\mathbf{e} - \omega^2\epsilon\mathbf{E}_1(\mathbf{r})\cdot\overline{\mathbf{G}}^1_E(\mathbf{r},\mathbf{r}')\cdot\mathbf{e} = \frac{1}{\mu(\mathbf{r}')}\mathbf{E}_1(\mathbf{r})\cdot\mathbf{e}\delta(\mathbf{r}-\mathbf{r}'). \tag{171}$$

Taking the difference of these two equations, we get

$$\begin{aligned}&\mathcal{L}\mathbf{E}_1(\mathbf{r})\cdot\overline{\mathbf{G}}^1_E(\mathbf{r},\mathbf{r}')\cdot\mathbf{e} - \mathbf{E}_1(\mathbf{r})\cdot\mathcal{L}\overline{\mathbf{G}}^1_E(\mathbf{r},\mathbf{r}')\cdot\mathbf{e}\\ &= -\mathrm{i}\omega\mathbf{J}_e(\mathbf{r})\cdot\overline{\mathbf{G}}^1_E(\mathbf{r},\mathbf{r}')\cdot\mathbf{e} - \frac{1}{\mu}\mathbf{E}_1(\mathbf{r})\cdot\mathbf{e}\delta(\mathbf{r}-\mathbf{r}').\end{aligned} \tag{172}$$

Taking the integral over $\mathbb{R}^3\backslash V_\delta$ gives

$$\begin{aligned}\int_{\mathbb{R}^3\backslash V_\delta} \mathrm{d}\mathbf{r} \Big[& \mathcal{L}\mathbf{E}_1(\mathbf{r}) \cdot \overline{\mathbf{G}}^1_E(\mathbf{r},\mathbf{r}') \cdot \mathbf{e} \\ & - \mathbf{E}_1(\mathbf{r}) \cdot \mathcal{L}\overline{\mathbf{G}}^1_E(\mathbf{r},\mathbf{r}') \cdot \mathbf{e} \Big] \\ = & -\mathrm{i}\omega \int_{\mathbb{R}^3\backslash V_\delta} \mathrm{d}\mathbf{r} \left[\mathbf{J}_e(\mathbf{r}) \cdot \overline{\mathbf{G}}^1_E(\mathbf{r},\mathbf{r}') \cdot \mathbf{e} \right]. \end{aligned} \tag{173}$$

For the derivative operator $\mathcal{L}$, we have the identity

$$(\mathcal{L}\mathbf{f}) \cdot \mathbf{g} - \mathbf{f} \cdot (\mathcal{L}\mathbf{g}) = \nabla \cdot \frac{1}{\mu}[\,(\nabla \times \mathbf{f}) \times \mathbf{g} + \mathbf{f} \times (\nabla \times \mathbf{g})]. \tag{174}$$

(173) becomes

$$\begin{aligned}&\int_{\mathbb{R}^3\backslash V_\delta} \mathrm{d}\mathbf{r}\ \nabla \cdot \frac{1}{\mu} \left[(\nabla \times \mathbf{E}_1(\mathbf{r})) \times \overline{\mathbf{G}}^1_E(\mathbf{r},\mathbf{r}') \cdot \mathbf{e} + \mathbf{E}_1(\mathbf{r}) \times \left(\nabla \times \overline{\mathbf{G}}^1_E(\mathbf{r},\mathbf{r}') \cdot \mathbf{e} \right) \right] \\ &= -\mathrm{i}\omega \int_{\mathbb{R}^3\backslash V_\delta} \mathrm{d}\mathbf{r}\ \mathbf{J}_e(\mathbf{r}) \cdot \overline{\mathbf{G}}^1_E(\mathbf{r},\mathbf{r}') \cdot \mathbf{e}. \end{aligned} \tag{175}$$

By Gauss's divergence theorem, we get

$$\begin{aligned} - \int_{\partial S \cup \Sigma} \mathrm{d}s\ \mathbf{n} \cdot \frac{1}{\mu(\mathbf{r})} \Big[& (\nabla \times \mathbf{E}_1(\mathbf{r})) \times \overline{\mathbf{G}}^1_E(\mathbf{r},\mathbf{r}') \cdot \mathbf{e} \\ & + \mathbf{E}_1(\mathbf{r}) \times \left(\nabla \times \overline{\mathbf{G}}^1_E(\mathbf{r},\mathbf{r}') \cdot \mathbf{e} \right) \Big] \\ = & -\mathrm{i}\omega \int_{\mathbb{R}^3\backslash V_\delta} \mathrm{d}\mathbf{r} \left[\mathbf{J}_e(\mathbf{r}) \cdot \overline{\mathbf{G}}^1_E(\mathbf{r},\mathbf{r}') \cdot \mathbf{e} \right], \end{aligned} \tag{176}$$

where $S_\delta = \partial V_\delta(\mathbf{r})$ and the normal $\mathbf{n}$ on S_δ is pointing out of $V_\delta(\mathbf{r})$. Taking $\mathbf{n}$ on Σ to be pointing in the same direction, the integrals over Σ will cancel due to the

boundary conditions that require tangential components to be continuous:

$$[\mathbf{n}\times(\mathbf{g}\times\mathbf{n})]_{\Sigma_i}=\mathbf{0},\ [\mathbf{n}\times(\mathbf{h}\times\mathbf{n})]_{\Sigma_i}=\mathbf{0},$$

$$\mathbf{n}\times[\mathbf{E}_1(\mathbf{r})]_{\Sigma_i}=\mathbf{0},\quad \mathbf{n}\times[\mathbf{H}_1(\mathbf{r})]_{\Sigma_i}=\mathbf{0}. \tag{177}$$

Switching $\mathbf{r}$ and $\mathbf{r}'$, we have

$$-\mathrm{i}\omega\mu(\mathbf{r})\int_{\mathbb{R}^3\setminus V_\delta}\mathrm{d}\mathbf{r}'\ \overline{\mathbf{G}}_E(\mathbf{r},\mathbf{r}')\cdot\mathbf{J}(\mathbf{r}')-\mu(\mathbf{r})\int_{S_\delta}\mathrm{d}s'\left[\mathrm{i}\omega\ \overline{\mathbf{G}}_E(\mathbf{r},\mathbf{r}')\cdot(\mathbf{n}\times\mathbf{H}(\mathbf{r}'))\right.$$
$$\left.-\ \frac{1}{\mu(\mathbf{r}')}\nabla\times\overline{\mathbf{G}}_E(\mathbf{r},\mathbf{r}')\cdot(\mathbf{n}\times\mathbf{E}(\mathbf{r}'))\right]=\mathbf{0},\qquad \mathbf{r}\in\Omega. \tag{178}$$

If $\delta\to 0$, the CPV is obtained. Since the inhomogeneities are handled by the dielectric constant, we will disregard the layers Σ and assume the Green's function everywhere is for a homogeneous medium. Future work will include introducing layers. Note that in the limit of $\delta\to 0$, it is valid to assume the Green's function on S_δ is well approximated by the Green's function for a homogeneous medium. The integral over S_δ can be estimated when δ is small since $kR\ll 1$ leads to

$$\overline{\mathbf{G}}_{\mathbf{E}}(\mathbf{r},\mathbf{r}')=\frac{1}{4\pi k^2R^3}(\mathbf{I}-3\mathbf{u}_R\mathbf{u}_R)+O\left(\frac{1}{R^2}\right), \tag{179}$$

$$\nabla'\times\overline{\mathbf{G}}_{\mathbf{E}}(\mathbf{r},\mathbf{r}')=\frac{1}{4\pi R^2}\mathbf{u}_R\times\mathbf{I}+O\left(\frac{1}{R}\right), \tag{180}$$

where $\mathbf{u}_R=(\mathbf{r}'-\mathbf{r})/R$. This implies that [12][39]:

$$\lim_{\delta\to 0}\int_{S_\delta}\mathrm{d}s'\ \mathbf{n}\times\mathbf{E}(\mathbf{r}')\cdot\nabla\times\overline{\mathbf{G}}_E(\mathbf{r}',\mathbf{r})=-\left[\mathbf{I}-\mathbf{L}_{V_\delta}\right]\cdot\mathbf{E}(\mathbf{r}), \tag{181}$$

$$\lim_{\delta\to 0}\int_{S_\delta}\mathrm{d}s'\ \mathbf{n}\times\mathbf{H}(\mathbf{r}')\cdot\overline{\mathbf{G}}_E(\mathbf{r}',\mathbf{r})=-\frac{1}{k^2}\mathbf{L}_{V_\delta}\cdot\nabla\times\mathbf{H}(\mathbf{r}), \tag{182}$$

and the **L**-dyadic for when V_δ is a sphere is given by [44]:

$$\mathbf{L}_{V_\delta} = \frac{1}{3}\mathbf{I}. \tag{183}$$

Returning to our integral equation, after evaluating the limit as $\delta \to 0$, we now have

$$\begin{aligned}\mathbf{0} = \mathbf{E}^{\text{inc}}(\mathbf{r}) - \mathrm{i}\omega\mu(\mathbf{r})\text{p.v.}\int_{\mathbb{R}^3} \mathrm{d}\mathbf{r}'\mathbf{J}_{eq}(\mathbf{r}')\cdot\overline{\mathbf{G}}_E(\mathbf{r}',\mathbf{r}) \\ +\ \mathbf{L}_{\mathbf{V}_\delta}\cdot\left[\mathrm{i}\omega\mu(\mathbf{r})\frac{1}{k^2}\nabla\times\mathbf{H}(\mathbf{r}')+\mathbf{E}(\mathbf{r})\right] - \mathbf{E}(\mathbf{r}), \quad \mathbf{r}\in\Omega.\end{aligned} \tag{184}$$

Applying Ampère's law (155) yields

$$\begin{aligned}\mathbf{0} = \ \mathbf{E}^{\text{inc}}(\mathbf{r}) - \mathrm{i}\omega\mu(\mathbf{r})\text{p.v.}\int_{\mathbb{R}^3} \mathrm{d}\mathbf{r}'\ \mathbf{J}_{eq}(\mathbf{r}')\cdot\overline{\mathbf{G}}_E(\mathbf{r}',\mathbf{r}) \\ +\ \mathbf{L}_{\mathbf{V}_\delta}\cdot\left(\frac{\mathrm{i}}{\omega}\mathbf{J}\right) - \mathbf{E}(\mathbf{r}), \quad \mathbf{r}\in\Omega.\end{aligned} \tag{185}$$

Since $\mathbf{J}(\mathbf{r}) = \mathbf{J}_{\text{eq}}(\mathbf{r}) = \mathrm{i}\omega\Delta\epsilon(\mathbf{r})\mathbf{E}(\mathbf{r})$ inside Ω, the VIE for $\mathbf{r}\in\Omega$ is given by

$$\mathbf{C}\cdot\mathbf{E}(\mathbf{r}) = \mathbf{E}^{\text{inc}}(\mathbf{r}) - \mathrm{i}\omega\mu(\mathbf{r})\ \text{p.v.}\int_\Omega \mathrm{d}\mathbf{r}'\ \mathrm{i}\omega\Delta\epsilon(\mathbf{r}')\mathbf{E}(\mathbf{r}')\cdot\overline{\mathbf{G}}_E(\mathbf{r}',\mathbf{r}), \tag{186}$$

where

$$\mathbf{C} = \mathbf{I} + \mathbf{L}_{V_\delta}\cdot\Delta\epsilon(\mathbf{r}). \tag{187}$$

However, the Cauchy principle value is difficult to evaluate in practice and it is desirable to exclude the spherical region V_δ. This can be accomplished through use of the Helmholtz decomposition.

4.2 Derivation of the Integral Equation Based on the Helmholtz Decomposition

While (186) can be used with a fixed δ in a VIE method, it is desirable to know how the choice of δ will affect our approximation to $\mathbf{E}$. In this section, we will rederive (186) with the role of δ made explicit.

4.2.1 The Helmholtz Decomposition and the Helmholtz Equation

The Helmholtz vector decomposition is given verbatim as follows in [6]. For a differentiable vector field $\mathbf{W}(\mathbf{r}) = (W_1(\mathbf{r}), W_2(\mathbf{r}), W_3(\mathbf{r}))^{\mathrm{T}}$, $\mathbf{r} \in \Omega \subset \mathbb{R}^3$, where Ω is simply connected with a Lipschitz-continuous boundary, there exists a unique vector potential $\mathbf{\Phi}(\mathbf{r})$ and a scalar potential $q(\mathbf{r})$ (unique up to a constant) such that the following orthogonal decomposition holds:

$$\mathbf{W} = \mathbf{W}_1 + \mathbf{W}_2 \equiv \nabla \times \mathbf{\Phi} + \nabla q, \tag{188}$$

where $\mathbf{W}_1 = \nabla \times \mathbf{\Phi}$ is the solenoid field with zero divergence and $\mathbf{W}_2 = \nabla q$ is the irrotational field with zero vorticity, and $\mathbf{\Phi}(\mathbf{r})$ and $q(\mathbf{r})$ satisfy the following elliptic systems with corresponding boundary conditions:

$$-\nabla^2 \mathbf{\Phi} = \nabla \times \mathbf{W}, \qquad \nabla \cdot \mathbf{\Phi} = 0, \tag{189}$$

$$\mathbf{n} \times \mathbf{\Phi} = \mathbf{0} \quad \text{on} \quad \partial\Omega, \tag{190}$$

and

$$\nabla^2 q = \nabla \cdot \mathbf{W}, \tag{191}$$

$$\nabla q \cdot \mathbf{n} = \mathbf{W} \cdot \mathbf{n} \quad \text{on} \quad \partial\Omega. \tag{192}$$

Assuming $\mathbf{J}_m = 0$ and $\rho_m = 0$, (157) gives

$$\nabla \cdot \mathbf{B} = 0. \tag{193}$$

Then, by the Homholtz decomposition provides for the existence of a vector potential $\mathbf{A}$ where

$$\mathbf{B} = \nabla \times \mathbf{A}. \tag{194}$$

Inserting (194) into (154),

$$\nabla \times (\mathbf{E} + \mathrm{i}\omega\mathbf{A}) = \mathbf{0}. \tag{195}$$

The Helmholtz decomposition for $\mathbf{E} + \mathrm{i}\omega\mathbf{A}$ provides for the existence of a scalar function V_e, where $\mathbf{E} + \mathrm{i}\omega\mathbf{A} = -\nabla V_e$ so that

$$\mathbf{E} = -\mathrm{i}\omega\mathbf{A} - \nabla V_e. \tag{196}$$

Putting this expression into the vector wave equation (163) for $\mathbf{E}$,

$$\mathcal{L}\mathbf{A} - \omega^2\epsilon\mathbf{A} + \mathrm{i}\omega\epsilon\nabla V_e = \mathbf{J}_e. \tag{197}$$

The vector identities

$$\nabla \times c\mathbf{f} = \nabla c \times \mathbf{f} + c\nabla \times \mathbf{f} \tag{198}$$

and

$$\nabla \times \nabla \times \mathbf{A} = -\nabla^2\mathbf{A} + \nabla(\nabla \cdot \mathbf{A}) \tag{199}$$

can be used to manipulate the vector wave equation (197) to get

$$-\nabla^2\mathbf{A} - k^2\mathbf{A} + \nabla(\nabla \cdot \mathbf{A}) + \mathrm{i}\omega\epsilon\mu\nabla V_e + \mu\left(\nabla\frac{1}{\mu}\right) \times \nabla \times \mathbf{A} = \mu\mathbf{J}_e. \tag{200}$$

Using the Lorentz gauge $\nabla \cdot \mathbf{A} = -\mathrm{i}\omega\epsilon\mu V_e$ and following [36], we have

$$\nabla^2\mathbf{A} + k^2\mathbf{A} - \mu\left(\nabla\frac{1}{\mu}\right) \times \nabla \times \mathbf{A} = -\mu\mathbf{J}_e. \tag{201}$$

Since we will take μ to be constant, we arrive at the usual Helmholtz equation for the components of $\mathbf{A}$:

$$\nabla^2\mathbf{A} + k^2\mathbf{A} = -\mu\mathbf{J}_e. \tag{202}$$

A similar derivation gives

$$\nabla^2\mathbf{A} + k^2\mathbf{A} = -\mu\mathbf{J}, \tag{203}$$

where $\mathbf{J}$ is again given by $\mathbf{J}(\mathbf{r}) = \mathbf{J}_e(\mathbf{r}) + \mathbf{J}_{\mathrm{eq}}(\mathbf{r})$.

4.2.2 Integral Equation Derivation

From the theory of Green's functions, an integral representation solution to (203) is

$$\mathbf{A} = \mu\int_{\mathbb{R}^3} \mathrm{d}\mathbf{r}'\mathbf{J}(\mathbf{r}')g(\mathbf{r},\mathbf{r}'). \tag{204}$$

Let $V_\delta \subset \Omega$ be a sphere of radius δ centered at $\mathbf{r}$. Since $\mathrm{supp}(\mathbf{J}_e(\mathbf{r})) \cap \Omega = \emptyset$ and $\mathbf{J}_{\mathrm{eq}}(\mathbf{r}) = \mathrm{i}\omega\Delta\epsilon(\mathbf{r})\mathbf{E}(\mathbf{r})$,

$$\begin{aligned}
\mathbf{A} &= \mu\int_{\mathbb{R}^3\setminus\Omega} \mathbf{J}_e(\mathbf{r}')g(\mathbf{r},\mathbf{r}')\mathrm{d}\mathbf{r}' + \mu\int_{\Omega} \mathbf{J}_{\mathrm{eq}}(\mathbf{r}')g(\mathbf{r},\mathbf{r}')\mathrm{d}\mathbf{r}' \\
&= \mu\int_{\mathbb{R}^3\setminus\Omega} \mathbf{J}_e(\mathbf{r}')g(\mathbf{r},\mathbf{r}')\mathrm{d}\mathbf{r}' + \mu\int_{\Omega} \mathrm{i}\omega\Delta\epsilon(\mathbf{r}')\mathbf{E}(\mathbf{r}')g(\mathbf{r},\mathbf{r}')\mathrm{d}\mathbf{r}' \\
&= \mu\int_{\mathbb{R}^3\setminus\Omega} \mathbf{J}_e(\mathbf{r}')g(\mathbf{r},\mathbf{r}')\mathrm{d}\mathbf{r}' + \mu\left(\int_{\Omega\setminus V_\delta} + \int_{V_\delta}\right) \mathrm{i}\omega\Delta\epsilon(\mathbf{r}')\mathbf{E}(\mathbf{r}')g(\mathbf{r},\mathbf{r}')\mathrm{d}\mathbf{r}'.
\end{aligned} \tag{205}$$

Since $\mathbf{r} \in V_\delta$, only the last integral will contain a singularity. Returning to the Helmholz decomposition for $\mathbf{E}$ given by (196), the Lorentz gauge condition $\nabla \cdot \mathbf{A} =$

$-\mathrm{i}\omega\epsilon\mu V$ gives [36]

$$\mathbf{E} = -\mathrm{i}\omega\mathbf{A} + \frac{1}{\mathrm{i}\omega\epsilon\mu}\nabla(\nabla\cdot\mathbf{A}) = -\mathrm{i}\omega\left[\bar{\mathbf{I}} + \frac{1}{k^2}\nabla\nabla\right]\mathbf{A}. \tag{206}$$

Inserting the integral representation for $\mathbf{A}$, we have

$$\begin{aligned}\mathbf{E} =& -\mathrm{i}\omega\left[\bar{\mathbf{I}} + \frac{1}{k^2}\nabla\nabla\right]\left[\mu\int_{\mathbb{R}^3\setminus\Omega}\mathbf{J}_e(\mathbf{r}')g(\mathbf{r},\mathbf{r}')\mathrm{d}\mathbf{r}'\right.\\ &\left.+\mu\left(\int_{\Omega\setminus V_\delta}+\int_{V_\delta}\right)\mathrm{i}\omega\Delta\epsilon(\mathbf{r}')\mathbf{E}(\mathbf{r}')g(\mathbf{r},\mathbf{r}')\mathrm{d}\mathbf{r}'\right]\\ =& -\mathrm{i}\omega\mu\int_{\mathbb{R}^3\setminus\Omega}\mathbf{J}_e(\mathbf{r}')\left[\bar{\mathbf{I}} + \frac{1}{k^2}\nabla\nabla\right]g(\mathbf{r},\mathbf{r}')\mathrm{d}\mathbf{r}'\\ &-\mathrm{i}\omega\mu\int_{\Omega\setminus V_\delta}\mathrm{i}\omega\Delta\epsilon(\mathbf{r}')\mathbf{E}(\mathbf{r}')\left[\bar{\mathbf{I}} + \frac{1}{k^2}\nabla\nabla\right]g(\mathbf{r},\mathbf{r}')\mathrm{d}\mathbf{r}'\\ &-\mathrm{i}\omega\mu\left[\bar{\mathbf{I}} + \frac{1}{k^2}\nabla\nabla\right]\int_{V_\delta}\mathrm{i}\omega\Delta\epsilon(\mathbf{r}')\mathbf{E}(\mathbf{r}')g(\mathbf{r},\mathbf{r}')\mathrm{d}\mathbf{r}'\end{aligned} \tag{207}$$

Using $\overline{\mathbf{G}}_{\mathbf{E}}(\mathbf{r},\mathbf{r}') = \left(\bar{\mathbf{I}} + \frac{1}{k^2}\nabla\nabla\right)g(\mathbf{r},\mathbf{r}')$ and $\mathbf{E}^{\mathrm{inc}}(\mathbf{r}) = -\mathrm{i}\omega\mu(\mathbf{r})\int_{\mathbb{R}^3}\overline{\mathbf{G}}_E(\mathbf{r},\mathbf{r}')\cdot\mathbf{J}_e(\mathbf{r}')\mathrm{d}\mathbf{r}'$,

$$\begin{aligned}\mathbf{E} =& \mathbf{E}^{\mathrm{inc}}(\mathbf{r}) - \mathrm{i}\omega\mu\int_{\Omega\setminus V_\delta}\mathrm{i}\omega\Delta\epsilon(\mathbf{r}')\mathbf{E}(\mathbf{r}')\overline{\mathbf{G}}_E(\mathbf{r},\mathbf{r}')\mathrm{d}\mathbf{r}'\\ &-\mathrm{i}\omega\mu\left[\bar{\mathbf{I}} + \frac{1}{k^2}\nabla\nabla\right]\int_{V_\delta}\mathrm{i}\omega\Delta\epsilon(\mathbf{r}')\mathbf{E}(\mathbf{r}')g(\mathbf{r},\mathbf{r}')\mathrm{d}\mathbf{r}'.\end{aligned} \tag{208}$$

In order to calculate the last integral accurately, a small digression is necessary. Let $R = |\mathbf{r}-\mathbf{r}'|$ and consider the Taylor expansion of $g(\mathbf{r},\mathbf{r}')$:

$$g(\mathbf{r},\mathbf{r}') = \frac{1}{4\pi R} - \frac{\mathrm{i}k}{4\pi} + \frac{(\mathrm{i}k)^2}{4\pi}\frac{R}{2!} - \frac{(\mathrm{i}k)^3}{4\pi}\frac{R^2}{3!} + \frac{(\mathrm{i}k)^4}{4\pi}\frac{R^3}{4!} - \frac{(\mathrm{i}k)^5}{4\pi}\frac{R^4}{5!} + \cdots \tag{209}$$

Let $g_0(\mathbf{r},\mathbf{r}') = \frac{1}{4\pi R}$ be the first term of the Taylor expansion. Then $\widetilde{g}(\mathbf{r},\mathbf{r}') = g(\mathbf{r},\mathbf{r}') - g_0(\mathbf{r},\mathbf{r}')$ has the real part of its singularity reduced. The imaginary part has its singularity reduced by our choice of interpolation, given later.

Also, Integrating the dominate part of the singular term, we get the **L**-dyadic for when V_δ is a sphere [22][44]:

$$\nabla\nabla \int_{V_\delta} g_0(\mathbf{r},\mathbf{r}')\mathrm{d}\mathbf{r}' = -\int_{\partial V_\delta} \frac{(\mathbf{r}-\mathbf{r}')\,\mathbf{u}_n(\mathbf{r}')}{4\pi|\mathbf{r}-\mathbf{r}'|^3}\mathrm{d}s' = -\mathbf{L}_{V_\delta} = -\frac{1}{3}\mathbf{I}, \tag{210}$$

where $\mathbf{u}_n(\mathbf{r}')$ is the unit normal vector at $\mathbf{r}'$. By subtracting and adding the term $\nabla\nabla \int_{V_\delta} g_0(\mathbf{r},\mathbf{r}')\Delta\epsilon(\mathbf{r})\mathbf{E}(\mathbf{r})\mathrm{d}\mathbf{r}'$, we get

$$\begin{aligned}
&\nabla\nabla \int_{V_\delta} \mathrm{d}\mathbf{r}'\Delta\epsilon(\mathbf{r}')\mathbf{E}(\mathbf{r}')g_0(\mathbf{r},\mathbf{r}') \\
&= \nabla\nabla \int_{V_\delta} g_0(\mathbf{r},\mathbf{r}')\Delta\epsilon(\mathbf{r})\mathbf{E}(\mathbf{r})\mathrm{d}\mathbf{r}' + \int_{V_\delta} \nabla\nabla g_0(\mathbf{r},\mathbf{r}')\left[\Delta\epsilon(\mathbf{r}')\mathbf{E}(\mathbf{r}') - \Delta\epsilon(\mathbf{r})\mathbf{E}(\mathbf{r})\right]\mathrm{d}\mathbf{r}' \\
&= -\mathbf{L}_{V_\delta}\Delta\epsilon(\mathbf{r})\mathbf{E}(\mathbf{r}) + \int_{V_\delta} \nabla\nabla g_0(\mathbf{r},\mathbf{r}')\left[\Delta\epsilon(\mathbf{r}')\mathbf{E}(\mathbf{r}') - \Delta\epsilon(\mathbf{r})\mathbf{E}(\mathbf{r})\right]\mathrm{d}\mathbf{r}'.
\end{aligned} \tag{211}$$

The remaining integral has the singularity reduced by one order because the electric field at $\mathbf{r}$ is subtracted. The remaining singularity is $O(1/R^2)$ and can be removed through the use of spherical coordinates.

Returning to the VIE derivation, (208) can now be written as

$$\begin{aligned}
\mathbf{C}\cdot\mathbf{E} = \mathbf{E}^{\mathrm{inc}}(\mathbf{r}) &- i\omega\mu \int_{\Omega\setminus V_\delta} i\omega\Delta\epsilon(\mathbf{r}')\overline{\mathbf{G}}_{\mathbf{E}}(\mathbf{r},\mathbf{r}')\cdot\mathbf{E}(\mathbf{r}') \\
&+ \omega^2\mu \int_{V_\delta} \mathrm{d}\mathbf{r}'\Delta\epsilon(\mathbf{r}')\mathbf{E}(\mathbf{r}')g(\mathbf{r},\mathbf{r}') \\
&+ \frac{\omega^2}{k^2}\mu \int_{V_\delta} \mathrm{d}\mathbf{r}'\Delta\epsilon(\mathbf{r}')\nabla\nabla\widetilde{g}(\mathbf{r},\mathbf{r}')\cdot\mathbf{E}(\mathbf{r}') \\
&+ \frac{\omega^2}{k^2}\mu \int_{V_\delta} \mathrm{d}\mathbf{r}'\nabla\nabla g_0(\mathbf{r},\mathbf{r}')\left[\Delta\epsilon(\mathbf{r}')\mathbf{E}(\mathbf{r}') - \Delta\epsilon(\mathbf{r})\mathbf{E}(\mathbf{r})\right],
\end{aligned} \tag{212}$$

where $\mathbf{C} = \mathbf{I} + \mathbf{L}_{V_\delta}\cdot\Delta\epsilon(\mathbf{r}) = \mathbf{I} + \frac{1}{3}\mathbf{I}\cdot\Delta\epsilon(\mathbf{r})$. We have assumed that $\Delta\epsilon(\mathbf{r})\mathbf{E}(\mathbf{r})$ is differentiable in V_δ and Hölder continuous. While the last three integrals are necessary

for calculating the CPV correctly, they can be omitted if δ is small enough that the desired accuracy can be obtained without them. The contribution of the integrals over V_δ are on the following orders:

$$\begin{aligned}
\left| \int_{V_\delta} \Delta\epsilon(\mathbf{r}')\mathbf{E}(\mathbf{r}')g(\mathbf{r},\mathbf{r}')\mathrm{d}\mathbf{r}' \right| &\leq C_1 ||\Delta\epsilon\mathbf{E}||_\infty \delta^2, \\
\left| \int_{V_\delta} \Delta\epsilon(\mathbf{r}')\nabla\nabla\widetilde{g}(\mathbf{r},\mathbf{r}')\cdot\mathbf{E}(\mathbf{r}')\mathrm{d}\mathbf{r}' \right| &\leq C_2 ||\Delta\epsilon\mathbf{E}||_\infty \delta^2, \\
\left| \int_{V_\delta} \nabla\nabla g_0(\mathbf{r},\mathbf{r}') \left[\Delta\epsilon(\mathbf{r}')\mathbf{E}(\mathbf{r}') - \Delta\epsilon(\mathbf{r})\mathbf{E}(\mathbf{r})\right] \mathrm{d}\mathbf{r}' \right| &\leq C_3 ||\Delta\epsilon\mathbf{E}||_{2,\infty} \delta^2,
\end{aligned} \tag{213}$$

where C_1, C_2, C_3 are constants; $\|\cdot\|_\infty$ and $\|\cdot\|_{2,\infty}$ are the $L^\infty(V_\delta)$ norms of a function and its second derivative, respectively.

4.3 Nyström Collocation Method for VIEs

We will use a Nyström method to numerically solve (212). Let $\Omega = \bigcup_{i=1}^N \Omega_i$ where Ω_i are discrete regions such as cubes, rectangles, cylinders, spheres, or ellipsoids. On each Ω_i, let $\{\phi_{ij} : 1 \leq j \leq M\}$ be a set of scalar basis functions that satisfy the Kronecker-delta property. For some coefficients $\mathbf{c}_{ij}$, $\mathbf{E}(\mathbf{r})$ can be expressed as

$$\mathbf{E}(\mathbf{r}) = \sum_{i=1}^{N}\sum_{j=1}^{M} \mathbf{c}_{ij}\phi_{ij}(\mathbf{r}), \qquad \mathbf{r} \in \Omega_i. \tag{214}$$

Letting V_δ^{ij} be the exclusion centered at $\mathbf{r}_{ij}$, (212) becomes

$$\begin{aligned}
\mathbf{C}\cdot\mathbf{c}_{ij} = \mathbf{E}_{ij}^{\mathrm{inc}} &+ \omega^2\mu \sum_{n=1}^{N}\sum_{m=1}^{M} \left[\int_{\Omega_n \setminus V_\delta^{ij}} \Delta\epsilon(\mathbf{r}')\bar{\mathbf{G}}_{\mathbf{E}}(\mathbf{r}_{ij},\mathbf{r}')\phi_{nm}(\mathbf{r}') \right] \cdot \mathbf{c}_{nm}\mathrm{d}\mathbf{r}' \\
&+ \omega^2\mu \sum_{m=1}^{M} \left[\int_{V_\delta^{ij}} \Delta\epsilon(\mathbf{r}')g(\mathbf{r}_{ij},\mathbf{r}')\phi_{im}(\mathbf{r}') \right] \cdot \mathbf{c}_{im}\mathrm{d}\mathbf{r}' \\
&+ \frac{\omega^2\mu}{k^2} \sum_{m=1}^{M} \left[\int_{V_\delta^{ij}} \Delta\epsilon(\mathbf{r}')\nabla\nabla\widetilde{g}(\mathbf{r}_{ij},\mathbf{r}')\phi_{im}(\mathbf{r}') \right] \cdot \mathbf{c}_{im}\mathrm{d}\mathbf{r}' \\
&+ \frac{\omega^2\mu}{k^2} \sum_{m=1}^{M} \int_{V_\delta^{ij}} \nabla^2 g_0(\mathbf{r}_{ij},\mathbf{r}') \left[\Delta\epsilon(\mathbf{r}')\phi_{im}(\mathbf{r}') - \Delta\epsilon_{ij}\phi_{im}(\mathbf{r}_{ij})\right] \cdot \mathbf{c}_{im}\mathrm{d}\mathbf{r}'.
\end{aligned} \tag{215}$$

Thus far, the integrals over V_δ^{ij} have been evaluated by a brute-force quadrature in spherical coordinates. Meanwhile, due to the Kronecker-delta property of the basis functions, the integrals over $\Omega_n \backslash V_\delta^{ij}$ can be evaluated with only one function evaluation each if the sample points for the quadrature rule with point-weight pairs $(\mathbf{r}_{k\ell}, w_{k\ell})$ coincide with the sample points for the basis functions:

$$\begin{aligned}
&\omega^2\mu \sum_{n=1}^{N}\sum_{m=1}^{M}\left[\int_{\Omega_n\backslash V_\delta^{ij}} \Delta\epsilon(\mathbf{r}')\bar{\mathbf{G}}_{\mathbf{E}}(\mathbf{r}_{ij},\mathbf{r}')\phi_{nm}(\mathbf{r}')\mathrm{d}\mathbf{r}'\right]\cdot\mathbf{c}_{nm} \\
&\quad= \omega^2\mu \sum_{n=1}^{N}\sum_{m=1}^{M}\left[\sum_{k=1}^{N}\sum_{\ell=1}^{M}\Delta\epsilon(\mathbf{r}')\bar{\mathbf{G}}_{\mathbf{E}}(\mathbf{r}_{ij},\mathbf{r}_{k\ell})\phi_{nm}(\mathbf{r}_{k\ell})w_{k\ell}\right]\cdot\mathbf{c}_{nm} \qquad (216)\\
&\quad= \omega^2\mu \sum_{n=1}^{N}\sum_{m=1}^{M}\left[\Delta\epsilon(\mathbf{r}')\bar{\mathbf{G}}_{\mathbf{E}}(\mathbf{r}_{ij},\mathbf{r}_{nm})w_{nm}\right]\cdot\mathbf{c}_{nm}.
\end{aligned}$$

If a singularity is present in the above integral, even if $\mathbf{r}_{ij} = \mathbf{r}_{nm}$, it is accounted for by the quadrature weights $w_{k\ell}$ given by the formulas (91) and (150). While (216) represents the speed increases of the Nyström method, the exact nature of the approximations are not given explicitly. To elucidate the series of approximation made in the Nyström method, let $\mathbf{E}_e$ be the exact solution for the electric field defined by the integral equation (212). Next, assume that basis functions with p sample points are used in (214). Let $\mathbf{E}_p$ be the projection of $\mathbf{E}_e$ onto the subspace spanned by these basis functions. $\mathbf{E}_p$ corresponds to (215). As p increases, $\mathbf{E}_p \to \mathbf{E}_e$. Next, we approximate $\mathbf{E}_p$ by discretizing the integrals in (215) with a q point quadrature rule. Recall that the sample points for the quadrature rule are the sample points of the basis functions used in (214). Let $\mathbf{E}_{p,q}$ be the result of solving (215) with discretized integral operators. As q increases, $\mathbf{E}_{p,q} \to \mathbf{E}_p$. In the Nyström collocation method, we take $p = q$ and increase them both at the same rate so that we take advantage of

the speed increase in (216). In the numerical results section, we verify that $\mathbf{E}_{p,q} \to \mathbf{E}_e$ as p and q increase together.

Before giving the final matrix for a the VIE, a digression is necessary to comment on how the quadrature rule integrates the Green's function. Recall that

$$\overline{\mathbf{G}}_{\mathbf{E}}(\mathbf{r}, \mathbf{r}') = \frac{e^{-ikR}}{4\pi R}(\mathbf{I} - \mathbf{u} \otimes \mathbf{u}) - \frac{ie^{-ikR}}{4\pi R^2 k}(\mathbf{I} - 3\mathbf{u} \otimes \mathbf{u}) - \frac{e^{-ikR}}{4\pi R^3 k^2}(\mathbf{I} - 3\mathbf{u} \otimes \mathbf{u}), \quad (217)$$

where $\mathbf{u} = (\mathbf{r} - \mathbf{r}')/R$ and $\otimes$ the outer product for vectors. The weights for integrating $\overline{\mathbf{G}}_{\mathbf{E}}(\mathbf{r}, \mathbf{r}')$ contain both the singularity and the dyadic, directional part $\mathbf{u} \otimes \mathbf{u}$ so that the convergence of the quadrature formula (89) depends on the ability of the basis functions to accurately interpolate $e^{-ikR} = \cos(kR) + i\sin(kR)$, similar to the situation in Figs. 28–36. As stated for those figures, $\sin(kR)/R$ is interpolated instead of $\sin(kR)$ whenever possible to avoid the cusp at $R = 0$ present in $\sin(kR)$; doing so reduces the singularity present in the imaginary part of the Green's function.

The resulting matrix equation has the form

$$\mathbf{V} \cdot \vec{\mathbf{c}} = \begin{bmatrix} \mathbf{V}_{xx} & \mathbf{V}_{xy} & \mathbf{V}_{xz} \\ \mathbf{V}_{yx} & \mathbf{V}_{yy} & \mathbf{V}_{yz} \\ \mathbf{V}_{zx} & \mathbf{V}_{zy} & \mathbf{V}_{zz} \end{bmatrix} \cdot \begin{bmatrix} \mathbf{c}_x \\ \mathbf{c}_y \\ \mathbf{c}_z \end{bmatrix} = \begin{bmatrix} \mathbf{E}_x^{\text{inc}} \\ \mathbf{E}_y^{\text{inc}} \\ \mathbf{E}_z^{\text{inc}} \end{bmatrix}, \quad (218)$$

where $\mathbf{V}$ is an easily invertible Fredholm operator. The matrix equation is solved by GMRES.

4.4 Numerical Results

We provide numerical results pertaining to several aspects of our method. First, we confirm that the correction terms are order δ^2. Second, we demonstrate that our

Table 10: Convergence of the nonzero matrix entries when the singularity is at center when correction terms are omitted.

	$\delta = 0.1$	$\delta = 0.05$	$\delta = 0.025$	$\delta = 0.0125$
Integral	3.985701	4.017024	4.024872	4.026835
Error	4.1784E-2	1.0461E-2	2.613E-3	6.5E-4
Order	-	2	2	2

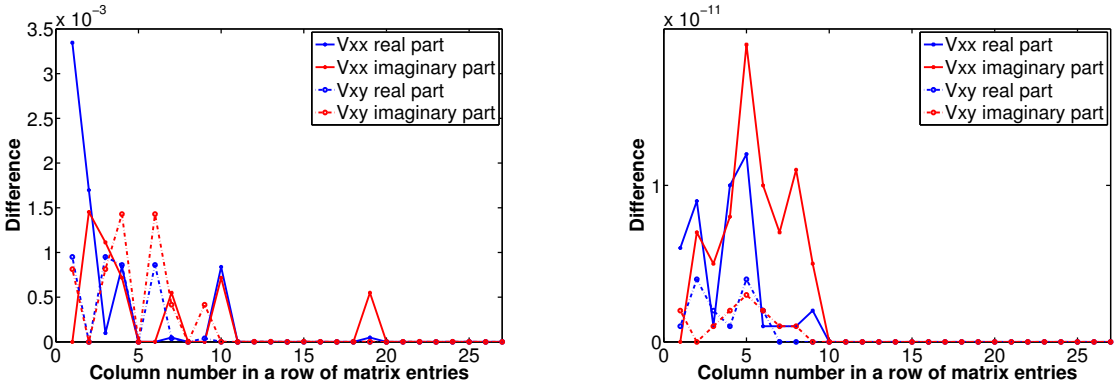

(a) (b)

Figure 40: Difference of matrix entries when $\delta = 0.1$ vs $\delta = 0.001$ when correction terms are omitted (a) and when they are included (b).

Nyström method obtains p-convergence. Third, we illustrate the efficiency of our method in handling a large number of scatterers.

4.4.1 The Correction Terms

In a first test, consider a cube with a singularity at its center. Then consider δ taking several values, approaching 0. Table 10 shows that the nonzero integrals converge at the expected rate of δ^2 when the correction terms are omitted from (215). Including the correction terms in (215) results in δ-independent matrix entries, as shown in Fig. 40. The same behavior has been observed in the many other cases that arise in computing the matrix entries. As such, the exact details of the computational experiment have been omitted.

4.4.2 p-Convergence

In a second test, convergence of the VIE solution under the relative L^2 function norm is verified when the number of basis functions, and therefore quadrature points, is increased. The relative L^2 norm of the difference between a reference $\mathbf{E}^{\text{ref}}$ and an approximation $\mathbf{E}^p$ is defined by

$$\frac{\|\mathbf{E}^p - \mathbf{E}^{\text{ref}}\|_{L^2(\Omega)}}{\|\mathbf{E}^{\text{ref}}\|_{L^2(\Omega)}}, \tag{219}$$

where

$$\begin{aligned} \|\mathbf{E}\|_{L^2(\Omega)} &= \sqrt{\int_\Omega |\mathbf{E}_x|^2 + |\mathbf{E}_y|^2 + |\mathbf{E}_z|^2 d\mathbf{r}} \\ &= \sqrt{\int_\Omega \text{re}(\mathbf{E}_x)^2 + \text{im}(\mathbf{E}_x)^2 + \text{re}(\mathbf{E}_y)^2 + \text{im}(\mathbf{E}_y)^2 + \text{re}(\mathbf{E}_z)^2 + \text{im}(\mathbf{E}_z)^2 d\mathbf{r}}, \end{aligned} \tag{220}$$

where $|\cdot|$ is the complex modulus. The integrals required for the norm are calculated by a brute-force integration method. This test is performed when the scatterer is a single cube, cylinder, or sphere, and the results are given in Figs. 41–43. The incident wave is $\mathbf{E}^{\text{inc}} = \mathbf{i}_x e^{ikz}$, where $k = 1$, though better results have been obtained for different incident waves. The reference solution is taken to be when m is one value larger for the cube and cylinder, and it is taken to be the MIE series solution to Maxwell's equations for the sphere. The MIE solution is given by

$$\mathbf{E}(r, \theta, \phi) = \sum_{n=1}^{\infty} \frac{i^n (2n+1)}{n(n+1)} \left(c_n \mathbf{M}_{o1n}^{(1)} - i d_n \mathbf{N}_{e1n}^{(1)} \right), \tag{221}$$

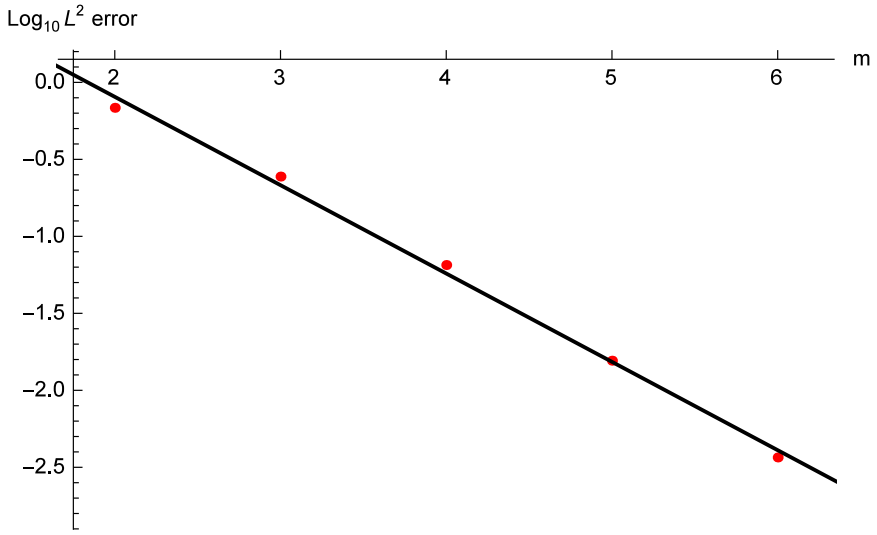

Figure 41: Convergence under the L^2 function norm for a cube with sides of length 2. Linear fit is given by $-0.57m + 1.1$.

where

$$\begin{aligned} c_n &= \frac{j_n(ka)[kah_n^{(1)}(ka)]' - h_n^{(1)}(ka)[kaj_n(ka)]'}{j_n(mka)[kah_n^{(1)}(ka)]' - h_n^{(1)}(ka)[mkaj_n(mka)]'}; \\ d_n &= \frac{mj_n(ka)[kah_n^{(1)}(ka)]' - mh_n^{(1)}(ka)[kaj_n(ka)]'}{m^2 j_n(mka)[kah_n^{(1)}(ka)]' - h_n^{(1)}(x)[mkaj_n(mka)]'}, \end{aligned} \tag{222}$$

and the vector special harmonics are

$$\mathbf{M_{o1n}^{(1)}} = \begin{pmatrix} 0 \\ \cos\phi \cdot \pi_n(\cos\theta) j_n(mkr) \\ -\sin\phi \cdot \tau_n(\cos\theta) j_n(mkr) \end{pmatrix}, \tag{223}$$

$$\mathbf{N_{e1n}^{(1)}} = \begin{pmatrix} n(n+1)\cos\phi \cdot \sin\theta \cdot \pi_n(\cos\theta)\dfrac{j_n(mkr)}{mkr} \\ \cos\phi \cdot \tau_n(\cos\theta)\dfrac{[mkrj_n(mkr)]'}{mkr} \\ -\sin\phi \cdot \pi_n(\cos\theta)\dfrac{[mkrj_n(mkr)]'}{mkr} \end{pmatrix}. \tag{224}$$

In the above formulas, m is the refractive index of the sphere relative to the ambient medium, a the radius of the sphere and k is the wave number of the ambient medium. The functions $j_n(z)$ and $h_n^{(1)}(z)$ are the spherical Bessel functions of first and third

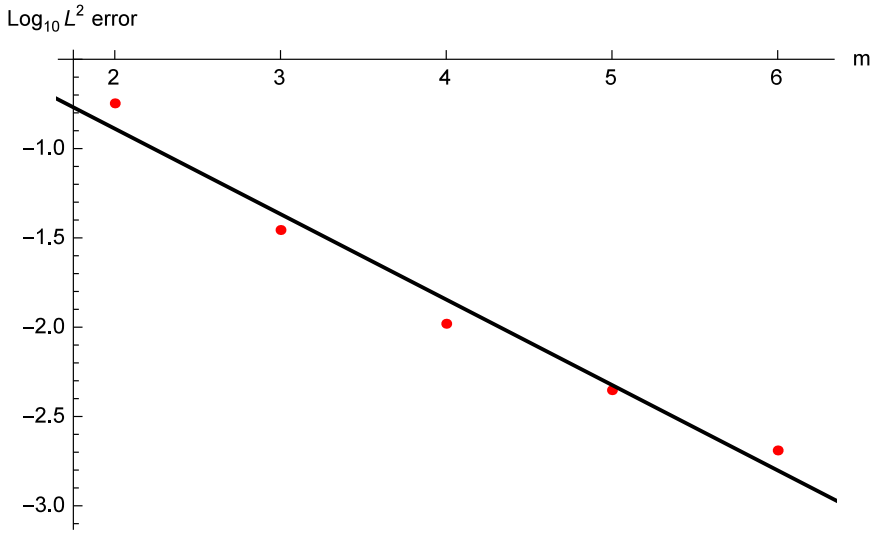

Figure 42: Convergence under the L^2 function norm for a cylinder of radius 1 and height 2. Linear fit is given by $-0.48m + 0.07$.

kind, respectively, and their derivatives have the relations

$$[zj_n(z)]' = zj_{n-1}(z) - nj_n(z); [zh_n^{(1)}(z)]' = zh_{n-1}^{(1)}(z) - nh_n^{(1)}(z), \tag{225}$$

where $\pi_n(\cos\theta)$ and $\tau_{\cos\theta}$ have the relations

$$\pi_n = \frac{2n-1}{n-1}\cos\theta \cdot \pi_{n-1} - \frac{n}{n-1}\pi_{n-2}; \tau_n = n\cos\theta \cdot \pi_n - (n+1)\pi_{n-1}, \tag{226}$$

with

$$\pi_0 = 0; \pi_1 = 1; \pi_2 = 3\cos\theta; \tau_0 = 0; \tau_1 = \cos\theta; \tau_2 = 3\cos 2\theta. \tag{227}$$

To illustrate the efficiency of the quadrature rule defined by (89), Table 11 shows the CPU time required for calculating the matrix entries for the sphere using our new tensor-product weights as well as using a brute-force approach. The other domains have produced similar timing results.

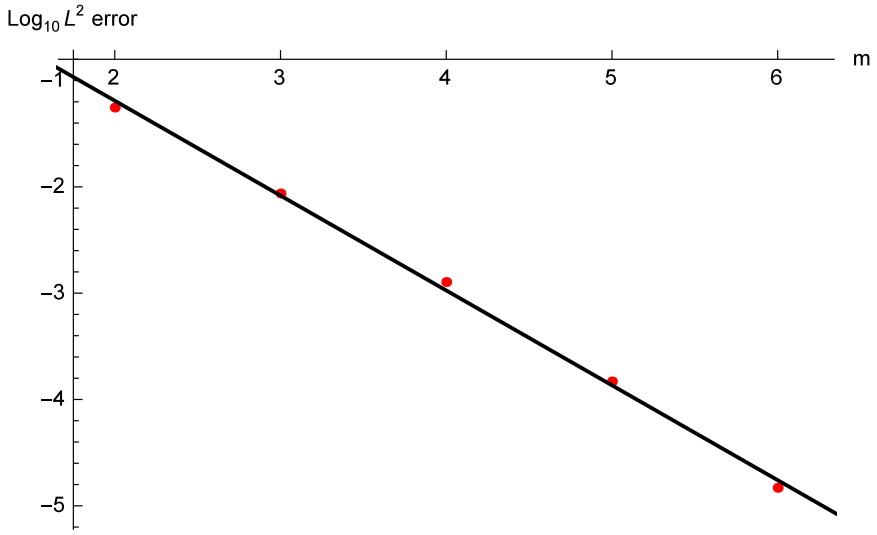

Figure 43: Convergence under the L^2 function norm for a sphere of radius 1. Linear fit is given by $-0.89m + 0.59$.

Table 11: Timing results for matrix construction for a single spherical domain.

m	M	Matrix Size	Interpolated weights	Brute-force
2	24	72×72	3ms	1.2h
3	72	216×216	32ms	20.7h
4	160	480×480	126ms	-
5	300	900×900	382ms	-
6	504	1512×1512	1171ms	-

4.4.3 Many Scatterers

In a third test, we consider a large number of scatterers in random arrangements, seen in Fig. 44. For cuboid scatterers, we considered a $15 \times 15 \times 3 = 675$ random arrangement with 27 collocation points for each cube with a side length of 0.5; required CPU time was 19 minutes. For spherical scatterers, we considered a $12 \times 12 \times 3 = 432$ random arrangement with 42 collocation points for each sphere of radius 1; required CPU time was 22 minutes.

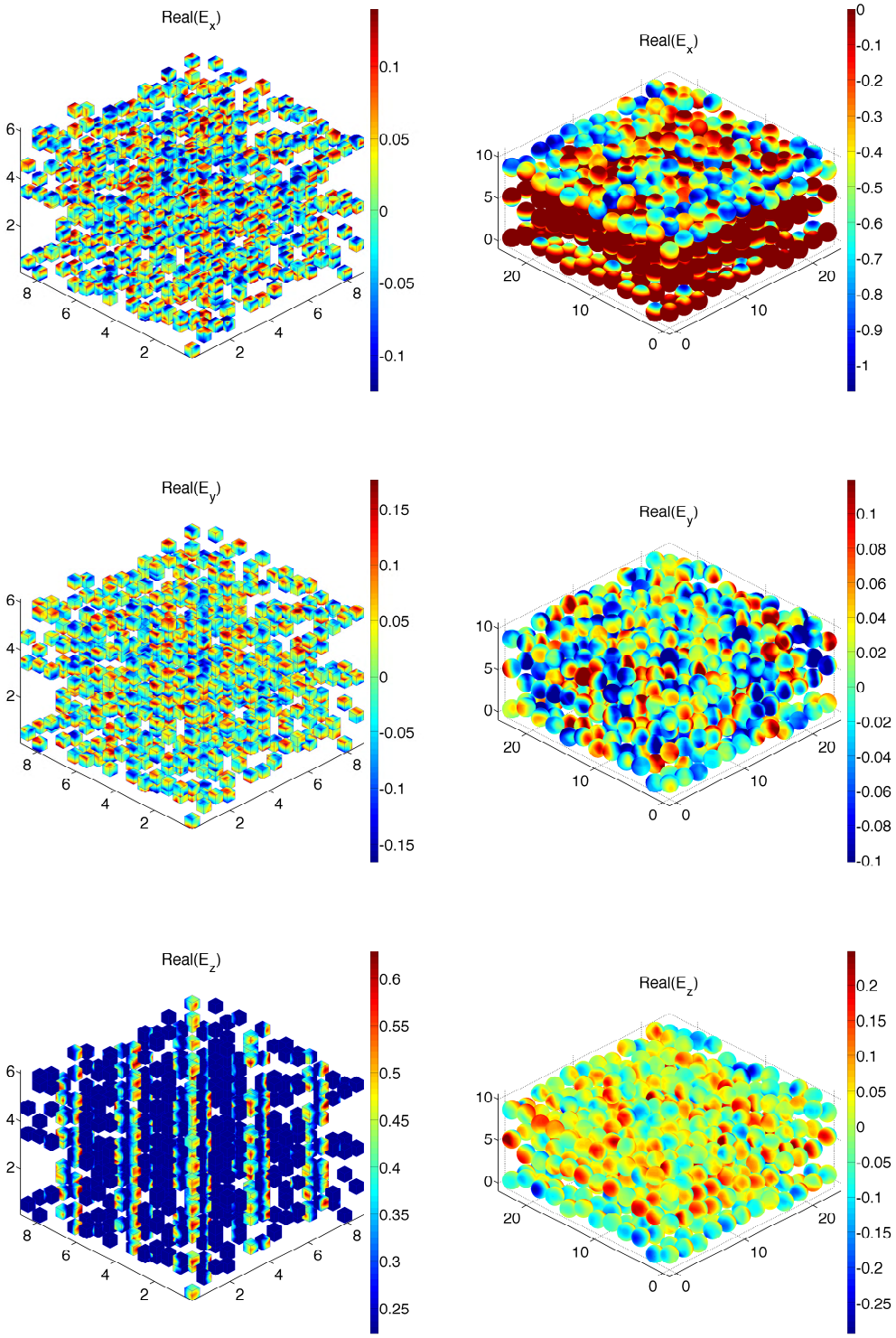

Figure 44: E_x, E_y, E_z for an arrangement of cubes (left) and an arrangement of spheres (right).

4.5 Future Work Concerning Scatterers

In the future, we would like to make a realistic model of a solar cell instead of a random arrangement of scatterers. One issue with is that the method does not produce good results when scatterers are too close. Thus, the near-singular behavior of the Green's function corresponding to a singularity in a nearby region needs to be addressed, possibly through the quadrature rule itself. A second issue is that while the code can handle the different types of scatterers at the same time, it is not clear what the ideal arrangement of scatters should be. In fact, finding the ideal arrangement of scatterers is one of the primary goals of this work and more sophisticated tests must be devised in order to find it. This effort will be aided with the development of the Green's function for layered media.

Thus far, the correction terms in (215) over V_δ have been calculated with 4,096 sample points in spherical coordinates. Since the integrands are simpler than $\hat{\mathbf{H}}$ in (151), the novel quadrature rule introduced in chapter 3 should be suitable for handling these integrals over the sphere V_δ. However, even using only $M = 42$ sample points in (89), the integral over V_δ is computationally expensive compared to the dominant integral over $\Omega \backslash V_\delta$, which requires only one sample point in the Nyström collocation method. Because the weights in (91) become very time consuming to calculate when δ is small, say when $\delta < 10^{-3}$, it is desirable to find a better way to approximate the correction terms. Otherwise, computational resources will limit the order of the VIE's accuracy to $\delta^2 = 10^{-6}$.

A second topic for future work involves adjusting the basis functions to account for

corner singularities in the electric field. These arise when the boundary between two materials with distinct dielectric constants has sharp corners. In the case of the cube and cylinder, there are edges whose interior angles are $\alpha = \pi/2$ and the problem is two-dimensional. For now, we ignore the three-dimensional problem associated with the vertices of the cube and proceed in a simplified way. Then the electric field, under certain conditions, near the edge can be expressed in polar coordinates $(\mathbf{u}_r, \mathbf{u}_\varphi)$ as [39]:

$$\mathbf{E}(r,\varphi) = \frac{A\nu}{r^{1-\nu}} \left[\cos(\nu(\varphi+\alpha))\mathbf{u}_r - \sin(\nu(\varphi+\alpha))\mathbf{u}_\varphi\right], \tag{228}$$

where $\nu = \pi/(2\pi - \alpha) = 2/3$. Since $\mathbf{E}(r,\varphi)$ behaves differently under different circumstances, we only require that (228) has a very weak singularity $1/r^{1-\nu}$, $\nu > 0$, and the electric field depends on the angle φ. For now, we will also work in two dimensions, on a square, and we will use the moving least-squared technique found in [18] to construct basis functions similar to those found in intrinsic finite element method literature. The moving least squared technique begins with a set of monomials, stored in a vector $\mathbf{p}(x,y)$. For bi-linear or bi-quadratic interpolation,

$$\begin{aligned} \mathbf{p}(x,y) &= (1,x,y,xy), \\ \mathbf{p}(x,y) &= (1,x,y,x^2,xy,y^2,x^2y,xy^2,(xy)^2). \end{aligned} \tag{229}$$

Next, we add to the vector $\mathbf{p}(x,y)$ all the functions that will capture the singularity. In our case, we add four functions of the form $\mathbf{E}(r,\varphi)/A$ that have been recentered and rotated to the corners of the square appropriately. For sample points in the moving least-square method, we use the tensor-product of Gauss points, where the total number of sample points must be equal to or greater than the length of $\mathbf{p}(x,y)$. For a

Table 12: Approximate absolute errors due to interpolation. Since the singularity is in the span of the IXFEM basis, its convergence rate is dominated by error due to interpolating $\cos(\sqrt{x^2+y^2})$.

	Near corner ($r < 0.02$)		Near center ($r > 0.05$)	
Degree	IXFEM	FEM	IXFEM	FEM
bi-linear	0.5	2	0.3	0.3
bi-quadratic	0.05	1.5	0.006	0.2
bi-cubic	0.01	1.5	0.006	0.06
bi-quartic	0.0002	1	0.0001	0.03

function to attempt to approximate, let $\mathbf{e}(x, y)$ be the sum of $\cos(\sqrt{x^2+y^2})$ and four singular functions $2\mathbf{E}(r, \varphi)/A$, where $\mathbf{E}(r, \varphi)$ is recentered and rotated to the corners of the square appropriately. We test convergence by attempting to interpolate $\mathbf{e}(x, y)$ with the moving least-square functions (IXFEM), which contain the singularities in the span of $\mathbf{p}(x, y)$, and the Lagrange polynomials (FEM) that correspond to the monomials in $\mathbf{p}(x, y)$. Table 12 shows the convergence for both sets of basis functions. Unfortunately, the moving least-square basis functions require a matrix inversion to be calculated each time they are evaluated and they fail to satisfy the Kronecker delta property. There is a possibility that the technique could be modified to product basis functions with the Kronecker delta property, which is required for the Nyström collocation method. The moving least-square basis functions are often referred to as intrinsic extended finite element method basis functions. For extrinsic extended finite element method basis functions, function evaluation does not involve matrix inversion and, for a function u to be interpolated, we have [17]

$$u(x, y) \approx \sum_{i=1}^{N} N_i(x, y) u_i + \sum_{j=1}^{N'} \sum_{k=1}^{M} \hat{N}_j(x, y) \psi_k(x, y) a_{j,k}, \tag{230}$$

where $N_i(x, y)$ and $\hat{N}_j(x, y)$ are the usual Lagrange basis functions, u_i are the usual

interpolation coefficients, $\psi_k(x, y)$ contain the information about the corner singularities, and $a_{j,k}$ are the interpolation coefficients for the singular part. However, even after modifying the interpolation formula, as described in [17], only the usual Lagrange basis functions satisfy the Kronecker delta property. At this time, convergence as the basis functions increase in degree is uncertain; in the finite element method, extrinsic extended finite element method basis functions are only ever used when $\hat{N}_j(x, y)$ are linear. Finally, even though these extrinsic basic functions are not as computationally intensive as the intrinsic basis functions, they introduce the additional unknowns $a_{j,k}$ into the matrix equation, increasing the memory and time requirements for constructing the matrix. In summary, if the general nature of the singularity is known, the basis functions can be adjusted by utilizing intrinsic or extrinsic extended finite element method basis functions so that the family of functions containing the singularity is in the span of the basis functions. Then, the error due to interpolation is independent of the singularity's presence.

4.6 Summary for Modeling Scattering with the Maxwell Equations

In this chapter, an accurate and efficient Nyström VIE method was developed to simulate the scattering of multiple cubes, cylinders, and spheres. Special attention was given to integrating the hyper-singular dyadic Green's function through the introduction of correction terms and interpolated quadrature weights. Numerical results confirm that exponential p-convergence is obtained.

CHAPTER 5: CONCLUSION

This dissertation is concerned with more than presenting models of the physical world. Throughout, it has emphasized mathematical analysis, techniques, and principals. Thus, the first part of the conclusion will give a brief overview of the models presented in chapters 2 and 4. The second part will summarize the most significant mathematical topic presented in the dissertation, the treatment of singular integrands.

5.1 Models of Physical Phenomena

In chapter 2, the electrostatic potential was calculated when inhomogeneities were present in a layered medium. These inhomogeneities took the form of an ion channel and a Janus particle. For the ion channel, we demonstrated that the potential and self energy inside the channel can be computed to a high degree of accuracy. This is significant in the study of selectivity filters present in ion channels that utilize diffusion. Specifically, one application of the ion channel model is to determine why one type of atom can pass through a channel and another cannot. For the Janus particle, we showed that our method can capture how the gradient of the electrostatic potential changes with the dielectric constants for each hemisphere. Since a small number of Janus particles are introduced to a given substance to affect how it behaves with respect to electromagnetic stimuli, being able to capture their behavior is a fundamental step towards modeling colloidal substances containing Janus particles.

In chapter 4, electromagnetic wave scattering due to a set of inhomogeneities was calculated. Analysis of the scattering can give information concerning how much energy was absorbed by the object from a given incident wave. This information is necessary for investigating the relationship between rough surfaces, made from several simple geometries, and the amount of energy absorbed. Moreover, the analysis must be repeated for many different geometries and many different incident waves. The strength of our method lies in its efficiency, which makes this analysis for a large number of physical circumstances possible.

5.2 Singular Integrands

Each topic addressed in this dissertation dealt with the special treatment of singular integrands. As such, the fact that they arise through the use of Green's functions and must be handled appropriately is the common thread that links the topics of this dissertation.

In chapter 2, the Green's function was weakly singular. Even though the Green's function's first and second derivatives were used, they were only used in circumstances where they contributed a weakly singular integrand. Specifically, the first normal derivative is made of two parts, the strongly singular gradient of the Green's function and the normal vector to the boundary. Since the gradient part contains the vector $\mathbf{r}-\mathbf{r}'$, which is orthogonal to the normal vector when $\mathbf{r}=\mathbf{r}'$, the strongly singular nature of the first normal derivative is reduced to a weakly singular integrand. This reduction occurs because we consider the integral equations on the boundary. In contrast, the part of the second normal derivative that is hyper-singular on the boundary is only

strongly singular in general, i.e., working on the boundary reduces the term that is, in general, hyper-singular to weakly singular and increases a second term from strongly singular to hyper-singular. Thus, we only consider the second normal derivative as the difference across the boundary, which is only weakly singular. Since all of the singularities can be treated in a weakly singular way after some mathematical manipulation, they can be removed through the introduction of polar coordinates centered at the singularity. In this sense, the singular integrals in chapter 2 are easy to compute accurately as the difficulties, due to strong and hyper-singularities, were addressed through mathematical manipulations.

In chapter 3, a general method for handling singular integrands in was introduced. While the method was presented in three dimensions, it can be applied to other spaces as long as an analog of polar or spherical coordinates is available. Since the Jacobian for spherical coordinates (ρ, ϕ, θ) contains ρ^2, this method can handle weak and strong singularities with ease; in this way, the spherical coordinates used in chapter 3 play the exact same role as the polar coordinates in chapter 2. Furthermore, this method illustrates its efficiency in approximating the CPV of hyper-singular integrals because, even when a large number of sample points are required in spherical coordinates to handle the singularity, the number of sample points required at runtime depends only on the nonsingular part of the integrand.

In chapter 4, the Green's function was hyper-singular. First, there is the issue of singular integration when the singularity is in the domain of integration Ω. The method in chapter 3 was used to approximate the CPV by omitting a sphere V_δ from Ω. Then, the task is reduced to calculating the integral over V_δ; it is broken into

the integral over the weakly singular parts and the hyper-singular part. The hyper-singular part is approximated by subtracting the first term of the Taylor expansion for the nonsingular part. However, the problem remains that the integral over V_δ is computationally intense. Fortunately, if the correction terms are omitted, we commit an error on the order of δ^2, which is acceptable in many circumstances.

In conclusion, singular integrals are usually best handled in a way that accounts for the context from which they arise. However, general methods that rely on polar or spherical coordinates can be relevant if a way to reduce the number of required sample points is introduced.

PUBLICATIONS

D. Chen, W. Cai, B. Zinser, and M. Cho. Accurate and Efficient Nyström Volume Integral Equation Method for the Maxwell equations for Multiple 3-D Scatterers. *J. of Comput. Phys.*, To appear, 2016.

B. Zinser, W. Cai, and D. Chen. Quadrature Weights on Tensor-Product Nodes for Accurate Integration of Hypersingular Functions over Some Simple 3-D Geometric Shapes. *CiCP*, To appear, 2016.

B. Zinser and W. Cai. A Well-Conditioned Hypersingular Boundary Element Method for Electrostatic Potentials in the Presence of Inhomogeneities within Layered Media. *CiCP*, To appear, 2016.

REFERENCES

[1] *Mathematica 10*. Wolfram Research Inc., 2014.

[2] K. Atkinson and I. Graham. Iterative variants of the Nyström method for second kind boundary integral operators. *SIAM J. Sci. Stat. Comput.*, pages 694–722, 1990.

[3] H. Atwater. The promise of Plasmonics. *Scientific American*, pages 56–62, 2007.

[4] J. Boyd. *Chebyshev and Fourier Spectral Methods*. Dover, 2001.

[5] J. Bremer. On the Nyström discretization of integral equations on planar curves with corners. *Appl. Comput. Harmon. Anal.*, pages 45–64, 2012.

[6] W. Cai. *Computational Methods for Electromagnetic Phenomena: electrostatics in solvation, scattering, and electron transport*. Cambridge University Press, 2013.

[7] W. Cai, S. Deng, and D. Jacobs. Extending the fast multipole method to charges inside or outside a dielectric sphere. *J. Comput. Phys.*, pages 846–864, 2007.

[8] G. Chandler. Galerkin's method for boundary integral equations on polygonal domains. *J. Aust. Math. Soc. Ser. B, Appl. Math.*, pages 1–13, 1984.

[9] D. Chen, W. Cai, B. Zinser, and M. Cho. Accurate and Efficient Nyström Volume Integral Equation Method for the Maxwell equations for Multiple 3-D Scatterers. *J. of Comput. Phys.*, To appear, 2016.

[10] L. Chen, M. Holst, and J. Xu. The finite element approximation of the nonlinear Poisson-Boltzmann equation. *SIAM J. Numer. Anal.*, pages 2298–2320, 2007.

[11] I.L. Chern, J.G. Lie, and W.C. Wang. Accurate evaluation of electrostatics for macromolecules in solution. *Meth. Appl. Anal.*, pages 309–328, 2003.

[12] R.E. Collin. *Field Theory of Guided Waves*. Wiley-IEEE Press, 1990.

[13] S. Deng and W. W. Cai. Analysis and application of an orthogonal nodal basis on triangles for discontinuous spectral element methods. *Appl. Num. Anal. Comp. Math.*, pages 326–345, 2005.

[14] Q. Du. Evaluations of certain hypersingular integrals on interval. *Int. J. for Num. Meth. in Eng.*, pages 1195–1210, 2001.

[15] D. Dunavant. High degree efficient symmetrical gaussian quadrature rules for the triangle. *IJNME*, pages 1129–1148, 1985.

[16] F. Fogolari, A. A. Brigo, and H. Molinari. The Poisson-Boltzmann equation for biomolecular electrostatics: a tool for structural biology. *J. Mol. Recognit.*, pages 377–392, 2002.

[17] T.P. Fries. Overview and comparison of different variants of the XFEM. *Proc. Appl. Mech.*, pages 27–30, 2014.

[18] T.P. Fries and T. Belytschko. The intrinsic XFEM: a method for arbitrary discontinuities without additional unknowns. *Int. J. Numer. Meth. Engng.*, pages 1358–1385, 2006.

[19] Y.Q. Fu and X. Zhou. Plasmonic lenses: a review. *Plasmonics*, pages 287–310, 2010.

[20] P. Keast. Moderate-Degree Tetrahedral Quadrature Formulas. *Comp. Meth. in Appl. Mech. and Engng.*, pages 339–348, 1986.

[21] R.A. Kress. A Nyström method for boundary integral equations in domains with corners. *Numer. Math.*, pages 145–161, 1990.

[22] S.W. Lee, J. Boersma, C.L. Law, and G.A. Deschamps. Singularity in Green's function and its numerical evaluation. *IEEE Transaction on Antennas and Propagation*, pages 311–317, 1980.

[23] H. Lin, H. Tang, and W. Cai. Accuracy and efficiency in computing electrostatic potential for an ion channel model in layered dielectric/electrolyte media. *J. of Comput. Phys.*, pages 448–512, 2013.

[24] P. Linz. On the approximate computation of certain strongly singular integrals. *Comput.*, pages 345–353, 1985.

[25] D. Liu, X. Zhang, and J. Wu. A collocation scheme for a certain Cauchy singular integral equation based on the superconvergence analysis. *Appl. Math. and Comput.*, pages 5198–5209, 2013.

[26] D. Liu, X. Zhang, and D. Yu. The superconvergence of the Newton-Cotes rule for Cauchy principal value integrals. *J. of Comput. and Appl. Math.*, pages 696–707, 2010.

[27] S. Maier. *Plasmonics: Fundamentals and Applications*. Springer, 2007.

[28] C. Müller. *Foundations of the Mathematical Theory of Electromagnetic Waves*. Springer-Verlag, 1969.

[29] J.C. Nédélec. *Acoustic and Electromagnetic Equations: Integral Representations for Harmonic Problems*. Springer-Verlag, 2001.

[30] J.B. Pendry. Negative refraction makes a perfect lens. *Physical Review Letters*, pages 3966–3969, 2000.

[31] H. Raether. *Surface plasmons on smooth and rough surfaces and gratings*. Springer Tracts in Modern Physics, 1988.

[32] C.V. Raman and K.S. Krishnan. A new type of secondary radiation. *Nature*, page 501, 1928.

[33] V. Rokhlin. Solution of acoustic scattering problem by means of second kind of integral equations. *Wave Motion*, pages 257–272, 1983.

[34] J. Shen. Efficient spectral-Galerkin methods IV. Spherical geometries. *SIAM J. Sci. Comput.*, pages 1438–1455, 1999.

[35] W.C. Still, A. Tempczyk, R.C. Hawley, and T. Hendrickson. Semianalytical treatment of solvation for molecular mechanics and dynamics. *J. Am. Chem. Soc.*, pages 6127–6129, 1990.

[36] J.A. Stratton. *Electromagnetic Theory*. New York: McGraw-Hill, 1941.

[37] W. Sun and J. Wu. Newton-Cotes formulae for the numerical evaluation of certain hypersingular integrals. *Comput.*, pages 297–309, 2005.

[38] M.S. Tong and W.C. Chew. Super-hyper singularity treatment for solving 3D electric field integral equations. *Microwave and Optical Technology Letters*, pages 1383–1388, 2007.

[39] J. van Bladel. *Singular Electromagnetic Fields and Sources*. Oxford University Press, 1991.

[40] A. Walther and A.H.E. Müller. Janus Particles: Synthesis, Self-Assembly, Physical Properties, and Applications. *Chem. Rev.*, pages 5194–5261, 2013.

[41] J. Wu and W. Sun. The superconvergence of Newton-Cotes rules for the Hadamard finite-part integral on an interval. *Numer. Math.*, pages 143–165, 2008.

[42] J. Wu and D. Yu. An approximate computation of hypersingular integrals on interval. *J. Num. Method and Comp. Appl.*, pages 118–126, 1998.

[43] Z.L. Xu and W. Cai. Fast analytical methods for macroscopic electrostatic models in biomolecular simulations. *SIAM Review*, pages 683–720, 2011.

[44] A.D. Yaghjian. Electric Dyadic Green's functions in the source region. *Proceedings of the IEEE*, pages 248–263, 1980.

[45] D. Yu. The numerical computation of hypersingular integrals and its application in BEM. *Adv. in Eng. Softw.*, pages 103–109, 1993.

[46] T. Yu and W. Cai. High order window functions and fast algorithms for calculating dyadic electromagnetic Green's function in multilayered media. *Radio Sci.*, pages 559–569, 2001.

[47] B. Zinser and W. Cai. A well-conditioned hypersingular boundary element method for electrostatic potentials in the presence of inhomogeneities within layered media. *CiCP*, To appear, 2016.

[48] B. Zinser, W. Cai, and D. Chen. Quadrature Weights on Tensor-Product Nodes for Accurate Integration of Hypersingular Functions over Some Simple 3-D Geometric Shapes. *CiCP*, To appear, 2016.

APPENDIX A: ANALYTICAL FORM FOR THE GREEN'S FUNCTION

Recall from (12) the definition of G in terms of $G_{\mathrm{mod},j}$ and P_j. The coefficients of $G_{\mathrm{mod},j}$ must be chosen to satisfy the boundary conditions in (4). The resulting function G is as follows.

First, for a shorthand, let us define

$$g = (\varepsilon_1\tilde{\eta}_1 - \varepsilon_2\tilde{\eta}_2)(\varepsilon_2\tilde{\eta}_2 - \varepsilon_3\tilde{\eta}_3)e^{-2\tilde{\eta}_2 D} + (\varepsilon_1\tilde{\eta}_1 + \varepsilon_2\tilde{\eta}_2)(\varepsilon_2\tilde{\eta}_2 + \varepsilon_3\tilde{\eta}_3).$$

For $\mathbf{r}' \in \Omega_1$, we have

$$G(\mathbf{r},\mathbf{r}') = \begin{cases} P_1(\mathbf{r},\mathbf{r}') + \frac{1}{2\pi}\int_{-\infty}^{+\infty}\int_{-\infty}^{+\infty} dk_x dk_y e^{ik_x(x-x')}e^{ik_y(y-y')}A_1(k_\rho,z,z'), & \in \Omega_1, \\ \frac{1}{2\pi}\int_{-\infty}^{+\infty}\int_{-\infty}^{+\infty} dk_x dk_y e^{ik_x(x-x')}e^{ik_y(y-y')}\left[B_1(k_\rho,z,z') + C_1(k_\rho,z,z')\right], & \mathbf{r} \in \Omega_2, \\ \frac{1}{2\pi}\int_{-\infty}^{+\infty}\int_{-\infty}^{+\infty} dk_x dk_y e^{ik_x(x-x')}e^{ik_y(y-y')}D_1(k_\rho,z,z'), & \mathbf{r} \in \Omega_3, \end{cases} \tag{231}$$

whered

$$\begin{aligned} A_1(k_\rho,z,z') =& e^{-\tilde{\eta}_1 z}\frac{e^{\tilde{\eta}_1(2D-z')}}{4\varepsilon_1\tilde{\eta}_1\pi g}\left[(\varepsilon_1\tilde{\eta}_1 + \varepsilon_2\tilde{\eta}_2)(\varepsilon_2\tilde{\eta}_2 - \varepsilon_3\tilde{\eta}_3)e^{-2\tilde{\eta}_2 D}\right. \\ & \left. +(\varepsilon_1\tilde{\eta}_1 - \varepsilon_2\tilde{\eta}_2)(\varepsilon_2\tilde{\eta}_2 + \varepsilon_3\tilde{\eta}_3)\right], \\ B_1(k_\rho,z,z') =& e^{-\tilde{\eta}_2 z}\,\frac{e^{\tilde{\eta}_1(D-z')-\tilde{\eta}_2 D}}{2\pi g}(\varepsilon_2\tilde{\eta}_2 - \varepsilon_3\tilde{\eta}_3), \\ C_1(k_\rho,z,z') =& e^{\tilde{\eta}_2 z}\,\frac{e^{\tilde{\eta}_1(D-z')-\tilde{\eta}_2 D}}{2\pi g}(\varepsilon_2\tilde{\eta}_2 + \varepsilon_3\tilde{\eta}_3), \\ D_1(k_\rho,z,z') =& e^{\tilde{\eta}_3 z}\,\frac{e^{\tilde{\eta}_1(D-z')-\tilde{\eta}_2 D}}{\pi g}\varepsilon_2\tilde{\eta}_2. \end{aligned}$$

For $\mathbf{r}' \in \Omega_2$, we have

$$G(\mathbf{r},\mathbf{r}') = \begin{cases} \frac{1}{2\pi}\int_{-\infty}^{+\infty}\int_{-\infty}^{+\infty} dk_x dk_y e^{ik_x(x-x')}e^{ik_y(y-y')}A_2(k_\rho,z,z'), & \mathbf{r}\in\Omega_1, \\ P_2(\mathbf{r},\mathbf{r}') + \frac{1}{2\pi}\int_{-\infty}^{+\infty}\int_{-\infty}^{+\infty} dk_x dk_y e^{ik_x(x-x')}e^{ik_y(y-y')} & \\ \qquad\qquad \cdot\left[B_2(k_\rho,z,z') + C_2(k_\rho,z,z')\right], & \mathbf{r}\in\Omega_2, \\ \frac{1}{2\pi}\int_{-\infty}^{+\infty}\int_{-\infty}^{+\infty} dk_x dk_y e^{ik_x(x-x')}e^{ik_y(y-y')}D_2(k_\rho,z,z'), & \mathbf{r}\in\Omega_3, \end{cases} \tag{232}$$

where

$$\begin{aligned} A_2(k_\rho,z,z') &= e^{-\tilde{\eta}_1 z}\,\frac{e^{(\tilde{\eta}_1-\tilde{\eta}_2)D}}{2\pi g}\left[(\varepsilon_2\tilde{\eta}_2-\varepsilon_3\tilde{\eta}_3)e^{-\tilde{\eta}_2 z'} + (\varepsilon_2\tilde{\eta}_2+\varepsilon_3\tilde{\eta}_3)e^{\tilde{\eta}_2 z'}\right], \\ B_2(k_\rho,z,z') &= e^{-\tilde{\eta}_2 z}\,\frac{e^{-\tilde{\eta}_2 z'}}{4\varepsilon_2\tilde{\eta}_2\pi g}(\varepsilon_2\tilde{\eta}_2-\varepsilon_3\tilde{\eta}_3)[(\varepsilon_1\tilde{\eta}_1+\varepsilon_2\tilde{\eta}_2) - (\varepsilon_1\tilde{\eta}_1-\varepsilon_2\tilde{\eta}_2)e^{2\tilde{\eta}_2(z'-D)}], \\ C_2(k_\rho,z,z') &= e^{\tilde{\eta}_2 z}\,\frac{e^{-2\tilde{\eta}_2 D}}{4\varepsilon_2\tilde{\eta}_2\pi g}(\varepsilon_1\tilde{\eta}_1-\varepsilon_2\tilde{\eta}_2)[(\varepsilon_2\tilde{\eta}_2-\varepsilon_3\tilde{\eta}_3)e^{-\tilde{\eta}_2 z'} + (\varepsilon_2\tilde{\eta}_2+\varepsilon_3\tilde{\eta}_3)e^{\tilde{\eta}_2 z'}], \\ D_2(k_\rho,z,z') &= e^{\tilde{\eta}_3 z}\frac{e^{-\tilde{\eta}_2 z'}}{2\pi g}[(\varepsilon_1\tilde{\eta}_1+\varepsilon_2\tilde{\eta}_2) - (\varepsilon_1\tilde{\eta}_1-\varepsilon_2\tilde{\eta}_2)e^{2\tilde{\eta}_2(z'-D)}]. \end{aligned}$$

For $\mathbf{r}' \in \Omega_3$, we have

$$G(\mathbf{r},\mathbf{r}') = \begin{cases} \frac{1}{2\pi}\int_{-\infty}^{+\infty}\int_{-\infty}^{+\infty} dk_x dk_y e^{ik_x(x-x')}e^{ik_y(y-y')}A_3(k_\rho,z,z'), & \mathbf{r}\in\Omega_1, \\ \frac{1}{2\pi}\int_{-\infty}^{+\infty}\int_{-\infty}^{+\infty} dk_x dk_y e^{ik_x(x-x')}e^{ik_y(y-y')}\left[B_3(k_\rho,z,z') + C_3(k_\rho,z,z')\right], & \mathbf{r}\in\Omega_2, \\ P_3(\mathbf{r},\mathbf{r}') + \frac{1}{2\pi}\int_{-\infty}^{+\infty}\int_{-\infty}^{+\infty} dk_x dk_y e^{ik_x(x-x')}e^{ik_y(y-y')}D_3(k_\rho,z,z'), & \mathbf{r}\in\Omega_3, \end{cases} \tag{233}$$

where

$$\begin{aligned} A_3(k_\rho,z,z') =& e^{-\tilde{\eta}_1 z}\,\frac{e^{\tilde{\eta}_1 D-\tilde{\eta}_2 D+\tilde{\eta}_3 z'}}{\pi g}\varepsilon_2\tilde{\eta}_2, \\ B_3(k_\rho,z,z') =& e^{-\tilde{\eta}_2 z}\,\frac{e^{\tilde{\eta}_3 z'}}{2\pi g}(\varepsilon_1\tilde{\eta}_1+\varepsilon_2\tilde{\eta}_2), \\ C_3(k_\rho,z,z') =& -e^{\tilde{\eta}_2 z}\,\frac{e^{\tilde{\eta}_3 z'-2\tilde{\eta}_2 D}}{2\pi g}(\varepsilon_1\tilde{\eta}_1-\varepsilon_2\tilde{\eta}_2), \\ D_3(k_\rho,z,z') =& e^{\tilde{\eta}_3 z}\,\frac{-e^{\tilde{\eta}_3 z'}}{4\varepsilon_3\tilde{\eta}_3\pi g}\Big[(\varepsilon_1\tilde{\eta}_1+\varepsilon_2\tilde{\eta}_2)(\varepsilon_2\tilde{\eta}_2-\varepsilon_3\tilde{\eta}_3) \\ & + (\varepsilon_1\tilde{\eta}_1-\varepsilon_2\tilde{\eta}_2)(\varepsilon_2\tilde{\eta}_2+\varepsilon_3\tilde{\eta}_3)e^{-2\tilde{\eta}_2 D}\Big]. \end{aligned}$$

APPENDIX B: INTEGRAL EQUATIONS FOR THE PB EQUATION

Here we derive (38) and (43) from (37) and (42), respectively. The derivation matches the one described in [23] and is included here for completeness.

For the outside integral equation, we begin by putting (37), given here, in a suitable form.

$$\int_{\mathbb{R}^3\setminus(\Omega\cup B(\mathbf{r}',\rho)} \varepsilon_{\text{out}}(\mathbf{r})\nabla\left[G_{\text{out}}(\mathbf{r},\mathbf{r}')\nabla\phi_{out}(\mathbf{r}) - \phi_{out}(\mathbf{r})\nabla G_{\text{out}}(\mathbf{r},\mathbf{r}')\right] d\mathbf{r} = 0 \tag{234}$$

Now, we can apply Green's second identity. The boundary of $\mathbb{R}^3\setminus(\Omega \cup B(\mathbf{r}',\rho))$ is split into five parts, i.e.

$$0 = I + II + III + IV + V,$$

Part I: The integral on the infinite interface. As both $\bar{G}(\mathbf{r},\mathbf{r}')$ and $\phi(\mathbf{r})$ vanish at infinity, $I = 0$.

Part II: The integral on the interface of the layered structure. By the boundary conditions (4), the terms in the integral cancel and $II = 0$.

Part III: The integral on the side surface of the cylinder

$$III = -\int_{\partial\Omega} \varepsilon_{out}(\mathbf{r})\left[G_{out}(\mathbf{r},\mathbf{r}')\frac{\partial\phi_{out}}{\partial\mathbf{n}}(\mathbf{r}) - \phi_{out}(\mathbf{r})\frac{\partial G_{out}}{\partial\mathbf{n}}(\mathbf{r},\mathbf{r}')\right] dS(\mathbf{r}).$$

Part IV: The integral on the surface of the semi-sphere where P^+ is the upper semi-sphere and P^- is the lower one.

$$IV = -\int_{P^+\cup P^-} \varepsilon_{out}(\mathbf{r})\left[G_{out}(\mathbf{r},\mathbf{r}')\frac{\partial\phi_{out}}{\partial\mathbf{n}}(\mathbf{r}) - \phi_{out}(\mathbf{r})\frac{\partial G_{out}}{\partial\mathbf{n}}(\mathbf{r},\mathbf{r}')\right] dS(\mathbf{r}).$$

Part V: The integral on $\partial B(\mathbf{r}', \rho)$

$$V = \int_{\partial B(\mathbf{r}',\rho)} \varepsilon_{out}(\mathbf{r}) \left[G_{out}(\mathbf{r}, \mathbf{r}') \frac{\partial \phi_{out}}{\partial \mathbf{n}}(\mathbf{r}) - \phi_{out}(\mathbf{r}) \frac{\partial G_{out}}{\partial \mathbf{n}}(\mathbf{r}, \mathbf{r}') \right] dS(\mathbf{r})$$
$$= -\phi_{out}(\mathbf{r}') \text{ as } \rho \to 0. \tag{235}$$

Combining $I - V$ yields (38) where $S = \partial\Omega \cup P^+ \cup P^-$.

$$\phi_{\text{out}}(\mathbf{r}') = \int_S \varepsilon_{\text{out}}(\mathbf{r}) \left[\phi_{\text{out}}(\mathbf{r}) \frac{\partial G_{\text{out}}(\mathbf{r}, \mathbf{r}')}{\partial \mathbf{n}} - G_{\text{out}}(\mathbf{r}, \mathbf{r}') \frac{\partial \phi_{\text{out}}(\mathbf{r})}{\partial \mathbf{n}} \right] dS(\mathbf{r}) \tag{236}$$

For the inside integral equation, we begin with putting (42) in a suitable form.

$$\begin{aligned} \int_{\Omega \cup B(\mathbf{r}',\rho)} \varepsilon_{\text{ins}}(\mathbf{r}) \nabla \left[G_{\text{ins}}(\mathbf{r}, \mathbf{r}') \nabla \phi_{ins}(\mathbf{r}) - \phi_{ins}(\mathbf{r}) \nabla G_{\text{ins}}(\mathbf{r}, \mathbf{r}') \right] d\mathbf{r} \\ = -4\pi \sum_{i=1}^{N} q_i G_{\text{ins}}(\mathbf{r}_i, \mathbf{p}) \end{aligned} \tag{237}$$

As before, we can apply Green's second identity. The boundary of $\Omega \cup B(\mathbf{r}', \rho)$ is split into four parts, i.e.

$$-4\pi \sum_{i=1}^{N} q_i G_{\text{ins}}(\mathbf{r}_i, \mathbf{p}) = I + II + III + IV,$$

Part I: The integral on the interface of the layered structure. By the boundary conditions (4), the terms in the integral cancel and $I = 0$.

Part II: The integral on the side surface of the cylinder

$$II = \int_{\partial\Omega} \varepsilon_{ins}(\mathbf{r}) \left[G_{ins}(\mathbf{r}, \mathbf{r}') \frac{\partial \phi_{ins}}{\partial \mathbf{n}}(\mathbf{r}) - \phi_{ins}(\mathbf{r}) \frac{\partial G_{ins}}{\partial \mathbf{n}}(\mathbf{r}, \mathbf{r}') \right] dS(\mathbf{r}).$$

Part III: The integral on the part of surface of the half sphere

$$III = \int_{P^+ \cup P^-} \varepsilon_{ins}(\mathbf{r}) \left[G_{ins}(\mathbf{r}, \mathbf{r}') \frac{\partial \phi_{ins}}{\partial \mathbf{n}}(\mathbf{r}) - \phi_{ins}(\mathbf{r}) \frac{\partial G_{ins}}{\partial \mathbf{n}}(\mathbf{r}, \mathbf{r}') \right] dS(\mathbf{r}).$$

Part IV: The integral on $\partial B(\mathbf{r}', \rho)$

$$\begin{aligned} IV &= \int_{\partial B(\mathbf{r}',\rho)} \varepsilon_{ins}(\mathbf{r}) \left[G_{ins}(\mathbf{r},\mathbf{r}') \frac{\partial \phi_{ins}}{\partial \mathbf{n}}(\mathbf{r}) - \phi_{ins}(\mathbf{r}) \frac{\partial G_{ins}}{\partial \mathbf{n}}(\mathbf{r},\mathbf{r}') \right] dS(\mathbf{r}) \\ &= -\phi_{ins}(\mathbf{r}') \text{ as } \rho \to 0. \end{aligned} \tag{238}$$

Combining $I - IV$ yields (43) where $S = \partial\Omega \cup P^+ \cup P^-$.

$$\begin{aligned} \phi_{\text{ins}}(\mathbf{r}') = &\int_S \varepsilon_{\text{ins}}(\mathbf{r}) \left[G_{\text{ins}}(\mathbf{r},\mathbf{r}') \frac{\partial \phi_{\text{ins}}(\mathbf{r})}{\partial \mathbf{n}} - \phi_{\text{ins}}(\mathbf{r}) \frac{\partial G_{\text{ins}}(\mathbf{r},\mathbf{r}')}{\partial \mathbf{n}} \right] dS(\mathbf{r}) \\ &+ 4\pi \sum_{i=1}^{N} q_i G_{\text{ins}}(\mathbf{r}_i, \mathbf{r}') \end{aligned} \tag{239}$$

APPENDIX C: CURVILINEAR ELEMENTAL MAPPING

All the integrals are performed on the reference triangle with vertices at $(0,0)$, $(0,1)$, and $(1,0)$. Thus, it is necessary to have a mapping Γ that goes from the reference triangle to each element on the mesh that covers the boundary. There are 5 different types of elements on the mesh. The mapping matches the one described in [23] and is included here for completeness. They are as follows.

Case 1: The curved triangle $\triangle_t$ is located in the innermost layer of the semi-sphere's surface such that it has one node at the north or south pole. Let R be the radius of the semi-sphere and X_{center}, Y_{center}, and Z_{center} are the coordinates of the center of the sphere. Using spherical coordinates $(\check{r}, \check{\theta}, \check{\phi})$, the mapping is given by

$$\Gamma: \quad \mathbf{r}(\xi,\eta) = (R\sin\check{\theta}\cos\check{\phi} + X_{center}, R\sin\check{\theta}\sin\check{\phi} + Y_{center}, R\cos\check{\theta} + Z_{center}), \tag{240}$$

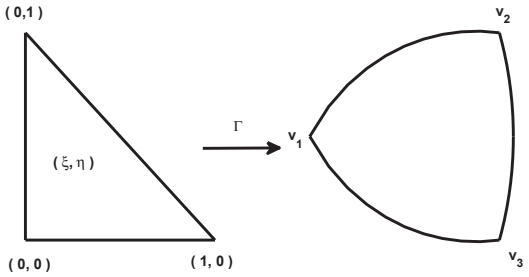

where

$$\check{\theta} = (1-\xi-\eta)\check{\theta}_{v_1} + (\xi+\eta)\check{\theta}_{v_2}, \qquad \check{\psi} = \begin{cases} 0, & \xi = \eta = 0, \\ \frac{\eta\check{\phi}_{v_2} + \xi\check{\phi}_{v_3}}{\xi+\eta}, & \text{otherwise.} \end{cases} \tag{241}$$

The corresponding Jacobian is

$$\left\| \frac{\partial}{\partial \xi} \times \frac{\partial}{\partial \eta} \right\| = \left| R^2 \sin(\check{\theta}) \, \frac{(\check{\phi}_{v_2} - \check{\phi}_{v_3})(\check{\theta}_{v_2} - \check{\theta}_{v_1})}{\xi+\eta} \right|. \tag{242}$$

Case 2: the curved triangle $\triangle_t$ is located on the semi-sphere surface, but does not have a node at the north or south pole. Again, let R be the radius of the semi-sphere and X_{center}, Y_{center}, and Z_{center} are the coordinates of the center of the sphere and use spherical coordinates $(\check{r}, \check{\theta}, \check{\phi})$. The mapping is given by

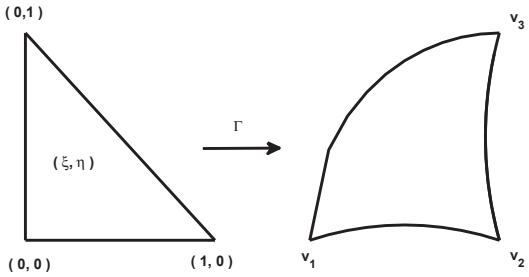

$$\Gamma: \quad \mathbf{r}(\xi,\eta) = (R\sin\check{\theta}\cos\check{\phi} + X_{center}, R\sin\check{\theta}\sin\check{\phi} + Y_{center}, R\cos\check{\theta} + Z_{center}), \tag{243}$$

where

$$\check{\theta} = (1-\xi)\check{\theta}_{v_2} + \xi\check{\theta}_{v_3}, \qquad \check{\phi} = (1-\xi-\eta)\check{\phi}_{v_1} + (\xi+\eta)\check{\phi}_{v_3}. \tag{244}$$

The corresponding Jacobian is

$$\left|\left|\frac{\partial}{\partial\xi} \times \frac{\partial}{\partial\eta}\right|\right| = \left|R^2 \sin(\check{\theta})\ (\check{\phi}_{v_1} - \check{\phi}_{v_3})(\check{\theta}_{v_3} - \check{\theta}_{v_2})\right|. \tag{245}$$

Case 3: The curved triangle $\triangle_t$ is located on the cylindrical surface. Using cylindrical coordinate by $(\tilde{\rho}, \tilde{\theta}, \tilde{z})$, we have

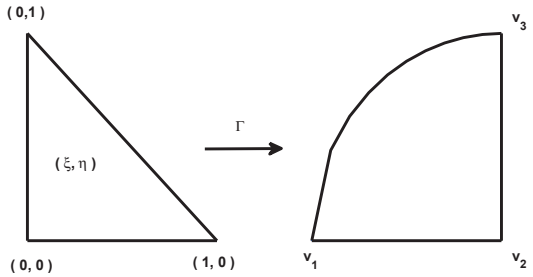

$$\Gamma: \quad \mathbf{r}(\xi,\eta) = (R\cos(\tilde{\theta}), R\sin(\tilde{\theta}), \tilde{z}), \tag{246}$$

where

$$\tilde{\theta} = (1-\xi-\eta)\tilde{\theta}_{v_1} + (\xi+\eta)\tilde{\theta}_{v_2}, \qquad \tilde{z} = (1-\xi)\tilde{z}_{v_1} + \xi\tilde{z}_{v_3}. \tag{247}$$

The corresponding Jacobian is

$$\left|\left|\frac{\partial}{\partial\xi} \times \frac{\partial}{\partial\eta}\right|\right| = \left|R\ (\tilde{z}_{v_3} - \tilde{z}_{v_1})(\tilde{\theta}_{v_2} - \tilde{\theta}_{v_1})\right|. \tag{248}$$

APPENDIX D: ROTATION MATRICES

The cube, cylinder, and sphere have rotational symmetry. We can take advantage of this by only calculating the weights $w_{j,k}$ from (91) for when the singularity is located at

certain interpolation points. When the singularity is located at an interpolation point for which there is no table, we provide a rotation map R that rotates the domain so that the singularity coincides with an interpolation point that has a table of weights. Let the rotation matrix R be defined by $R = R_x(\alpha)R_y(\beta)R_z(\gamma)$ so the space is first rotated around the z-axis; second, it is rotated around the y-axis; last, it is rotated around the x-axis. The multipliers $R_x(\alpha)$, $R_y(\beta)$, and $R_z(\gamma)$ are respectively given by:

$$\begin{bmatrix} 1 & 0 & 0 \\ 0 & \cos(\alpha) & -\sin(\alpha) \\ 0 & \sin(\alpha) & \cos(\alpha) \end{bmatrix}, \begin{bmatrix} \cos(\beta) & 0 & \sin(\beta) \\ 0 & 1 & 0 \\ -\sin(\beta) & 0 & \cos(\beta) \end{bmatrix}, \begin{bmatrix} \cos(\gamma) & -\sin(\gamma) & 0 \\ \sin(\gamma) & \cos(\gamma) & 0 \\ 0 & 0 & 1 \end{bmatrix}. \quad (249)$$

Note that 3×3 rotation matrices do not form a commutative group, i.e., $R_x(\alpha)R_y(\beta)R_z(\gamma) \neq R_z(\gamma)R_y(\beta)R_x(\alpha)$ in general. For each location of the singularity, corresponding rotation matrices are given in the appendices.

For example, the quadrature formula recorded in the tables for a singularity at node $\mathbf{r}'_i$ is

$$\int_{\Omega \setminus V_\delta(\mathbf{r}'_i)} \frac{f(\mathbf{r})}{|\mathbf{r} - \mathbf{r}'_i|^k} d\mathbf{r} \approx \sum_{j=1}^{M} f(\mathbf{r}_j) w_{j,k}, \quad (250)$$

and a symmetric node $\mathbf{r}''_i$ is related by a rotation matrix $R = R_x(\alpha)R_y(\beta)R_z(\gamma)$ according to

$$\mathbf{r}''_i = R\mathbf{r}'_i. \quad (251)$$

Then, the integral with a singularity located at $\mathbf{r}''_i$ can be done with the same quadra-

ture nodes and weights as in (250) with the help of the rotation matrix R:

$$\int_{\Omega\setminus V_\delta(\mathbf{r}_i'')} \frac{f(\mathbf{r})}{|\mathbf{r}-\mathbf{r}_i''|^k} d\mathbf{r} \approx \sum_{j=1}^{M} f(R\mathbf{r}_j) w_{j,k}. \tag{252}$$